PhD Dissertation

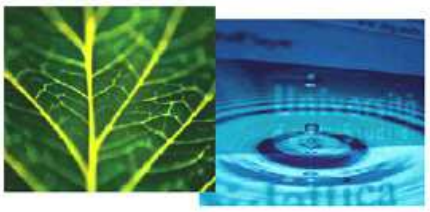

International Doctorate School in Information and Communication Technologies

DISI - University of Trento

Advanced Signal Processing Methods for Planetary Radar Sounders Data

Leonardo Carrer

Advisor:

Prof. Lorenzo Bruzzone

University of Trento

January 2018

A mia madre

Ma Nino non aver paura a sbagliare un calcio di rigore,
non è mica da questi particolari che si giudica un giocatore,
un giocatore lo vedi dal coraggio,
dall'altruismo e dalla fantasia.
Francesco De Gregori, La leva calcistica del '68

Abstract

Radar sounders are spaceborne electromagnetic sensors specifically designed for subsurface investigations. They operate in the HF/VHF part of the electromagnetic spectrum and are widely employed for applications such as monitoring changes to the polar ice sheets of the Earth and for the study of planetary bodies (e.g. Mars) from satellite.
Radar sounding of planetary bodies is a relatively young discipline both in terms of system design and data processing architectures. As a result of the current state of the art in system design, the data recorded by radar sounders are typically affected by artifacts, such as off-nadir surface clutter, which hinders its interpretation by scientists. On top of that, the analysis of the very large of amount of data produced by such systems is typically performed manually by experts thus inherently subjective and time-consuming. Therefore the development of automatic high-level processing strategies for reliable, objective and fast extraction of information is needed. Accordingly, this thesis work deals with different aspects of radar sounding namely system design, low-level and high-level processing.
The thesis provides three main novel contributions to the state of the art. First, we present a study on system design, performance assessment and 3D electromagnetic simulations of a radar sounding system specifically tailored for detecting lava tubes under the Moon surface. Lava tubes are considered to be important and useful structures. By having a stable temperature and by providing protection against cosmic ray radiation and micrometeorites impacts, they could potentially serve as natural shelter for human outposts on the Moon. The results presented in this thesis show that a multi-frequency radar sounder is the best option for effectively sound most of the lava tube dimension expected from the literature and that they show unique electromagnetic signature which can be used for their detection.
The second novel contribution is focused on low-level processing and consists in a bio-inspired clutter detection model based on bats echolocation. Very relevant analogies occur between a bat and radar sounder such as the nadir acquisition geometry. The mathematical model proposed in this thesis adapts the bats frequency diversity strategy (i.e. multi-frequency approach) to solve clutter ambiguities to the radar sounding case. The proposed bio-inspired clutter detection model has been tested and validated on experimental data acquired over Mars. The experimental results showed that the method is able to discriminate in a precise way the radar echoes arising from subsurface targets with respect to off-nadir surface clutter ones.
The third novel contribution of this thesis goes in the direction of high-level processing and in particular of automatic data analysis for accurate and fast extraction of relevant information from radar sounding data. To this extent, we propose a novel automatic method for retrieving the spatial position and radiometric properties of the subsurface layers based on Hidden Markov Models for radar response modeling and the Viterbi Algorithm for the inference step. Furthermore, a novel radargram enhancement and denoising technique has been developed to support the detection step. The effectiveness of the technique has been demonstrated on different radargrams acquired over the North Pole of Mars pointing out its superiority with respect to current state of the art techniques.

Keywords: Radar sounder, Ground Penetrating Radar, Synthetic Aperture Radar, Signal Processing, Remote Sensing, Planetary Exploration, Bats, Lava Tube.

Acknowledgements

This thesis work has been partially supported by the Italian Space Agency under Contract ASI/INAF n. 2013-056-R.O. "Partecipazione italiana alla fase A/B1 della missione JUICE" and by Thales Alenia Space Italia which partially funded the PhD scholarship.

The work compiled in this thesis is the result of an endeavor of perseverance and faith. Now that I climbed this mountain and I am standing on top of it, I can take a breath, turn around and look at what this journey had been and just say thanks to all the people that made this possible.

Foremost, I would like to thank Lorenzo for trusting and advising me and nonetheless faithfully supporting my exotic research ideas. I learned a lot from you.
I would like to thank all the people in Thales Alenia Space in Rome for supporting this thesis work and make it possible despite the difficulties. Renato, you thought me pretty much everything I know about the art of radar sounding. Now lets go to the other side of the ocean. Thanks Dusty for hosting me in your research group at Stanford and for making me discover the HomeState Texas tacos in LA. Also I would like to thank all the folks from the Radioglaciology group that made my California stay very pleasant. A special mention goes to the two gentlemen from Verona.
It is now time to acknowledge the University of Trento and RSLab folks. In particular, I would like to thank Massimo, Francesca, Davide and Ana with whom I shared the torment and delight of working on RIME. A very special thanks goes to Andrea for teaching me the art of slow eating and to Claudia for talk some sense into me whenever I got off on a tangent. Whenever I grew tired, you both reminded me I got one thing to do and to not ramble on.
I would like to thank my everlasting friends in Rome which I consider my extended family. Pally, Claudio, Lofi, Luca, Mucca, Pollo, Silvia, Marghe, Charlie, Vale and Spezza you are supporting, advising and encouraging me since we were in high school. We may have grown up, put some weight on and got some white hairs appearing on our heads but nothing really changed our pristine friendship in a significant way in the last 15 years. So, thanks for that.
A special mention goes to my girlfriend. Thanks for your patience and for unconditionally supporting me throughout this journey that made me wander around the world.
As this little page is coming to an end, I would like to thank my family for the unconditional support they always gave me and for making me the person I am today.

Leonardo

Contents

List of Tables

List of Figures

List of Abbreviations

ALSE	Apollo Lunar Sounder Experiment
AQ	Amazonis Quadrangle
DEM	Digital Elevation Model
DM	Deuteronilus Mensae
ESA	European Space Agency
GPR	Ground Penetrating Radar
HF	High Frequency
HMM	Hidden Markov Model
LRS	Lunar Radar Sounder
MARSIS	Mars Advanced Radar for Subsurface and Ionosphere Sounding
MRO	Mars Reconnaisance Orbiter
PRF	Pulse Repetion Frequency
RDR	Reduced Data Records
RIME	Radar for Icy Moon Exploration
RMS	Root Mean Square
SHARAD	Shallow Radar
SNR	Signal-to-noise Ratio
SP	South Pole
VA	Viterbi Algorithm
VHF	Very High Frequency

List of Symbol

$\mathbf{E}$	Electric Field
$\mathbf{H}$	Magnetic Field
ω	Angular frequency
f	Electromagnetic wave frequency
ϵ_c	Complex Permittivity
ϵ_r	Relative permittivity
μ_r	Relative permeability
α	Medium attenuation constant
β	Medium phase constant
S	Electromagnetic Power Density
η	Characteristic impedance of the transmission medium
$\tan\delta$	Loss tangent
σ	Conductivity
c	Speed of light in a medium
Γ	Reflection coefficient
T	Transmission coefficient
θ_{inc}	Incidence angle
θ_t	Transmission angle
P_t	Transmit power
G	Antenna gain
h	Sensor height
σ^0	Radar backscatter coefficient
A_{ill}	Illuminated area
A_{eff}	Antenna effective area
λ	Wavelength
z	Penetration depth
R_r	Range Resolution
B	Radar Bandwidth
R_{at}	Along-track resolution
R_{act}	Across-track resolution
L_s	Synthetic aperture length
SNR	Signal to Noise Ratio
T_g	Galactic noise temperature
T_e	Electronics noise temperature

T	Overall noise temperature
k_b	Boltzmann constant
P_n	Noise Power
T_s	Pulse length
G_r	Range compression gain
G_{az}	Azimuth compression gain
PRF	Pulse repetition frequency
θ_c	Clutter angle
SCR	Signal to clutter ratio
A_c	Clutter equivalent area
P_n	Noise Power
σ_0^2	Radar backscattering coefficient of the surface
r_t	Regolith average thickness
h_r	Lava tube depth
w	Lava tube width
N_r	Number of rocks by unit area
K	Decay constant
ρ	Two-way rough surface transmission power loss
σ_b	RMS variation of surface height
ψ	RMS rough surface phase variation
θ	Off-nadir angle
f_0	Radar central frequency
H	Hurst coefficient
T	Topothesy
A_f	Area of the lava tube floor
s	Surface RMS slope
d	Radar slant range
ΔP_s	Surface power Ratio
ΔP_{ss}	Subsurface power ratio
$\hat{d}$	Distance versor
NPM	Noise Power Measurement
x	Cartesian coordinate (range direction)
y	Cartesian coordinate (azimuth direction)
$R(x, y)$	Original bidimensional radargram
R_{AV}	Averaged bidimensional radargram
R_p	Local maxima bidimensional radargram
N_{AV}	Scalar averaging length
ν	Sample amplitude
p_s	Signal amplitude conditional density function
p_n	Noise amplitude conditional density function
NR	Noise radargram region
SR	Signal radargram region
P_{FA}	Probability of false alarm
P_D	Probability of detection

T_h	Scalar threshold
f_r	Spatial sampling frequency
f_s	Sampling frequency
ΔR_r	Radar range accuracy
Υ	Half size of the rectangular function
ζ	Index of the radargram block being processed
L	Total number of time steps
Q	State sequence
Λ	State bound
$\mathbf{O}$	Observation vector
$\{\pi\}$	Initial state distribution
$\{a\}$	State transition probability matrix
$\{b_j(\mathbf{O}_t)\}$	Continuous emission probability densities
Ω	Seed Function
y_c	Current azimuth coordinate
χ	Initial range coordinate
δ	Probability of the partial best path
φ	Back-pointers matrix
μ	Multivariate gaussian mean vector
Σ	Multivariate Gaussian covariance matrix
σ_v	Scalar value of lateral continuity of the layer boundary
N_L	Number of layers in the radargram
o_h	Computational overhead of the method

Introduction

This chapter presents an introduction to the PhD thesis work. We briefly introduce the framework where this work has been developed by providing an overview of the problems affecting radar sounder systems. This allows us to highlight and discuss the motivation, the objectives and the novel contributions of this thesis. Finally, the structure of the document is reported.

Background

Radar remote sensing acquires information about a given target or phenomenon without making physical contact with the object. This technique is employed in numerous fields such as Earth Sciences, military, intelligence, commercial, economic, planning, and humanitarian applications. In this thesis, we focus on remote sensing radars for planetary exploration. These type of radars are mainly used for mapping and understanding the geophysical characteristics of celestial bodies other than Earth.
Planetary radars falls into two categories namely imaging radars and sounding radars. The planetary imaging radars category typically includes synthetic aperture and altimeter radar instruments, such as the ones flewn on-board the Magellan and Cassini spacecraft, which were able to penetrate the thick clouds of Venus and Titan respectively providing important information regarding their surface morphology. In contrast to imaging radars, sounding radars are unique instruments being able to acquire data about a given planet subsurface. Their low operating frequency allows them to penetrate hundreds of meters, or even kilometers, below the surface. In this thesis we focus our attention on the latter ones.
The first radar sounder flown was ALSE (Apollo Lunar Sounder Experiment) on board Apollo 17. Other sounder instruments flown are MARSIS (Mars Advanced Radar for Subsurface and Ionosphere Sounding) on board the European Space Agency's Mars Express probe and SHARAD (Mars SHAllow RADar sounder) on JPL's Mars Reconnaissance Orbiter (MRO). They are currently operational. A radar sounder was also deployed on the Japanese probe SELENE which investigated the Moon subsurface. Due to their low operating frequency (MHz range), this type of instruments have capability of penetration in icy, arid and rocky (i.e. basaltic) environment such as volcanic regions.
There are mounting evidence that ice can be found throughout the Solar System[1], from Mercury, to the far reaches of the Oort cloud and comets. Some solar system bodies surface regions are believed to be composed almost entirely of ice such as Saturn's moon Enceladus and Jupiter's moon Europa. Ice also occurs in the form of polar caps such

as the North and South Polar Layered Deposit of Mars, as revealed by MARSIS and SHARAD instruments, and may persist inside the coldest and darkest craters of different planetary bodies such as Ceres [2]. These observation greatly renewed the interest for radar sounders as subsurface exploration systems. In this context, the approved Jupiter Icy Moons Explorer (JUICE) mission of the European Space Agency (ESA) will carry onboard the Radar for Icy Moon Exploration (RIME). RIME is a radar sounder specifically designed for studying the subsurface of the icy moons Ganymede, Europa and Callisto. Another target of interested resulting from recent evidences are the lava tubes under the Moon surface. Gravitometric observations by the GRAIL spacecraft suggest the presence of lunar lava tubes with widths in the order of a kilometer. Such structures can remain stable with a ceiling that is about 2 meters thick. Lava tubes at least 500 m underground can theoretically remain stable with widths up to 5 km [3]. The potential for global lava tubes mapping gravimeters is very limited. In order to accurately detect lava tubes it is necessary to perform direct subsurface measurements of the shallow lunar subsurface which can be achieved by the means of a radar sounder.

It is therefore clear that radar sounders can play an important role in advancing our knowledge regarding the past and future of the Solar System. However, this type of instruments are affected by a number of unwanted nuisances which limits their data interpretation. These nuisance are mainly the result of the current state of the art in system design, low-level and high-level processing. In the context of low-level processing, one of the most important problem is clutter. In a single given acquisition, planetary sounders antennas (which are typically dipoles for mechanical reasons) are always pointed toward nadir direction with respect to the surface and illuminate large surface and subsurface regions. The very large antenna footprint implies that off-nadir surface reflections (i.e. surface clutter) of the transmitted signal can be disguised for echoes coming from the interior of the target area. This causes a serious issue in terms of data interpretation. With regard to high-level processing, a crucial issue is that the data analysis is still carried out by visual inspection by planetary geophysicists thus is inherently subjective. Accordingly, it is mandatory to develop advanced high-level processing techniques that can automatically analyze and extract information from the data for properly supporting the scientific community. Automatic data analysis assumes a particular importance also considering that the past radar sounding sounding missions to the Moon and Mars provided a huge amount of data and the same data volume is expected by future missions.

This thesis focuses on radar sounding system design and the subsequent low-level and high-level processing in order to overcome the aforementioned shortcomings. The first novel contribution is related to a new type of multi-frequency radar sounding systems envisioned for lava tube exploration on the Moon. The second novel contribution consists in a low-level processing method for clutter detection based on bats echolocation. It is interesting to notice that the proposed method for low-level processing is intertwined with novel concepts of radar sounder system design. For instance, a clutter detection method operating on frequency diversity (i.e. low-level processing) would required a multi-frequency radar sounder system. Finally, we propose a high-level processing technique for reliable and fast radar sounder data extraction.

The objectives and novel contributions of this thesis are further elaborated in the next

section of this chapter.

Objectives and Novel Contributions of the Thesis

The work presented in this thesis is aimed at investigating and defining novel strategies in system design, low-level and high-level processing for radar sounders. In greater detail, the novel contribution of the thesis are as follows:

1. *System design*: A study on a multi-frequency radar system specifically designed for detecting lava tubes under the Moon surface.

2. *Low-level processing*: A bio-inspired clutter detection model based on bats echolocation

3. *High-level processing*: A technique for the automatic enhancement and detection of layering in radar sounder data

In the following subsections the main objectives and novelties for each contribution of the thesis will be briefly described.

A Multi-Frequency Radar Sounder for Lava Tubes Detection on the Moon

As stated before, lunar lava tubes are subsurface structures which are potential candidates for future human outposts on the Moon. Recently, remote sensing observations of the Moon based on optical cameras and gravitational field mapping have detected features that can be directly related to the presence of lava tubes. However, the potential for global lava tubes mapping using these types of sensors is very limited. In order to accurately detect lava tubes it is necessary to perform direct subsurface measurements of the shallow lunar subsurface. Unfortunately, past Moon radar sounder missions were not focused on the detection of lava tubes and thus had limited capability to detect them. In this thesis, a novel study is carried out to determine the optimal type of orbiting radar instrument that would be needed to detect the majority of lunar lava tubes, based on their expected properties. To define this instrument, a performance assessment versus different parameters of the radar sounder and an electromagnetic signature analysis (based on 3D electromagnetic simulations) are developed to determine the possibility to detect lava tubes having different sizes from orbit. The results show that a multi-frequency radar sounder in the MHz range is the best option to accurately detect most of the lava tubes dimension which are expected from the structural stability analysis recently published in the literature. In particular, the main driving factors limiting the radar sounder penetration capabilities are the frequency-dependent attenuation of the Moon basalt substrate and its roughness. Moreover, the electromagnetic simulations show that phase inversion due to subsurface dielectric transitions is a very effective feature to differentiate lava tube echoes from off-nadir surface clutter.

A Bat Inspired Model for Clutter Reduction in Radar Sounder Systems

Due to the radar sounders wide antenna beam, off-nadir surface reflections (i.e. clutter) of the transmitted signal can compete with echoes coming from the subsurface thus masking them. Different strategies have been adopted for clutter mitigation. However, none of them proved to be the final solution for this specific problem. In this context, we took inspiration from bats to study effective cletter detection strategies. Bats are very well known for their ability in discriminating between a prey and unwanted clutter (e.g. foliage) by effectively employing their sonar. According to recent studies, big brown bats can discriminate clutter by transmitting two different carrier frequencies. Most interestingly, there are many striking analogies between the characteristics of the bat sonar and the one of a radar sounder. Among the most important ones, they share the same nadir acquisition geometry and transmitted signal type (i.e. linear frequency modulation). In this thesis, we explore the feasibility of exploiting frequency diversity for the purpose of clutter discrimination in radar sounding by mimicking unique bats signal processing strategies. Accordingly, we propose a frequency diversity clutter reduction method based on specific mathematical conditions that, if verified, allows to perform the disambiguation between the clutter and the subsurface signal. These analytic conditions depend on factors such as difference in central carrier frequencies, surface roughness and subsurface material properties. One of the main strength of the proposed technique is that it does not rely on any a-priori information such a digital elevation model of the surface that is not always available. The method performances have been evaluated on Mars experimental data acquired by SHARAD proving its effectiveness. In particular the results obtained on radargrams of icy and volcanic region of Mars, which where previously analyzed by time-consuming analysis conducted by planetary geophysicists, proved that the method can effectively discriminate between genuine subsurface reflections and off-nadir surface clutter thus paving the way for a new generation of multi-frequency radar sounders with clutter discrimination capabilities.

An Automatic Enhancement and Detection Technique of Layering in Radar Sounder Data

The analysis of the very large amount of data produced by radar sounders requires the development of automatic techniques for an objective, accurate and fast extraction of relevant information from radargrams. A typical example of application of automatic techniques is the extraction of relevant information regarding subsurface layering (i.e. stratification) in icy regions. From the geophysical point of view, the analysis of subsurface layering is particular important. Through layering analysis is it possible to obtain valuable information about past climate of a planetary body. Recent work on automatic techniques for layering extraction from radargrams showed promising results but the accuracy is still lower to the one of an expert human annotator.
In this thesis, we propose a novel technique for the automatic detection of layer boundaries based on a local scale Hidden Markov Model (HMM), which models the radar response in the presence of a layer boundary, and the Viterbi Algorithm, which performs the inference step. The proposed technique is based on a divide and conquer strategy that

executes the Viterbi algorithm using the observation data and the HMM to infer the most likely layer boundary location within a small radargram portion. Finally, a detection strategy is defined to chain together the inferred local layer locations. Furthermore, a novel radargram enhancement and denoising technique tailored to support the detection step is presented. The effectiveness of the proposed technique has been confirmed by testing it on different radargrams acquired by SHARAD (SHAllow RADar) over the North Pole of Mars. The results obtained point out the superiority of the proposed method in retrieving the position of each layer boundary (and thus of the related intensity and geometric properties) with respect to the state-of-the-art techniques.

Thesis Organization

The present Chapter provided a brief overview on planetary remote sensing with radar sounders. In addition, it introduced the motivation, the objectives and the novel contributions of this thesis. The rest of this dissertation is organized in five main chapters. Chapter 1 illustrates the fundamentals and the background notions useful for understanding the thesis. Chapter 2 presents the proposed approach for designing a multi-frequency radar sounder for lava tubes detection on the Moon. Chapter 3 describes the bat-inspired low-level processing model for clutter detection in radar sounder systems while Chapter 4 presents the novel high-level processing technique for automatic enhacement and detection of layering in radar sounder data. In each chapter an introduction to the specific topic and a review of the related state-of-the-art is provided. Finally, in the last chapter the conclusions of the thesis are drawn and proposals for future research developments are discussed.

Chapter 1

Fundamentals and Background

In this chapter we review the fundamentals of radar, planetary radar sounding and electromagnetic waves propagation in media. This provides the basic concepts and definition needed in the next chapters of the thesis.

1.1 Radar Basics and Historical Overview

The principle on which radar operates is similar to the familiar principle of sounds wave reflection like the echoes inside a cave. By knowing the speed of sound, it is possible to estimate the distance of the reflecting objects. Radar uses electromagnetic energy pulses in the same fashion. The radar transmits electromagnetic energy which is then reflected by the target. Only a small portion of the energy returns to the receiver. The return energy is called echo from the target. By knowing the velocity of the electromagnetic wave in a given medium is it possible to determine the target distance. A radar system consists of a transmitter producing electromagnetic waves in the radio or microwaves domain, a transmitting antenna, a receiving antenna (often the same antenna is used for transmitting and receiving), a receiver and a processing block to determine properties of the object(s).
Nowadays radar systems are used for a broad variety of very different applications spanning from air traffic monitoring to the study of planetary bodies (see Fig 1.1).
The main advantages of a radar sensor are the following:

- Day and night operation both in lightness or darkness over a long range.
- Capability of operations in all weather conditions, in fog and rain to even penetrate walls or layers of snow.
- Detection and tracking of moving objects.
- Unmanned operations.

The history of radar as an effective instrument for remote sensing and astronomy can be seen as the summation of many developments and scientific discovery. The following list summarizes the most important scientific milestones toward the development of modern planetary imaging and sounding radars [4]:

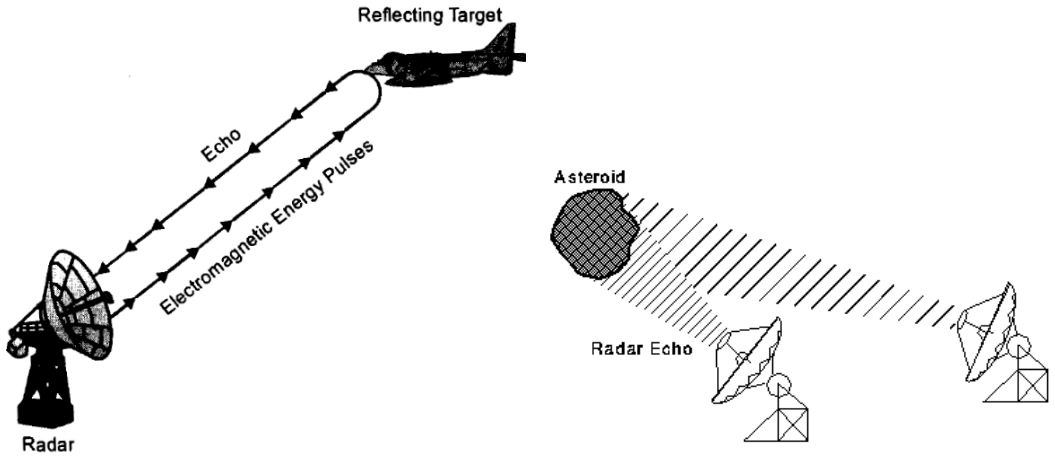

(a) (b)

Figure 1.1: Radar Systems are used in many different applications ranging from (a) air traffic control to (b) exploration of planetary bodies.

- **1865**: James Clerk Maxwell presents his "Theory of the Electromagnetic Field" (description of the electromagnetic waves and their propagation). Maxwell demonstrated that electric and magnetic fields travel through space in the form of waves, and at the constant speed of light.
- **1886**: Heinrich Rudolf Hertz discovered electromagnetic waves, thus demonstrating the Maxwell theory.In his 1887 experiment he found that electromagnetic waves propagates through different types of materials. He also found that the nature of electromagnetic waves is similar to visible light. They can be reflected, refracted, and polarized.
- **1897**: Guglielmo Marconi achieved the first long distance transmission of electromagnetic waves. Moreover, he noticed radio waves were being reflected back to the transmitter by objects in radio beacon experiments he conducted in 1899.
- **1900**: Nicola Tesla suggested that the reflection of electromagnetic waves could be used for detecting of moving metallic objects.
- **1904**: Christian Hülsmeyer invented the "telemobiloscope" for a traffic monitoring on the water in poor visibility. He gave a public demonstrations in Germany and the Netherlands of the use of radio echoes to detect ships so that collisions could be avoided. This was the first radar practical test.
- **1935**: Robert Watson-Watt discovered that radio waves can be used to detect aircraft at a distance. He proposed the first radar concept.
- **1946**: Radio astronomy and radar astronomy are introduced as disciplines.
- **1952**: Carl Wiley discovered the technique of Doppler Beam Sharpening as a mean of improving the spatial resolution of long wavelength imaging radar. This technique

is often referred as synthetic aperture radar. It allows a small antenna to achieve the same resolution of a much larger one by exploiting the Doppler shift induced on the radar echo by a moving platform.

- **1961**: Jet Propulsion Laboratory is able to record a radar echo from the Venus Surface. This marks the start of radar observation of planetary bodies in the Solar System.
- **1962**: Waite and Schmidt demonstrated that low-frequency radars were able to measure the thickness and other features of polar glaciers.
- **1972**: For the first time, low frequency electromagnetic waves are used to probe the interior of a planetary body. The Apollo Lunar Sounder Experiment used radar to study the Moon's interior revealing structures beneath the Moon's surface.
- **1973**: British scientists in Antarctica confirmed through airborne ground penetrating radar campaign the existence of a vast sub-glacial lake known as lake Vostok. This is the 16th largest lake in the world by surface area and it is covered by more than 3 kilometer-thick ice cap.
- **1978**: First spaceborne satellite imaging radar. Seasat satellite flew a microwave altimeter, a multi-beam scatterometer and a synthetic aperture radar. Its primary goal was to study the Earth's oceans.
- **1990**: The Magellan probe to Venus became the first interplanetary synthetic aperture radar. It provided high resolution detail of the Venus surface.
- **1993**: By measuring the displacement of the Earth's surface caused by an earthquake in California, Didier Massonnet proved the feasibility of interferometry with spacebourne radars.
- **1993-2017**: Cassini radar made important discoveries on Saturn's moon Titan. It proved the existence of oceans and lakes of liquid methane on Titan's surface.
- **2005-2018**: MARSIS became the first radar sounder to be deployed in orbit around Mars and has been collecting data ever since. It provided strong evidence for a former ocean on Mars. The radar is still operative.
- **2006-2018**: SHARAD radar sounder, which is currently orbiting and operating around Mars, provided strong and multiple evidence of water ice deposits both at polar and mid-latitudes regions of Mars.

By analyzing this radar historical overview in the perspective of this thesis dissertation on radar sounding, we can highlight the following. The work by Waite et al. [5] in 1962 on electromagnetic waves measurements of the electrical characteristics and thickness of ice at high and ultra-high frequencies in both polar areas, set the starting point for electromagnetic sounding of Earth's subsurface. Until 1972, electromagnetic probing of the subsurface was merely confined to terrestrial application mainly in icy regions. We denote this research field as terrestrial radar sounding. The successful results of the

Apollo Lunar Sounder Experiment [6] in 1972 paved the way for planetary exploration of subsurface bodies. This experiment marked the start of planetary radar sounding. In the next section of this chapter we analyze in more detail the background of radar sounding both in terms of underlying physical principles and acquisition process.

1.2 Radar Sounding

1.2.1 Overview

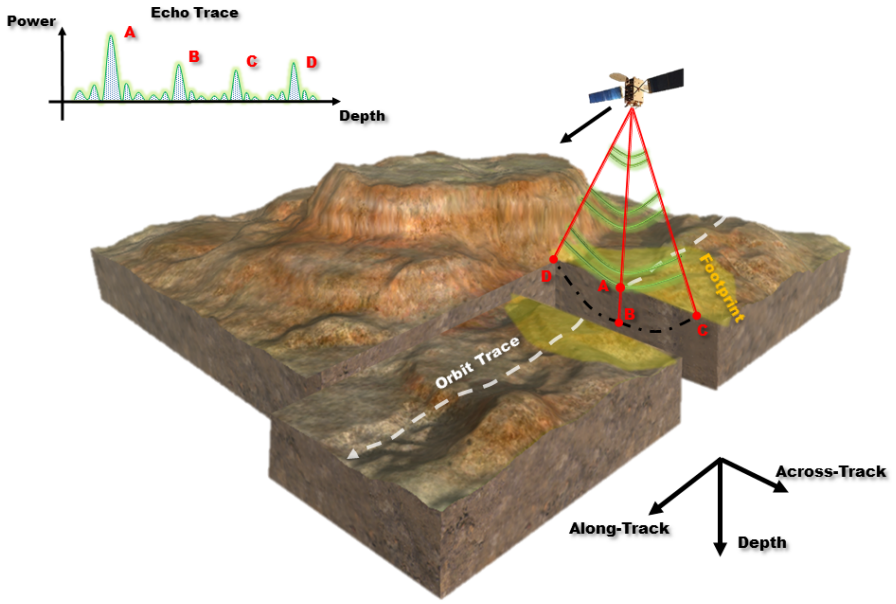

Figure 1.2: The radar sounding main goal is to acquire the signal coming from the nadir surface and subsurface regions (points A and B). Due to the large antenna footprint, the echo trace contains unwanted reflections coming from the antenna footprint sides (points C and D). A radar sensor measures time intervals occurring between the signal transmission and reception and not absolute distances. This implies that reflections from points C and D can be disguised as subsurface signal. In fact, in a radar system distance is inferred from time delay by knowing the wave speed in the medium.

Planetary sounders are spacebourne radars which are widely employed for geophysical exploration of celestial bodies around the solar system. In order to investigate the subsurface of a given target, a planetary radar sounder transmits pulsed electromagnetic radiation in the HF/VHF electromagnetic band (e.g. 1 MHz to 300 MHz) and, as it travels through the subsurface, each dielectric discontinuity in the ground material results in part of the signal being reflected towards it. These signal reflections (i.e. echoes) are subsequently recorded by the sensor thus forming an echo trace for each given acquisition

(Fig. 1.2). By analyzing these echo traces it is possible to obtain crucial information on the subsurface structure and composition. This is achieved by studying (i) the change of propagation velocity induced by the medium, (ii) the waves attenuation in the medium and (iii) the amount of reflected energy at the interface between two subsurface media. By stacking together subsequent echo traces a bidimensional image (denoted as radargram)(Fig. 1.3) is formed where one axis represents depth and the other one the position of the sensor along its ground track. Due to the wide antenna beam pattern of a planetary radar sounder, echoes coming from off-nadir reflections of the surface can compete with echoes coming from the subsurface thus masking them (Fig. 1.2 and 1.3).
Radar sounders have been successfully employed to probe the subsurface of Mars[7, 8] and the Moon [9, 6]. As an example, by using radar sounder data scientists were able to confirm the presence of nearly pure water ice within the South Polar Layer Deposits of Mars [10] and to observe its accumulation and erosion [11]. Moreover, the recent evidence supporting the thesis that there could be liquid water under the ice surface of celestial bodies such as the Galilean moons of Jupiter [12] greatly renewed the interest for such remote sensing systems. Similar sensors mounted on aircrafts are widely used for monitoring Earth's ice sheets. As an example, airbourne radar sounders data provided strong evidences of subsurface lakes in Antarctica that led to the discovery and further investigation of Lake Vostok [13, 14]. Even if the underlying physical principles for retreving the subsurface properties are similar, airbourne sounders differ from planetary ones due to the very different acquisition geometry and the mechanical constraints.
The rest of this section is organized as follows. In Subsection 1.2.2 we discuss the fundamental physical principle of electromagnetic wave propagation in media. Then in Subsection 1.2.3 the radar sounder acquisition process is discussed along with the radar equation for radar sounding where we apply the principles discussed in 1.2.2). The rest of the subsections discuss important quantities for radar sounding namely geometric resolution (1.2.4), signal to noise ratio (1.2.5) and clutter contribution (1.2.6).

1.2.2 Concepts of Eletromagnetic Waves Propagation relevant to Radar Sounding

Electromagnetic Plane Waves Propagation in Lossy Media

In this section we develop a basic physical understanding of plane wave propagation in lossy media. This is required in order to understand the underlying principles behind radar sounding and to define important quantities such as the attenuation constant which will be recalled throughout the thesis.
In the phasor domain we define a time-varying electric $\boldsymbol{E}(x, y, z; t)$ and magnetic field $\boldsymbol{H}(x, y, z; t)$, where t is the time variable and x, y, z the cartesian coordinates as following [15]:

$$\boldsymbol{E}(x, y, z; t) = \mathcal{R}[\widetilde{\boldsymbol{E}}(x, y, z)e^{j\omega t}] \tag{1.1}$$

where ω is the angular frequency $[rad/s]$ which can be expressed as $\omega = 2\pi f$ where f $[Hz]$ is the electromagnetic wave frequency. Similar definition applies to $\boldsymbol{H}$. In the phasor

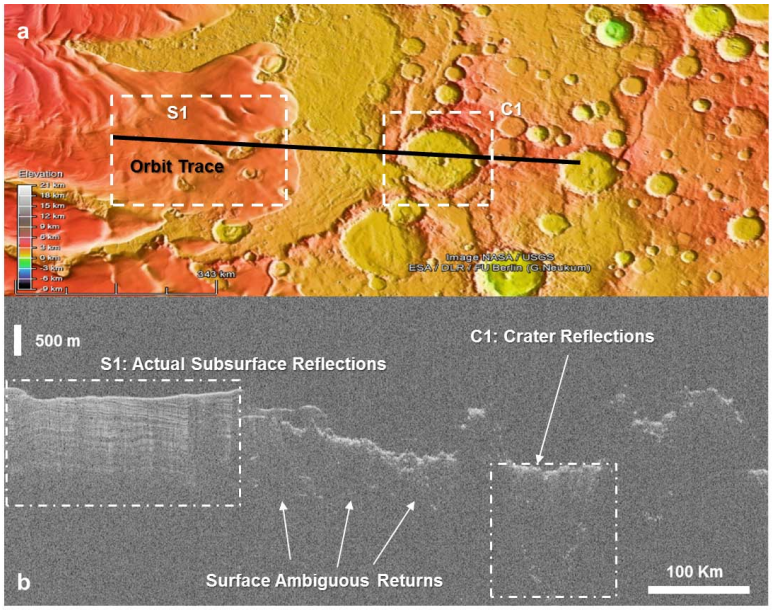

Figure 1.3: (**a**) Orbit trace of the SHallow RADar [7] acquisition 243101 projected over Mars South Pole region of Promethei Lingula. S1 represents a region where the instrument detects subsurface layered deposits while C1 is an example of ambiguous return due to off-nadir reflections from the crater rim (**b**) SHARAD radargram of acquisition 243101. From the image we can notice that there are many ambiguous returns which cause difficulties in the data interpretation.

domain, we can write Maxwell equations in the following way:

$$\nabla \cdot \widetilde{\boldsymbol{E}} = 0 \tag{1.2}$$

$$\nabla \times \widetilde{\boldsymbol{E}} = -j\omega\mu\widetilde{\boldsymbol{H}} \tag{1.3}$$

$$\nabla \cdot \widetilde{\boldsymbol{H}} = 0 \tag{1.4}$$

$$\nabla \times \widetilde{\boldsymbol{H}} = j\omega\epsilon_c\widetilde{\boldsymbol{E}} \tag{1.5}$$

where $\widetilde{\boldsymbol{E}}$ and $\widetilde{\boldsymbol{H}}$ are the vector phasors for the electric and magnetic field respectively, and μ is the magnetic permeability. We define ϵ_c as the complex permittivity equal to:

$$\epsilon_c = \epsilon - j\frac{\sigma}{\omega} = \epsilon^{'} - j\epsilon^{''} \tag{1.6}$$

We define the relative permittivity (i.e. dielectric constant) ϵ_r and permability μ_r as follows:

$$\epsilon_r = \epsilon/\epsilon_0 \tag{1.7}$$

$$\mu_r = \mu/\mu_0 \tag{1.8}$$

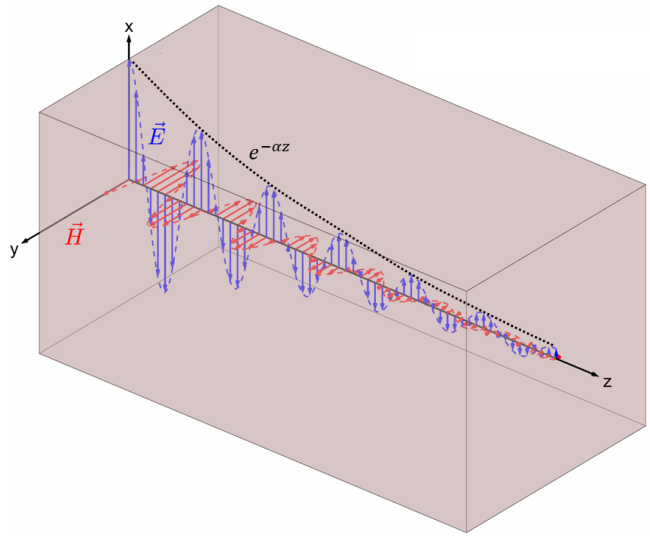

Figure 1.4: Electromagnetic waves propagation in a lossy media. In this example, the electric **E** and magnetic field **H** are attenuated as they propagate inside the dielectric box.

where ϵ_0 and μ_0 are the permittivity and permeability of vacuum respectively. The homogeneous wave equation for $\widetilde{\boldsymbol{E}}$ resulting from manipulating (1.3) and (1.5) is equal to:

$$\nabla^2 \widetilde{\boldsymbol{E}} + \omega^2 \mu \epsilon_c \widetilde{\boldsymbol{E}} = 0 \tag{1.9}$$

Without loosing in generality, we assume the electric field phasor to be equal to $\widetilde{\boldsymbol{E}} = \widetilde{E}_x(z)\hat{\boldsymbol{x}}$. This corresponds to a uniform plane wave traveling in the z direction. Accordingly, (1.9) reduces to:

$$\frac{d^2 \widetilde{E}_x(z)}{dz^2} + \omega^2 \mu \epsilon_c \widetilde{E}_x(z) = 0 \tag{1.10}$$

The solution to (1.10) is formed by two terms, one describing a wave traveling in the positive z direction and one in the negative z direction. We consider only the former one (see Fig. 1.4) therefore the solution is equal to:

$$\widetilde{\boldsymbol{E}}(z) = E_{x0} e^{-\sqrt{-\omega\mu\epsilon_c} z} \hat{\boldsymbol{x}} = E_{x0} e^{-\alpha z} e^{-j\beta z} \hat{\boldsymbol{x}} \tag{1.11}$$

where E_{x0} is the electric field amplitude.
We define α as the medium's attenuation constant and β as the phase constant defined as:

$$\alpha = \omega \left\{ \frac{\mu \epsilon'}{2} \sqrt{1 + (\frac{\epsilon''}{\epsilon'})^2} - 1 \right\}^{1/2} \tag{1.12}$$

$$\beta = \omega \left\{ \frac{\mu \epsilon'}{2} \sqrt{1 + (\frac{\epsilon''}{\epsilon'})^2} + 1 \right\}^{1/2} \tag{1.13}$$

In radar sounding, we are interested in the power of the electric field rather than in the amplitude. In this case, the time-average value of the Poynting vector which defines the power density S is equal to:

$$S = \frac{1}{2|\eta|}|\widetilde{\boldsymbol{E}}(z)|^2 = \frac{1}{2|\eta|}|E_{x0}|^2 e^{-2\alpha z} \tag{1.14}$$

where $\eta = \sqrt{\mu/\epsilon_c}$ is the characteristic impedance of the transmission medium. From (1.14) it is clear that the attenuation constant α plays an important role in determining the energy dissipation experienced by the electromagnetic wave as it travels through a given medium being the power density exponentially dependent on it. The penetration depth in a given medium is typically assumed to be equal to $1/2\alpha$. Losses in a medium are typicall expressed as $[dB/m]$. We define as the loss tangent $\tan\delta$ the following quantity:

$$\tan\delta = \frac{\epsilon''}{\epsilon'} = \frac{\sigma}{2\pi f \epsilon} \tag{1.15}$$

The loss tangent represents the material inherent dissipation of electromagnetic energy. In radar sounding we tipically deal with subsurface mediums which are considered low-loss dielectric and non-magnetic. Accordingly, by assuming $\tan\delta << 1$ (i.e. low-loss dieletric) and $\mu_r = 1$ (i.e. non-magnetic media), (1.12) reduces to:

$$\alpha \approx \pi f \sqrt{\epsilon_0 \mu_0}\sqrt{\epsilon_r}\tan\delta \tag{1.16}$$

Therefore the attenuation in a given medium depends on the wave electromagnetic frequency f and the loss tangent $\tan\delta$. Moreover, the radio wave propagation velocity in the medium depends on ϵ_r while the radio wave absorption on $\tan\delta$. The wave propagation velocity in a given medium is equal to:

$$c = \frac{1}{\sqrt{\mu\epsilon}} = \frac{c_0}{\sqrt{\epsilon_r}} \tag{1.17}$$

where c_0 is the speed of the light and $\mu_r = 1$. The loss tangent value typically depends on the medium temperature and the frequency on the propagating electromagnetic wave, while the value of ϵ_r generally depends on the density and chemical composition of the medium [16].

Reflection and Refraction at a Plane Boundary

In the previous section, we discussed the fundamental physical principles of electromagnetic waves propagation in a physical media. In this section, we discuss the physical phenomena that occur when an electromagnetic wave impinges on a plane boundary which acts a separation between two different mediums. In general, the electromagnetic energy impinging on a plane interface results in two components (see Fig. 1.5). The first component is reflected by the surface while the second one is transmitted through the interface. By defining as $\boldsymbol{E}_i$ the incident electromagnetic field, the following equation

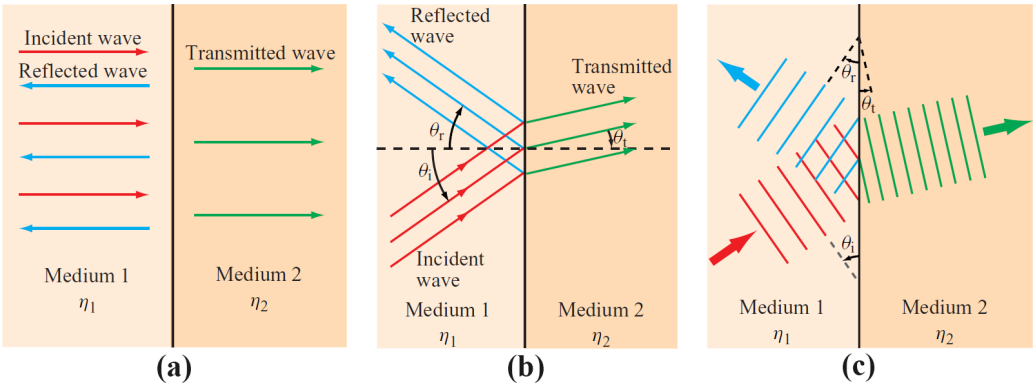

Figure 1.5: Ray representation of wave reflection and transmission at **(a)** normal incidence and **(b)** oblique incidence, and **(c)** wavefront representation of oblique incidence. Image from [15].

holds (under no interface absorption assumption):

$$\boldsymbol{E}_i = \boldsymbol{E}_t + \boldsymbol{E}_r \tag{1.18}$$

where E_t and E_r are respectively the electric field transmitted and reflected component. We define the reflection coefficient Γ a[15]:

$$\Gamma = \frac{\boldsymbol{E}_r}{\boldsymbol{E}_i} \tag{1.19}$$

The transmission coefficient T is equal to:

$$T = \frac{\boldsymbol{E}_t}{\boldsymbol{E}_i} \tag{1.20}$$

By combining (1.18), (1.19) and (1.20), the following relation between Γ and T holds:

$$T = 1 - \Gamma \tag{1.21}$$

By using results from the Snell's law, the reflection coefficient $\Gamma_{\perp,ij}$ and $\Gamma_{\parallel,ij}$ between the i-th and j-th medium for perpendicular and parallel polarization respectively can be computed as:

$$\Gamma_{\perp,ij} = \frac{\eta_j \cos\theta_{inc} - \eta_i \cos\theta_t}{\eta_j \cos\theta_{inc} + \eta_i \cos\theta_t} \tag{1.22}$$

$$\Gamma_{\parallel,ij} = \frac{\eta_j \cos\theta_t - \eta_i \cos\theta_{inc}}{\eta_j \cos\theta_t + \eta_i \cos\theta_{inc}} \tag{1.23}$$

where θ_{inc} is the incidence angle with respect to the surface normal of the impinging electromagnetic wave, θ_t the transmission angle into the medium and η_j the characteristic

impedance of the j-th medium. The following relation between θ_t and θ_{inc} is valid:

$$\sin\theta_t = \sqrt{\mu_i\epsilon_i/\mu_j\epsilon_j}\sin\theta_{inc} \tag{1.24}$$

A very important quantity in radar sounding is the value of the reflection coefficient Γ_{ij} at normal incidence (i.e. $\theta_{inc} = \theta_t = 0$) which is defined as:

$$\Gamma_{ij} = \frac{\eta_j - \eta_i}{\eta_j + \eta_i} \tag{1.25}$$

At normal incidence, the reflection coefficient is independent from polarization of the electromagnetic wave. As stated in section 1.2.2, in many radar sounding practical cases $\mu_r = 1$ and $\tan\delta << 1$. Under this assumption, the reflection coefficient at normal incidence reduces to:

$$\Gamma_{ij} = \frac{1 - \sqrt{\epsilon_{r,j}/\epsilon_{r,i}}}{1 + \sqrt{\epsilon_{r,j}/\epsilon_{r,i}}} \tag{1.26}$$

We will seldom refer to this expression in the following sections and chapters of this thesis. The reflectivity (i.e. power of the reflection coefficient) is equal to $\Gamma_{i,j}^2$ while transmissivity (i.e. power of the transmission coefficient) can be written as $1 - \Gamma_{i,j}^2$.

1.2.3 Acquisition Process and Radar Equation for Sounding

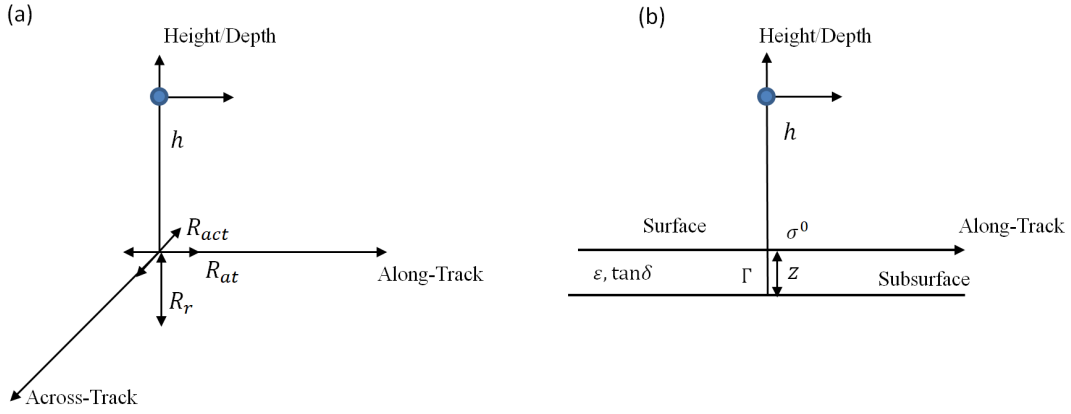

Figure 1.6: Radar Sounding Acquisition geometry (a) 3D view and (b) section view

In the previous section, we discussed the basic principles of electromagnetic waves propagation in a given medium. In this section we combine the previously discussed theory with geometry of acquisition and radar parameters to formulate the radar equation for radar sounding. This is needed in order to evaluate the expected echo power received by the radar from the subsurface. Radar sounders are nadir looking systems which acquire relevant information regarding the subsurface from orbit. The sensor orbit height denoted

as h is typically between 25 km and 500 km. The power density S_1 $[W/m^2]$ impinging on a given surface is equal to (see Fig. 1.6):

$$S_1 = \frac{P_t G}{4\pi h^2}, \tag{1.27}$$

where P_t is the radar transmitted power and G the antenna gain. The denominator is denoted as geometric spreading losses, which accounts for the fact that the radar transmitted energy spreads over a sphere of radius h. Part of this energy is intercepted and scattered back to the radar by the illuminated surface and subsurface. To quantify the target equivalent area we denote as $\sigma^0(\theta_i)$ the radar backscatter coefficient and as A_{ill} the illuminated area. The backscatter coefficient describes the ability of given target to reflect the intercepted energy toward the radar. Different electromagnetic models are available in the literature for the value of σ^0. An overview of the different model for the backscatter coefficient relevant to radar remote sensing of planetary surfaces is presented in [16]. A common and simple assumption is that $\sigma^0 = |\Gamma|^2$ where Γ is defined as in (1.25).
The echo power received by the radar denoted as P_r is equal to [17]:

$$P_r = S_1 \sigma^0 A_{ill} \frac{A_{eff}}{4\pi h^2} = \frac{P_t G^2 \lambda^2 \sigma^0 A_{ill}}{(4\pi)^3 h^4} \tag{1.28}$$

where we denote with $A_{eff} = \lambda^2 G/4\pi$ the effective area of the antenna and with λ the wavelength of the transmitted wave. The formulation of (1.28) only explicits the echo power expected from the surface taking into account (i) the radar transmission parameters (i.e. P_t and G), (ii) the surface backscattering properties and geometry (i.e. σ^0 and A_{ill}) (iii) the reception properties of the system (i.e. A_{eff}), (iv) and the two-way geometry spreading losses.
In radar sounding, we are more interested in estimating the echo power coming from the subsurface from a given dielectric interface positioned at an arbitrary depth z_i, where i is the interface index. To model this, we introduce in the radar equation the notions discussed in 1.2.2 on EM waves propagation in lossy media and reflection and refraction at a plane boundary. Accordingly, the power received by the radar from a given subsurface interface j denoted as $P_{ss,j}$ is equal to:

$$P_{ss,j} = \frac{P_t G^2 \lambda^2 \Gamma_{j,j+1}^2 A_{ill} \prod_{i=0}^{j-1} (1 - \Gamma_{i,i+1}^2)^2 e^{-4\alpha z_j}}{(4\pi)^3 (h + z_j)^4} \tag{1.29}$$

where α is the attenuation constant of (1.16) and Γ is described in (1.25). The product symbol takes into account all the two-way transmissivities previously defined in 1.2.2.

1.2.4 Geometric Resolution

Radar sounder capability of discriminating different targets is expressed by three different quantities namely along-track, across-track and range resolution. The radar range

resolution is equal to:

$$R_r = \frac{c_0}{2B\sqrt{\epsilon_r}} \tag{1.30}$$

where f_0 is the radar carrier frequency and B the radar signal bandwidth. The range resolution is typically in the order of meters and depends on both the signal bandwidth and the subsurface dielectric constant of the medium under investigation. The along-track resolution is computed as:

$$R_{at} = \frac{\lambda h}{2L_s} \tag{1.31}$$

In radar sounding, it is assumed that the length of the synthetic aperture is equal to $L_s = \sqrt{\lambda h/2}$ [18], which corresponds to a resolution equal to $R_{at} = \sqrt{\lambda h/2}$ (i.e. unfocused processing). Usually, the along-track resolution is in the order of hundred metres. The across track resolution is equal to the pulse-limited diameter [17]:

$$R_{act} = 2\sqrt{c_0 h/B} \tag{1.32}$$

The across-track resolution is the main limitation of a radar sounder. Its large value is dictated by the fact that, for mechanical reasons due to the deployment in space, a dipole antenna is usually adopted, resulting in a very large footprint. The large dimensions of the footprint and the fact that no synthetic aperture can be formed in the direction perpendicular to the S/C motion, result in an across-track resolution in the order of thousand meters.

1.2.5 Signal to Noise Ratio and Processing Gains

In section 1.2.3 we discussed the different terms affecting the echo power received by the radar. An important factor affecting the radar sounder capability in detecting the surface and subsurface echo is the noise contribution induced by the electronics and the surrounding environment, which leads to the definition of the signal to noise ratio denoted as SNR.
In planetary radar sounder the galactic noise temperature T_g is many order of magnitude greater than the noise temperature T_e induced by the electronics. Therefore we can assume that the overall noise temperature $T = T_e + T_g$ can be approximated as $T \simeq T_g$. The overall noise power P_n is equal to:

$$P_n = k_b T B \tag{1.33}$$

where k_b is the Boltzmann constant. The signal to noise ratio SNR_j for the $j-th$ subsurface interface is equal to:

$$SNR_j = \frac{P_{ss,j}}{P_n} = \frac{P_t G^2 \lambda^2 \Gamma_{j,j+1}^2 A_{ill} \prod_{i=0}^{j-1}(1-\Gamma_{i,i+1}^2)^2 e^{-4\alpha z_j}}{(4\pi)^3 (h+z_j)^4 k_b T B} \tag{1.34}$$

Radar sounders typically transmits linear frequency modulated pulses(i.e. chirp). By applying a particular processing after signal reception denoted as range compression, this type of waveform allows to increase the SNR by a factor equal to G_r and denoted as range

compression gain. This factor is equal to

$$G_r = B \cdot T_s \tag{1.35}$$

where T_s is the transmitted pulse width. The synthetic aperture processing described in 1.2.4 not only is beneficial for the along-track resolution but it also increase the SNR by a factor determined by the azimuth compression gain denoted as G_{az} which is equal to:

$$G_{az} = \frac{L_s}{v_s \; PRI} = \frac{\sqrt{2\lambda h}}{v_s} PRF \tag{1.36}$$

where $PRF = \dfrac{4v_s}{\lambda} \sin\theta_c$ is the minimum pulse repetition frequency of the radar required for sampling the Doppler spectrum, and v_s is the orbital velocity. For the definition of the clutter angle θ_c the reader can refer to the next section. The SNR including processing gain and denoted as $SNR_{g,j}$ is equal to

$$SNR_{g,j} = SNR_j \; G_{az} \; G_r \tag{1.37}$$

1.2.6 Surface Clutter and Signal to Clutter Ratio

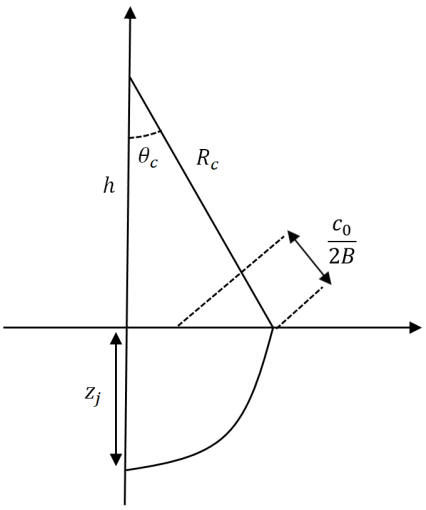

Figure 1.7: Clutter Geometry scheme

In a single given acquisition, planetary sounders antennas (which are assumed to be dipoles due to mechanical reasons) are always pointed toward nadir direction with respect to the surface and illuminate large surface and subsurface regions. The very large antenna footprint implies that off-nadir surface reflections (i.e. surface clutter) of the transmitted signal can be disguised for echoes coming from the interior of the target area. This causes a serious issue in terms of data interpretation. The clutter main driving factors are the surface characteristics such as roughness and electromagnetic backscattering properties.

In this section a mathematical model is provided for evaluating the clutter contribution. The clutter slant range R_c with respect to a given suburface interface j is given by (see Fig. 1.7):

$$R_c = h + z_j\sqrt{\epsilon_{r,j}} \tag{1.38}$$

As a result of the azimuth radar focusing, the equivalent clutter area is given by [19]:

$$A_c = \sqrt{2\lambda h}\frac{c_0}{B\sin(\theta_c)}. \tag{1.39}$$

This area corresponds to the one such that the illuminated points have zero Doppler. The clutter angle θ_c is equal to

$$\theta_c = \cos^{-1}(h/R_c). \tag{1.40}$$

The clutter echo power P_c is equal to

$$P_c = \frac{P_t G^2 \lambda^2 \sigma_s^0(\theta_c) A_c}{(4\pi)^3 R_c^4}, \tag{1.41}$$

The signal to clutter ratio denoted as SCR_j is defined as:

$$SCR_j = \frac{A_{ill}}{A_c}\frac{\Gamma_{j,j+1}^2 \prod_{i=0}^{j-1}(1-\Gamma_{i,i+1}^2)^2}{\sigma_s^0(\theta_c)}e^{-4\alpha z_j} \tag{1.42}$$

The dominant parameters which mainly drive the value of the SCR are the clutter angle θ_c (which controls the value of σ_0) and the attenuation term $e^{-4\alpha z_j}$. Another factor affecting SCR is the sensor height h. By lowering it, the SCR increases due to the direct increase of θ_c.

1.2.7 Conclusions

In this section, we provided the basic concepts and definition needed in the next chapters of the thesis.
Section 1.1 and 1.2.1 provided a general overview on radar and radar sounding and presented an historical overview to put this thesis work into context.
Section 1.2.2 highlighted fundamentals electromagnetic waves propagation concepts relevant to radar sounding. Particular emphasis was placed on concepts such as reflection and refraction at a plane boundary and attenuation in a given media. Sections from 1.2.3 to 1.2.6 were devoted to the description of the high-level equations (e.g.,related to resolution) needed by the radar system engineer for dimensioning a radar sounder, evaluate its acquisition geometry and performance.

Chapter 2

A Multi-Frequency Radar Sounder for Lava Tubes Detection on the Moon: Design, Performance Assessment and Simulations

Lunar lava tubes are subsurface caves which have attracted special interest as they would be suitable shelters for future human outposts on the Moon. Recent evidence from optical images and gravitational anomalies have brought quasi-conclusive proof of their existence, but such investigative means have very limited potential for global mapping of lava tubes. In this chapter[1]*, we investigate the design requirement and feasibility of a radar sounder system specifically conceived for detecting subsurface Moon lava tubes from orbit. This is done by conducting a complete performance assessment and by simulating the electromagnetic signatures of lava tubes using a coherent 3D simulator. The results show that radar sounding of lava tubes is feasible with good performance margins in terms of signal-to-noise and signal-to-clutter ratio, and that a dual-frequency radar sounder operating would be able to detect a vast majority of lunar lavatubes. The electromagnetic simulations show that lava tubes display an unique signature characterized by a signal phase inversion on the roof echo. The analysis is provided for different acquisition geometries with respect to the position of the sounded lava tube. This analysis confirms that orbiting multi-frequency radar sounder can detect and map in a reliable and unambiguous way the majority of Moon lava tubes.*

2.1 Introduction

In the last years, there has been a renewed interest in the exploration of the Moon. Our satellite is a potential strategic outpost with significant raw materials reserves [20]. Lunar lava tubes are considered to be one of the main candidates for a future human outpost

[1]Part of this chapter appears in:
L. Carrer, C. Gerekos and L. Bruzzone, "A Multi-Frequency Radar Sounder for Lava Tubes Detection on the Moon: Design, Performance Assessment and Simulations" in *Planetary and Space Science*. 2018, In press

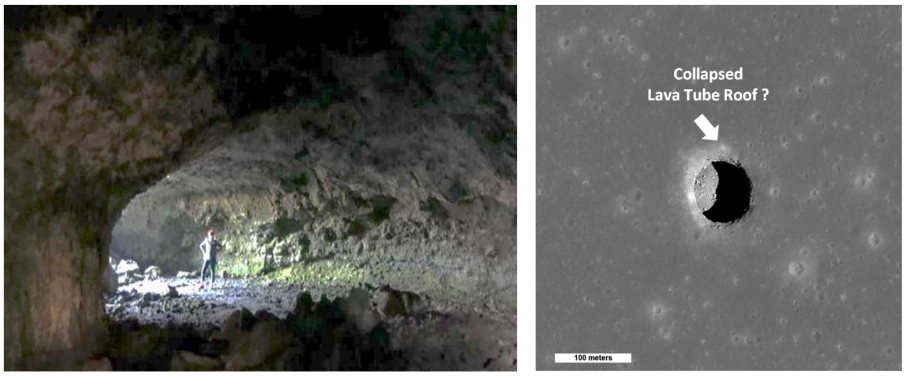

Figure 2.1: (**a**) Example of terrestrial lava tube located at Beauty Cave at Craters of the Moon National Monument, Idaho, US ©Becky Wright (**b**) Mare Tranquillitatis Pit Crater on the Moon. This pit may provide access to a still-open and uncollapsed lava tubes. The pit depth is estimated to be 100 m with width ranging from 100 m to 115 m across. ©NASA/GSFC/Arizona State University

[21]. Lava tubes are natural subsurface conduits which are the result of volcanic activity [22]. They are formed when the upper part of the lava stream cools down and crusts while the lower part of it continues to flow, which results in the formation of an empty cave.

Moon lava tubes are considered to be important and useful structures since they can offer shelter against meteorite impacts, radiation [23] and strong thermal variations taking place on the Moon surface [21]. Recent studies based on gravity measurements [3, 24] and experimental evidence based on terrain mapping camera [25, 26] suggest the hypothesis that there is an abundance of lava tubes on the Moon and their dimensions are consistently larger than the ones found on the Earth. The main reason for their large size, is that the Moon gravity is considerably lower than the terrestrial one.

A complete map of the lava tubes dimension and location will provide important information in view of the exploration and colonization of the Moon. However, the mapping of lava tubes with optical camera has limitations. This is due to the fact that lava tubes are essentially subsurface structures. Radar observations at 70-cm wavelength of the region near Bessel crater in Mare Serenitatis show dark-radar lineaments. This can be interpeted as locally deeper regolith filling voids which might be collapsed portions of once-subsurface lava tubes [27]. Unfortunately, radar waves at centimeter scale cannot penetrate through the regolith.

Planetary radar sounders instruments are particularly suitable for revealing the presence of lava tubes concealed under the Moon surface. Their signal wavelength is in the order of metres. As stated in the introduction of this Thesis, these types of instruments are capable of transmitting pulsed electromagnetic energy and recording any reflection generated by dielectric discontinuities in the target terrain. In particular, by analysing the electromagnetic characteristic of the echo signals generated from both the Moon sur-

face and subsurface, it is possible to understand the physical composition of the lava tube (e.g., whether it is empty or not), its size and shape and the nature of the material forming the lava tube roof and floor.

Two radar sounding missions already probed the Moon surface, NASA's Apollo lunar radar sounder experiment (ALSE) and JAXA's LRS instrument onboard the Kaguya spacecraft [28, 29] but they were not specifically designed for lava tubes detection. Very recently, an intact lava tube was detected in the data acquired by the Lunar Radar Sounder (LRS) [30]. On the one hand, this confirms the potentiality of sounders to detect lava tubes, but on the other hand, LRS has not been specifically designed for the detecting them. Thus, due to its very low spatial resolution (due to a relatively small carrier frequency), it can only detect very large lava tubes. A recent paper has nevertheless highlighted the possibility of detecting lava tubes of sub-resolution size (LRS resolution is 75m)[31]. However, in the paper there are two different interpretation of the lava tube detection results namely (i) the lava tube roof echo is buried in the surface response or (ii) the lava tube echo floor is buried in the roof radar echo. A dedicated, higher-frequency radar, however, would be able to make more conclusive detections of such small and shallow tubes, which are of special importance since they are easier to explore either by manned or unmanned missions.

Sood et al. [32] highlighted the scientific value of a radar sounder mission specifically designed for lava tubes detection. However, they did not provide an assessment analysis on how an hypothetical sounder system will be able to perform for this specific task and how to interpret the returning data. The studies performed on terrestrial lava tubes with ground penetrating radar [33, 34, 35] are of marginal relevance in terms of system design for the planetary radar sounding case. This is due to the very different acquisition geometry and very different radar system technological implementations.

This thesis chapter addresses the problem of detecting lava tubes on the Moon from orbit by using radar sounders. To this extent, the main goals of this paper are (i) the understanding of the design requirements that the sounding system should have for effective lava tube sounding, (ii) a performance assessment as function of the radar, geometric and terrain parameters and (iii) extensive simulations and analysis of the lunar lava tubes electromagnetic responses. The evaluation of the electromagnetic signatures is needed for providing a better understanding of the potential recorded data and thus greatly aiding its scientific interpretation. In our analysis, the allowed lava tube sizes are the ones provided in the recently published structural stability analysis based on gravity measurements presented by Blair et al. [3], which also envelopes the lava tube sizes provided by Coombs et al. [36].

The remainder of this chapter is organized as following. Section 2.2 introduces the acquisition geometry and the subsurface structure assumptions. This serves as a basis for the performance analysis and lava tubes detectability results of Section 2.3. Section 2.4 presents the lava tubes electromagnetic signature analysis for different scenarios. Finally, Section 2.5 addresses the conclusions of this thesis chapter.

2.2 Radar Sounding Acquisition Geometry and Subsurface Structure Assumptions

In this section, we introduce the radar sounding geometry and the main assumptions regarding the Moon's lava tubes structure. This forms the basis for the next sections of the chapter.

Let us consider a radar sensor with carrier frequency assumed to be in the range between 1 MHz to 100 MHz positioned at certain height h from the surface as shown in Fig. 2.2. We define a coordinate reference system composed by three orthogonal axes which are denoted as (i) along-track (i.e., in the direction of the sensor movement), (ii) across-track (i.e., in the direction orthogonal to the sensor movement) and (iii) height/depth direction (which is perpendicular to the other ones previously defined).

We consider the surface substrate to be covered by a regolith layer with average thickness denoted as r_t. We assume the base of the regolith (i.e., the interface between the regolith and the substrate) to be rough. The slope of this rugged base is poorly constrained in the literature. The best piece of evidence available for estimating its order of magnitude (at least in Maria regions) is an optical image of the regolith base on Rima Hadley at Apollo 15 landing site [37] and the pit rims features exposing layered walls of basalt below the regolith [38]. Such optical clues suggest that the regolith base relief is in the order of metres. This is also suggested by the earth-based radar mapping observations at 70-cm wavelength scale [27]. Due to this uncertainty, we follow the same approach described in [39], where the base of the regolith roughness is assumed to be of the same magnitude as the one measured by the Lunar Orbiter Laser Altimeter (LOLA) [40]. A given lava tube is geometrically described by (i) its depth, denoted as h_r, (ii) its width, denoted as w, and (iii) its height, which is set equal to $w/3$. These assumptions are based on the structural analysis of Blair et al. [3]. The work by Coombs et al. [36] on lunar rilles suggests lava tubes of dimension far smaller than the possible maximum dimension specified by Blair et al.[3]. In any case, the numbers given in [36] are covered by the provided lava tube dimensions in [3] and therefore included in our analysis.

The length of a lava tube is not specified and it is assumed to be in the order of kilometres [21, 36]. For what pertains the surface and subsurface materials we denote as ϵ_1, ϵ_2 and ϵ_4 the real part of the dielectric constant of the regolith, the lava tube roof, and lava tube floor (i.e., cave bottom), respectively. The dielectric constant of the cave interior ϵ_3 is assumed to be the one of vacuum and is thus equal to 1.

2.3 Radar Sounder Design and Lava Tubes Detectability Analysis

In this section we study the requirements on the parameters of a radar sounder for detecting lava tubes and perform an analysis of the expected performances and detection capabilities.

In subsection 2.3.1, we assess the regolith contribution to echo power losses. In subsection 2.3.2 the model for the echo power received by the lava tube is presented. Subsections 2.3.3 and 2.3.4 are devoted to the assessment of the signal-to-noise ratio (SNR) and signal-

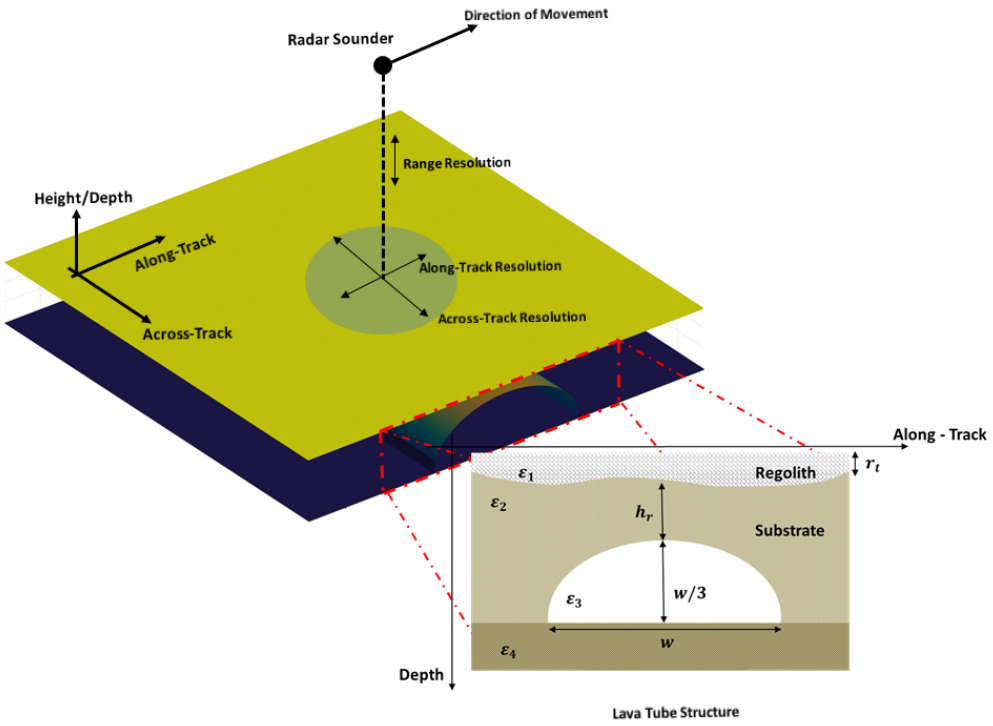

Figure 2.2: Radar sounder acquisition and terrain geometry

to-clutter ratio (SCR), respectively. Finally, subsection 2.3.5 illustrates the results on the lava tube detectability by combining the analyses presented in the previous sections of this chapter. The final assessment provides information on whether a lava tube with given width and depth of the roof can be detected as a function of the probing central frequency.

2.3.1 Regolith Scattering Assessment

Radar sounders propagation losses are classified in three different types namely (i) geometric losses due to the radial distance between the target and the sensor, (ii) attenuation losses induced by the terrain electric properties, and (iii) scattering losses due to heterogeneous inclusions in an otherwise homogeneous medium. In this section we investigate the impact of lunar regolith on both the attenuation and scattering losses, as well as on the dispersion of wide bandwidth waveforms.

Lunar surface is covered by a mantling layer composed of fragmented heterogeneous material denoted as regolith. Its average thickness is estimated to be 5 metres in Maria regions and 12 metres in Highland regions [41]. Being formed by an ensemble of objects (e.g., rocks) of various sizes and shapes, they could potentially give rise to volume scattering phenomena. In general, for longer wavelength the scattering mechanism is dominated by the base of the regolith, whereas, for shorter ones, scattering on and within the regolith is an important factor contributing to losses [16]. Let us analyse a scenario of a

regolith with thickness $r_t = 8.5$ m (i.e., global average over the Moon surface) and rock inclusion modelled as dielectric spheres of radius comprised between $0.6\lambda/(2\pi\sqrt{\epsilon_1})$ and $10\lambda/(2\pi\sqrt{\epsilon_1})$ where $\epsilon_1 = 2.7$ is the average dielectric constant of the soil enclosing the rocks [41, 42]. According to Mie's theory [18], this particular range of radius size is the one that gives the highest backscattering values and, in turn, the greatest losses (i.e., less electromagnetic energy propagates below the regolith).

We assume the volume rock population $N(d_r)[1/m^4]$ as function of the rock diameter d_r to be the one that has been measured by the Surveyor missions [16]. The number of rocks by unit area is equal to [16]

$$N_r = r_t \int_{0.6\lambda/(\pi\sqrt{\epsilon_1})}^{10\lambda/(\pi\sqrt{\epsilon_1})} N(d_r)\ dd_r. \tag{2.1}$$

From the results reported on Fig. 2.3 we can infer that, even in a worst case scenario, the number of rocks comprised in the regolith by unit area having a size comparable to the incident wavelength is negligible over the entire frequency range of interest typical of radar sounding. The only exception to the general trend of Fig. 2.3 is the one inferred from Surveyor 7 data, which highlights marginal volume scattering effects for sounding frequencies higher than 80 MHz. However, recent discoveries suggest that the highest concentration of lava tubes lies in the Mare regions [38, 26]. The Surveyor 7 sampling site was located in the Highland plains region near Tycho crater, thus, in our case, of less significance when compared to Mare regions data where all the other Surveyor sampling sites were located.

Another potential contribution to echo power loss results from voids inclusion in the regolith material. The Maxwell-Garnett mixing model describes dielectric constant of the solid/pore filling mixture ϵ_m at different depths in the following way [43]:

$$\epsilon_m(z) = \epsilon_1 \frac{1 + 2\Omega(z)\xi}{1 - \Omega(z)\xi} \tag{2.2}$$

$$\xi = \frac{\epsilon_i - \epsilon_1}{\epsilon_i + 2\epsilon_1} \tag{2.3}$$

where ϵ_i is the dielectric constant of the inclusion assumed to be vacuum (i.e. $\epsilon_i = 1$). The model of the decline of porosity Ω as function of the depth z due to the lithostatic pressure is equal to [44]:

$$\Omega(z) = \Omega(0)e^{-z/K} \tag{2.4}$$

where $\Omega(0)$ is the surface porosity and K is a decay constant. $\Omega(z)$ and $\Omega(0)$ are porosity percentage divided by 100. The decay constant for the Moon is equal to $K = 6.5$ Km [44]. In this case, the two-way transmission coefficient between the regolith and the substrate T_{reg} is equal to;

$$T_{reg}(z) = (1 - \Gamma_{reg}^2(z))^2 \tag{2.5}$$

where Γ_{reg} is the porous base of the regolith reflection coefficient defined as:

$$\Gamma_{reg}(z) = \frac{1 - \sqrt{\epsilon_2/\epsilon_m(z)}}{1 + \sqrt{\epsilon_2/\epsilon_m(z)}} \tag{2.6}$$

The real part of the permittivity and the loss tangent decrease when increasing the porosity. This implies that the reflection coefficient $\Gamma_{reg}(z)$ increases or decreases with the porosity depending on the value of ϵ_1 and ϵ_2. By assuming $2.5 \leq \epsilon_1 \leq 4$ and $4 \leq \epsilon_2 \leq 8$ [41, 42], the resulting decrease or increase of the transmission coefficient T_{reg} is smaller than 1 dB and thus negligible. The total two-way radar signal attenuation $L_{reg} = 0.18\sqrt{\epsilon_m(z)}\ \tan\delta\ z\ [dB/MHz]$ [45], where $\tan\delta$ is the loss tangent, decreases as function of the porosity and the depth. Its variation can be considered negligible at low frequencies (e.g., 10 MHz). At 100 MHz, considering worst case parameters, there is a reduction in total signal attenuation up to 5dB as shown in Fig. 2.4). The values assumed for the loss tangent (i.e. 0.01 to 0.03) are in the upper range of the ones measured for the Moon basaltic material in our frequency range [46] and thus should be considered as worst case.
The waveform dispersion in the regolith is related to the frequency dependence of ϵ_1 and $\tan\delta$. If the phase of the signal is a linear function of frequency (i.e., linear phase condition), there is no dispersion (i.e. temporal smearing) of the radar signal and thus no distortion. In the frequency range 1 MHz to 100 MHz, the tangent loss is always much smaller than one [47] and the real part of the dielectric constant has very small variations with frequency [47]. Under this assumptions of low-loss dielectric [18], linear phase condition of the signal in the regolith is met and thus there is no waveform dispersion.
According to the above analysis, we consider volume scattering, voids inclusions and signal phase dispersion effects negligible and thus in the following we will only take into account the regolith geometric and attenuation losses.

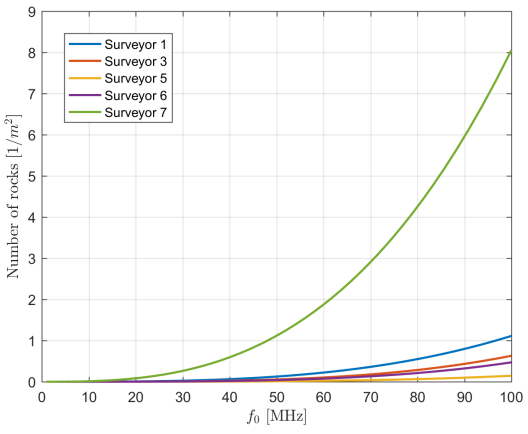

Figure 2.3: Number of rocks $[1/m^2]$ contributing to volume scattering as function of the carrier frequency f_0 and the Surveyor sampling site

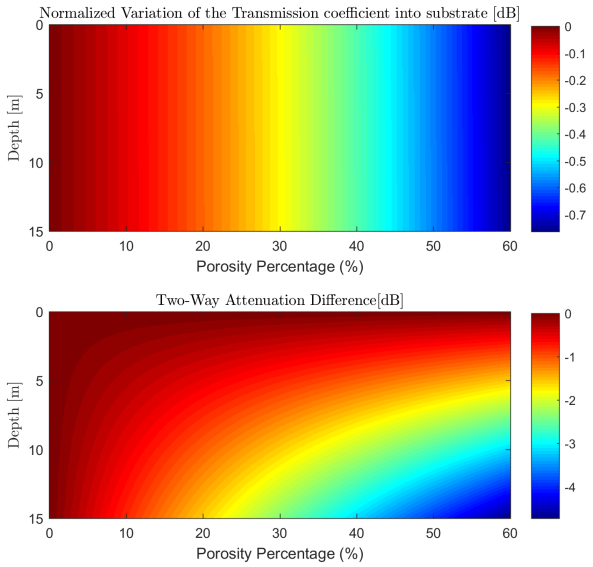

Figure 2.4: Example of normalized variation of the transmission coefficient and attenuation as function versus the regolith porosity percentage, $\epsilon_i = 1$, $\epsilon_1 = 4$, $\epsilon_2 = 8$, $\tan\delta = 0.03$, $f_0 = 100$ MHz

2.3.2 Lava Tube Floor Echo Power

The radar echoes of interests are those arising from the lava tube roof and floor. The radar echo undergoing the most attenuation is the one generated by the lava tube floor. Accordingly, we model the echo power received from it as function of the radar and surface/subsurface parameters. The echo power density S_i $[W/m^2]$ measured at the radar antenna (without considering the terrain attenuation and backscattering) is equal to:

$$S_1 = \frac{P_t G^2 \lambda^2}{(4\pi)^3 R_e^4}, \tag{2.7}$$

where P_t is the radar transmitted power, G the antenna gain and R_e the effective radar distance to the target, which is equal to:

$$R_e = h + r_t/\sqrt{\epsilon_1} + h_r/\sqrt{\epsilon_2} + w/3. \tag{2.8}$$

The effective radar distance is the one from the radar to the floor of the lava tube and it depends on the regolith depth r_t, the depth of lava tube roof h_r and the lava tube height (which is assumed equal to $w/3$, where w is the width of the lava tube). The effective distance is reduced in both the regolith and lava tube roof medium according to the decrease in velocity of the electromagnetic wave.

The echo power density S_i is reduced by the two-way attenuation the transmitted

pulse experiences as it travels through both the regolith and lava tube roof such that:

$$S_2 = S_1 e^{-2\alpha f_0(\sqrt{\epsilon_2}h_r + \sqrt{\epsilon_1}r_t)}, \tag{2.9}$$

where $\alpha = 2\pi/c_0 \tan\delta$ is the two-way attenuation constant. We assume the loss tangent $\tan\delta$ to be equal for both the regolith and the lava tube roof.

At each interface (i.e., dielectric contrast between different materials) part of the energy is reflected toward the radar and part of it continues to travel downwards into the target terrain. Therefore the power density S_2 is further reduced by the various interfaces reflections such that:

$$S_3 = S_2 \; T_{01}^2 \rho_{12} T_{12}^2 T_{23}^2, \tag{2.10}$$

where the transmission coefficient T_{ij} between the i-th and j-th medium is equal to $T_{ij} = 1 - \Gamma_{ij}$.The Fresnel reflection coefficient at normal incidence denoted as Γ_{ij} defined as follows:

$$\Gamma_{ij} = \left| \frac{1 - \sqrt{\epsilon_j/\epsilon_i}}{1 + \sqrt{\epsilon_j/\epsilon_i}} \right|^2. \tag{2.11}$$

The transmission factors are related to the vacuum-regolith, regolith-roof and roof-cave interfaces.
The regolith-roof interface is the one between the regolith and the substrate.
As discussed in Section 2.2, this interface is rough. Accordingly, let ρ_{12} be the two-way rough surface transmission power loss with respect to the specular return [48, 49, 50]:

$$\rho_{12} = J_0^2(\frac{\psi^2}{2}) e^{-\psi^2} \tag{2.12}$$

where $J_0(.)$ is the zero-order modified Bessel function and ψ is the RMS phase variation induced by the rough surface on the transmitted signal which is equal to:

$$\psi = \frac{4\pi\sigma_b}{\lambda}(\sqrt{\epsilon_2} - 1) \tag{2.13}$$

The RMS variation of surface height σ_b is referred to the base of the regolith. As already stated in Section 2.2, the base of the regolith roughness is assumed to be of the same magnitude as that measured by LOLA [40]. Therefore σ_b can be computed from the surface slope derived from LOLA data.
To retrieve the lava tube floor echo power P_f $[W]$, the power density S_3 is multiplied by radar cross-section of the lava tube floor as follows:

$$P_f = S_3 \; \sigma_f^0(0) A_f, \tag{2.14}$$

where $A_f = \min\{w, \sqrt{2\lambda h}\} \cdot \sqrt{2\lambda h}$ is the equivalent area of the lava tube floor. If the lava tube width is greater than the first Fresnel diameter, we consider a rectangular area formed by the latter. The length of the lava tube is assumed to be in the order of kilometres [21], thus it is appropriate to consider only the contribution of the coherent

part of the scattered field given by the first Fresnel diameter. We denote as $\sigma_f^0(0)$ the backscattering cross-section normalized to unit area defined as follows [51]:

$$\sigma_f^0(\theta) = \frac{C_f \Gamma_{34}}{2} \frac{1}{[\cos^4(\theta) + C_f \sin^2(\theta)]^{3/2}}. \tag{2.15}$$

Hagfor's model is particularly appropriate because it has been already applied and validated on Moon data. The value of the constant $C_f = 1/s_f^2$ can be computed assuming the reference slope to be equal to $s_f = tan^{-1}(\frac{\sigma_f}{w})$. There is no available data regarding the rms value of the floor height distribution σ_f. We know from terrestrial lava tubes that the floor relief can vary from relatively smooth to very rough and knobby [21]. Moreover, this variability occurs at scales considerably smaller than the lava tube cross-sectional dimension. Assuming that the tube height is equal to $w/3$, and assuming a Gaussian distribution for the floor height variation inside the lava tube, we can safely constraint the rms height such that $4\sigma_f = w/3$. This, in turn, provides the value of the reference slope assumed equal to $s_f = \tan^{-1}(\frac{1}{12}) = 0.0831\,\text{rad}$.

2.3.3 Signal to Noise Ratio (SNR)

The signal-to-noise ratio is expressed with reference to the power scattered by the floor of the lava tube as follows [52]:

$$SNR = \frac{P_f}{P_n} = \frac{P_t G^2 \lambda^2 \sigma_f^0(0) A_f}{(4\pi)^3 (h + r_t + h_r/\sqrt{\epsilon_1} + w/3)^4} \frac{T_{01}^2 \rho_{12} T_{12}^2 T_{23}^2 e^{-2\alpha f_0(\sqrt{\epsilon_2} h_r + \sqrt{\epsilon_1} r_t)}}{k_b T_e(f_0) B}, \tag{2.16}$$

where the noise power is equal to $P_n = k_b T_e(f_0) B$, k_b is the Boltzmann constant and $T_e(f_0)$ is the frequency dependent galactic noise temperature[53]. It is clear from equation (2.16) that the attenuation term and, in turn, the depth of lava tube roof h_r play a major role in the SNR performance of the radar system. Another important factor affecting the SNR is the two-way rough surface transmission term $\rho_{12} \sim e^{-f_0^2}$. We constrain the value of σ_b by considering the average range of slope values for Highlands and Maria region provided in [38]. The derived average values of σ_b are 0.6 m and 2.2 m for the Maria and Highlands regions respectively. The analysis of the two-way rough surface transmission losses of equation (2.12) shows that the frequency range 80 MHz to 100 MHz is particularly affected by the roughness of the base of the regolith in both Maria and Highlands regions (see Fig. 2.5).
The range compression gain is equal to

$$G_r = B \cdot T_s, \tag{2.17}$$

where T_s is the transmitted pulse width. The azimuth compression gain is equal to

$$G_{az} = \frac{L_s}{v_s \; PRI} = \frac{\sqrt{2\lambda h}}{v_s} PRF, \tag{2.18}$$

where $PRF = \frac{4v_s}{\lambda} \sin\theta_c$ is the minimum pulse repetition frequency of the radar required for sampling the Doppler spectrum, and v_s is the orbital velocity. For the definition of the clutter angle θ_c the reader can refer to the next section.

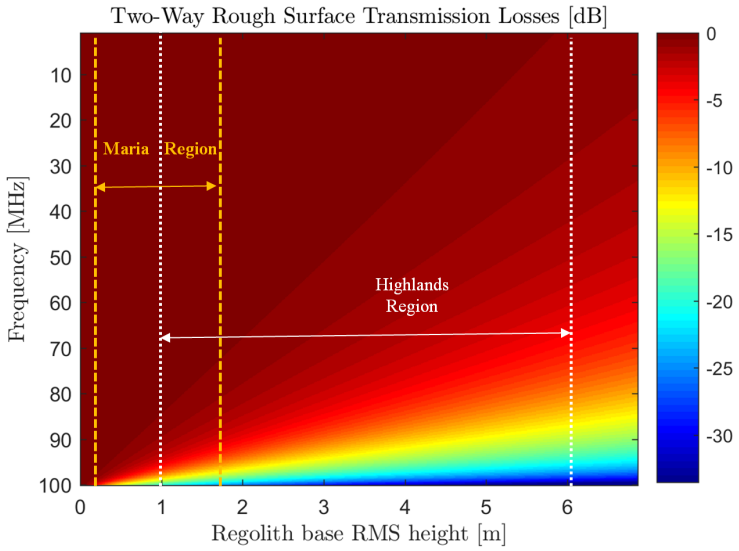

Figure 2.5: Two-Way rough surface transmission losses with respect to specular return induced by the regolith base as function of both its RMS variation of the height and the central frequency. Due to lack of knowledge regarding the roughness of the regolith base, range of plausible RMS height values for the Maria Region and the Highlands Region were calculated assuming that the base of the regolith roughness is of the same magnitude as that of the lunar surface which is constrained by LOLA [40]. In this example, the value of the substrate dielectric constant is assumed equal to $\epsilon_2 = 6$

.

2.3.4 Clutter Model and Signal-to-Clutter Ratio (SCR)

In radar sounding, clutter is defined as off-nadir echoes coming from the surface which may mask the echoes of interest coming from the subsurface. This generates ambiguities and may hinder data interpretation. The clutter slant range (see Fig. 2.6) with respect to the lava tube floor is equal to:

$$R_c = h + r_t\sqrt{\epsilon_1} + h_r\sqrt{\epsilon_2} + w/3. \tag{2.19}$$

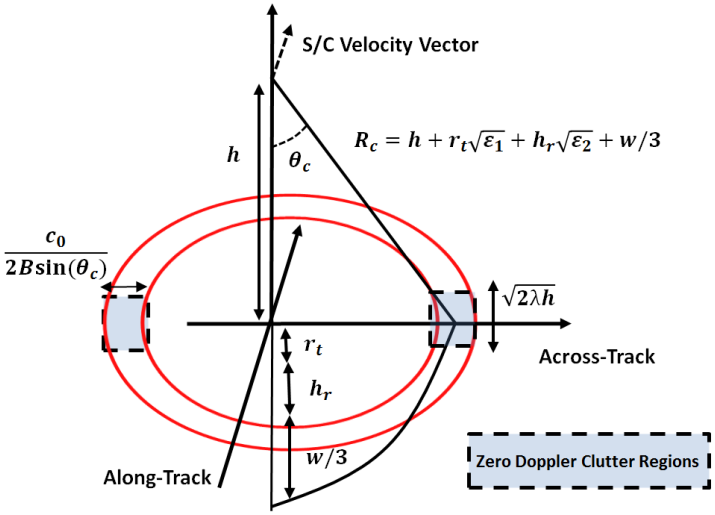

Figure 2.6: Illustration of the Clutter Geometry

As a result of the azimuth radar focusing, the equivalent clutter area is given by [19]:

$$A_c = \sqrt{2\lambda h}\frac{c_0}{B\sin(\theta_c)}. \tag{2.20}$$

This area corresponds to the one such that the illuminated points have zero Doppler. The clutter angle θ_c is equal to

$$\theta_c = \cos^{-1}(h/R_c). \tag{2.21}$$

The clutter echo power P_c is equal to

$$P_c = \frac{P_t G^2 \lambda^2 \sigma_s^0(\theta_c) A_c}{(4\pi)^3 R_c^4}, \tag{2.22}$$

where the surface back-scattering coefficient is expressed as for the Hagfor's model:

$$\sigma_s^0(\theta) = \frac{C_s \Gamma_{01}}{2}\frac{1}{[\cos^4(\theta) + C_s \sin^2(\theta)]^{3/2}}, \tag{2.23}$$

where $C_s = 1/s(\lambda)^2$ and $s(\lambda) = s_0\ (\lambda/\lambda_0)^{H-1}$ is the frequency dependent RMS slope of the surface [54], H is the surface Hurst exponent and s_0 the reference RMS slope. The reference wavelength and slopes are assumed equal to $\lambda_0 = 17\,\mathrm{m}$ and $s_0 \leq 25\,\mathrm{deg}$ respectively [40]. The value of the Hurst exponent can be assumed in the range $0.7 \leq$

$H \leq 1$ [40]. The signal to clutter ratio denoted as SCR is defined as:

$$SCR = \frac{P_f}{P_c} = \left(\frac{h + r_t\sqrt{\epsilon_1} + h_r\sqrt{\epsilon_2} + w/3}{h + r_t/\sqrt{\epsilon_1} + h_r/\sqrt{\epsilon_2} + w/3}\right)^4 \frac{\sigma_f^0(0)}{\sigma_s^0(\theta_c)} \\ T_{01}^2 \rho_{12} T_{12}^2 T_{23}^2 \frac{A_f}{A_c} e^{-2\alpha f_0(\sqrt{\epsilon_2}h_r + \sqrt{\epsilon_1}r_t)}. \tag{2.24}$$

The dominant parameters which mainly drive the value of the SCR are the clutter angle θ_c (which controls the value of σ_0) and the attenuation terms $e^{-2\alpha f_0\sqrt{\epsilon_2}h_r}$ and $\rho_{12} \sim e^{-f_0^2}$. For a fixed f_0, the sounding of large lava tubes (in terms of width) is less affected by clutter when compared to small lava tubes. As w increases (note that the lava tube height is assumed equal to $w/3$), the clutter angle increases and thus σ_s^0 decreases. This results in an improvement of the SCR. Another factor affecting SCR is the sensor height h. By lowering it, the SCR increases due to the direct increase of θ_c.

In equation (2.24) the most difficult term to analyse is the one accounting for the surface and subsurface backscattering, which we denote as $\Delta\sigma_0 = \sigma_f^0(0)/\sigma_s^0(\theta_c)$.

Assuming a worst case scenario such that $\epsilon_2 = 8$ and $\epsilon_3 = 4$, Fig. 2.7 shows that, even if for small surface slopes and small clutter angles θ_c, the clutter backscattering contribution (i.e., σ_s^0) does not considerably degrade the SCR performance. Therefore we can conclude that the dominant factor for SCR degradation is the subsurface attenuation and the relief at the base of the regolith.

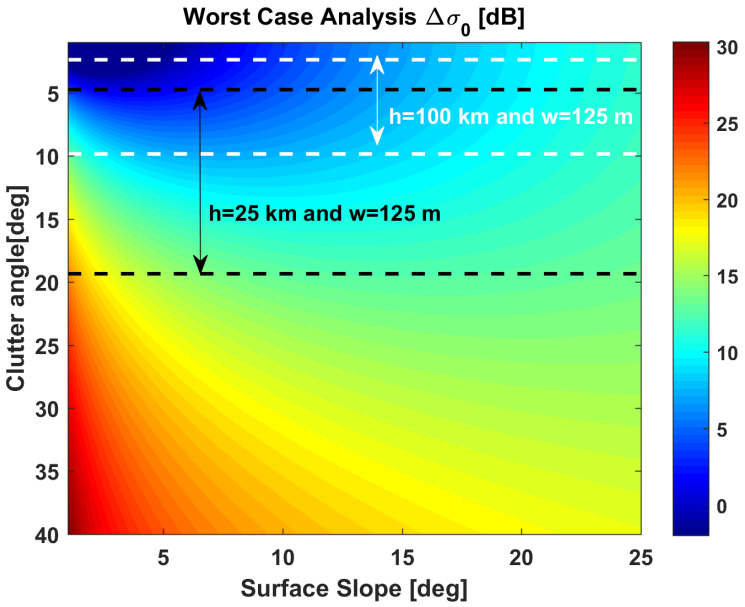

Figure 2.7: Worst case analysis for the back-scattering ratio $\Delta\sigma_0 = \sigma_f^0(0)/\sigma_s^0(\theta_c)$ [dB] between the subsurface and surface versus the clutter angle θ_c and the surface RMS slope s. The dashed lines are constraining the values of the clutter angle θ_c as function of the S/C height h, the lava tube roof h_r and the lava tube width w. The analysis is performed for the lava tube of width $w = 125$ which is the one resulting in the smallest clutter angles thus considered worst case.

2.3.5 Lava Tubes Detectability

The analyses presented in sections 2.3.3 and 2.3.4 highlight that the main driving factor affecting the radar performance is the substrate attenuation on the radar signal which mainly depends on the depth of the lava tube roof h_r, the central frequency f_0 and the RMS variation of surface heights of the regolith-substrate interface σ_b for fixed subsurface properties in terms of complex dielectric constant. The lava tube width w plays a secondary role in terms of SCR and SNR when compared to the depth of lava tube roof. Fig. 2.8 shows the maximum depth at which a lava tube can be detected for different carrier frequencies as function of $\tan\delta$ and σ_b. As expected, the maximum detectable depth of the lava tube roof is strongly dependent on f_0. Fig. 2.8 (b) shows that the base of the regolith roughness strongly impacts performance in the range 80 MHz to 100 MHz. Performances have been evaluated considering radar system parameters based on previous Moon radar sounding missions [29]. Accordingly, the transmitted power is set equal to $P_t = 800\,\mathrm{W}$, the antenna gain is equal to $G = 1\,\mathrm{dB}$, the pulse repetition frequency $PRF = 500\,\mathrm{Hz}$, the pulse width $T_s = 100\,\mu\mathrm{s}$ and the S/C height equal to $h = 25\,\mathrm{km}$. For what regards the Moon surface parameters, we assume a representative and rather challenging scenario, from the attenuation point of view, such that $H = 0.8$, $s_0 = 2.5\,\mathrm{deg}$, $\epsilon_1 = 2.7$, $\epsilon_2 = 4$, $\epsilon_4 = 4$, $\tan\delta = 0.01$, $r_t = 8.5\,\mathrm{m}$ and $\sigma_b = 0.6$ m. These values are in line with what discussed in the previous sections [41, 42, 40]. Fig. 2.9 shows the results regarding SNR, SCR and detection matrix for three different carrier frequencies namely 10 MHz, 50 MHz and 100 MHz. The detection matrix is displayed in the same fashion as the structural stability one presented in [3]. The lava tubes dimension we consider feasible and for which detectability is provided are the stable and quasi-stable configurations for both the lithostatic and Poisson stress state in the material models as in [3]. Accordingly, performance for unstable lava tubes were not computed.

A lava-tube is considered detectable if, for a specific combination of lava tube roof depth h_r and lava tube width w, all of the following conditions holds true: (i) $SCR > 0$ (ii) $SNR > 10$ dB, (iii) h_r greater than two times the range resolution defined as in Section 1.2.4, (iv) w greater than the along-track resolution defined as in Section 1.2.4. It is clear from Fig. 2.9 that for $f_0 = 10\,\mathrm{MHz}$ only very large lava tubes can detected. These large lava tubes are detected with very solid performances in terms of SNR. On the other hand, for a frequency $f_0 = 100\,\mathrm{MHz}$, small lava tubes can be detected and with a lower SNR when compared to the 10 MHz sounding case. Finally, the $f_0 = 50\,\mathrm{MHz}$ sounding frequency is suitable for detecting medium size lava tubes. Therefore there is a clear correlation between the sounding central frequency and the dimension of the lava tubes that can be detected with it.

By further analysing the results of Fig. 2.9 we can highlight a general scheme in terms of lava tubes detection as function of their width w and lava tube roof depth h_r. With reference to Fig. 2.10, the area of feasible lava tube detection presented in blue is constrained by three different sub-bands. Each sub-band thickness depends on certain radar performance factors which are mainly affected by the selected radar central frequency f_0.

As a conclusion, it is therefore clear that a multi-frequency radar sounder will allow to map the vast majority of all the feasible and potential lava tube dimensions. This

can be done by selecting at least two frequencies, one from the lower and one from the upper part of the 1 to 100 MHz frequency range. As an example, Fig. 2.11 shows that a radar sounder with lower carrier frequency equal to 10 MHz and higher one of 100 MHz is potentially able to detect the vast majority of the allowed (in terms of structural stability) lava tubes sizes if $\tan\delta = 0.01$. However, to take margin against the basalt surface relief and loss tangent variation which has a major impact on performance (see Fig. 2.8 (b)), a central frequency in the range 60 to 65 MHz is a more reasonable choice (see Fig. 2.11 (c)). for detecting small lava tubes under the 50 % fractional bandwidth assumption.

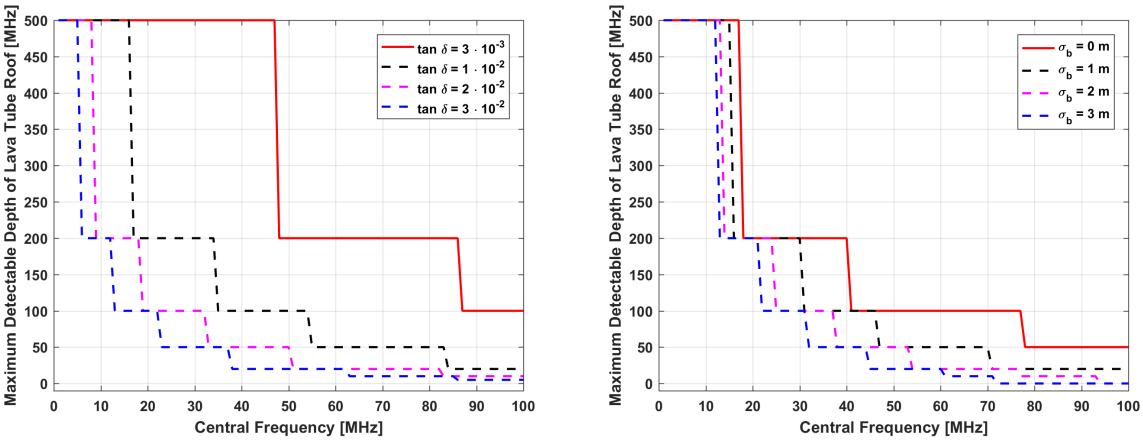

(a) (b)

Figure 2.8: (a) Maximum detectable depth of lava tube roof h_r versus the carrier frequency f_0 for different values of (a) loss tangent and (b) basalt substrate RMS variation of surface heights. The depth of lava tube roof is discretized according to the structural stability matrix of [3].

2.4 Lava Tubes Electromagnetic Signatures

This section is devoted to the analysis of the electromagnetic signature of lava tubes of different dimensions, in the frequency range of 1 MHz to 100 MHz identified in the previous section. We investigate the radar returns resulting from a range of lava tubes geometries using of a multi-layer coherent simulator. Lava tubes echoes are generated for different radar central frequencies and different crossing angles assuming to transmit with a linear chirp weighted by an Hann window. Range-compression is then applied to the simulated data. The crossing angle is defined as the angle at which the spacecraft ground trace intersects the line perpendicular to the lava tube axis. The coherent simulator allows us to analyse both the received signals power and the phase information.

Although the simulator works with interfaces represented by 3D surfaces, it is possible to simulate 3D volumes by cladding two properly-chosen surfaces together, as shown in Fig. 2.12. Lava tubes are modelled in this fashion, where one surface containing an open half-cylinder is clad to a flat surface underneath, thus adding a ground to the lava tube. It is worth noting that a minor issue arises when modelling the tubes this way. Because

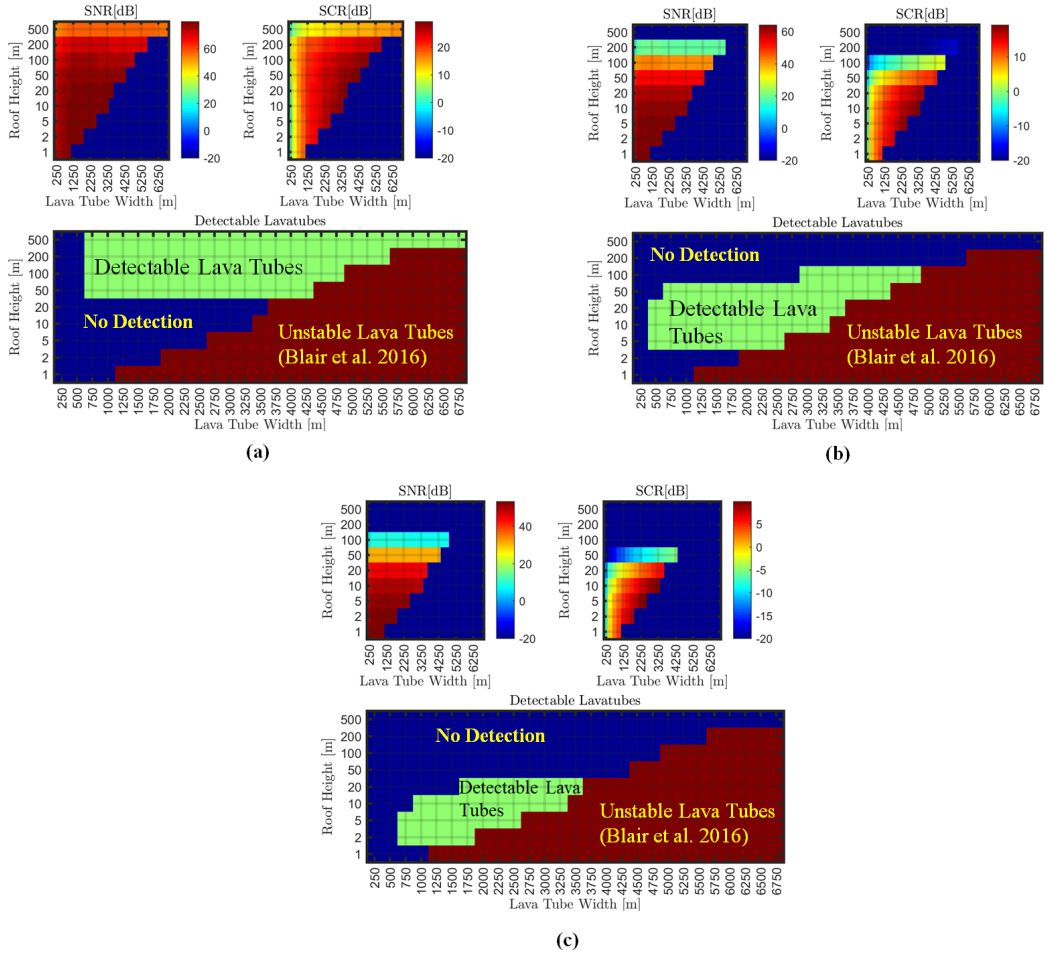

Figure 2.9: SNR, SCR and detectability matrix for (a) $f_0 = 10$ MHz (b) $f_0 = 50$ MHz and (c) $f_0 = 100$ MHz assuming loss tangent equal to $\tan\delta = 0.01$ and RMS height variation of basalt substrate equal to $\sigma_b = 0.6$ m.

the simulator processes the subsurface layers in an iterative way, a reflection is generated by the layer containing the open half-cylinder, but this feature is easily recognizable in the resulting radargram and does not endanger the general picture of the simulation. For what pertains the subsurface geoelectrical properties, we assume the medium between the lunar surface and the lava tube roof to be basalt with real part of the dielectric constant equal to $\epsilon_{r,1} = 4$ and tangent loss equal to $\tan\delta_1 = 0.01$. The lava tube floor is described by a dielectric constant equal to $\epsilon_{r,3} = 4$. We consider the space between the lava tube roof and floor as empty such that $\epsilon_{r,2} = 1$.

The rest of this section is organized as follows. In section 2.4.1 we investigate the electromagnetic signature of lava tubes of different sizes assuming an ideal geometry such that the lunar surface is flat and the lava tubes are modelled with perfect geometric shapes. This is done in order to establish clear reference cases for the lava tubes electromagnetic

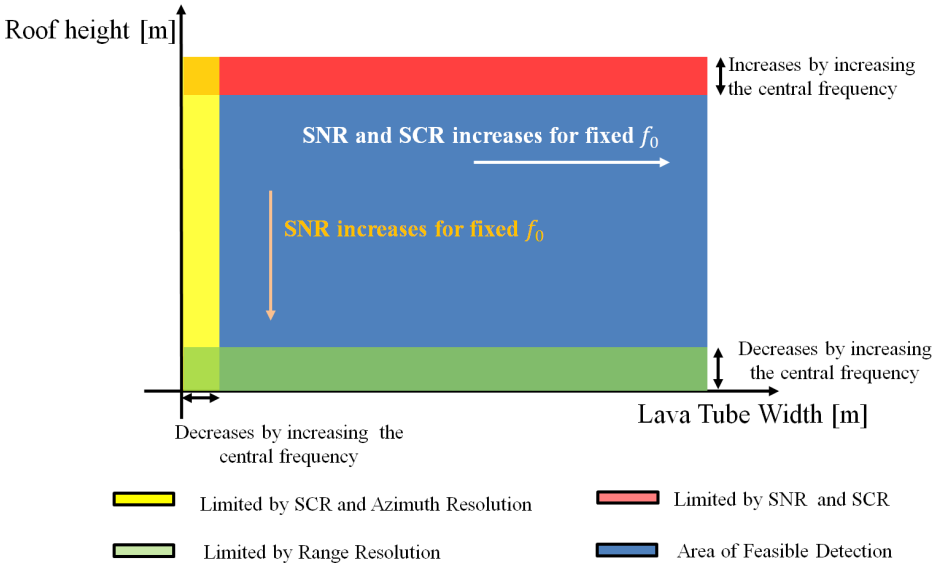

Figure 2.10: General scheme of lava tube detection versus the lava tube width and the roof height. The area of feasible lava tube detection is depicted in blue. The size of this area is bounded by three smaller sub-bands which size depends on the value of the radar parameters. The radar central frequency is the main factor affecting the size of these sub-bands. In terms of central frequency f_0, (i) the red band increase is proportional to $\sim exp(f_0^2)$ due to basalt substrate roughness,(ii) the green band decreases as $\sim f_0$ due to the larger exploitable bandwidth and thus improved range resolution and (iii) the yellow band decrease as $\sim 1/\sqrt{f_0}$ as across-track resolution is dictated by the first Fresnel zone.

responses. Then, in section 2.4.2, we present simulations of more realistic scenarios. This is done by modelling irregular lava tubes and a lunar surface characterized by the presence of craters and significant roughness.

2.4.1 Lava Tubes Electromagnetic Signatures : Ideal Geometry

We investigated four lava tubes of different sizes selected on the basis on the structural stability analysis of [3]. The simulations on the selected cases where performed at two different combinations of central frequencies and bandwidths : (i) $f_{0,1} = 10\,\text{MHz}$ and a bandwidth $B_1 = 5\,\text{MHz}$, and (ii) $f_{0,2} = 100$ MHz and $B_2 = 50\,\text{MHz}$. The simulations were performed for the following four scenarios : (a) perpendicular (to the lava tube axis), (b) centred parallel, (c) off-centre parallel, and (d) oblique with an angle of 45°, all of which are represented schematically in Fig. 2.12. The radar altitude was set to $h = 100\,\text{km}$ for all runs, and the radar peak power to $P = 800\,\text{W}$. The footprints considered have a radius equal to twice the pulse-limited zone radius of each instrument, that is, $A_1 = 4897\,\text{m}$ and $A_2 = 1549\,\text{m}$. The investigated cases, covering different lava tubes sizes, are summarized

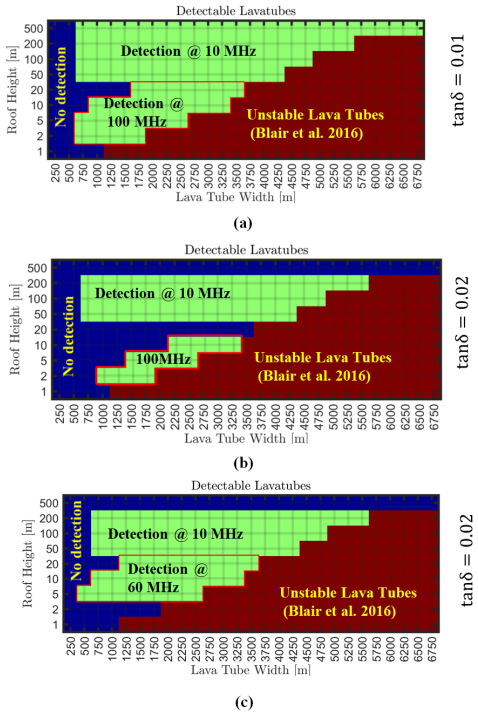

Figure 2.11: Examples of detectable lava tubes by combining the sounding at two different carrier frequencies. (a) $\tan\delta = 0.01$, $\sigma_b = 0.6$ m, lower frequency equal to 10 MHz, higher frequency equal to 100 MHz (b) $\tan\delta = 0.02$, $\sigma_b = 0.6$, lower frequency equal to 10 MHz, higher frequency equal to 100 MHz (c) $\tan\delta = 0.02$, $\sigma_b = 0.6$ m, lower frequency equal to 10 MHz, higher frequency equal to 60 MHz.

in Table 2.4.1.

In order to establish a series of clear reference cases, the lava tubes are modelled with perfect linearity and curvature. The lunar surface is modelled as flat. To avoid ray-tracing artifacts, some minimal roughness was added to every interface by adding a surface modelled as fractional Brownian motion with a Hurst's coefficient $H = 0.1$ and a topothesy $T = 0.26$ m.

Experimental results show that the lava tubes signatures for the parallel and oblique crossing cases are composed of two vertically-aligned ensembles of hyperbolas (see Fig. 2.13). The upper and lower features correspond to the lava tube roof and the floor, respectively. The two hyperbolas brightness is similar. The finer characteristics of these signatures strongly depend on the probing central frequency and associated bandwidth. For lava tubes sounded with the 100 MHz radar, the signatures are usually very clear and reduce to two simple hyperbolas corresponding to the roof and to the floor (see Fig. 2.13). For the 10 MHz central frequency case, each of the two traces is rather made of one bright hyperbola and some dimmer, more chaotic echoes underneath as shown, for example, in Fig. 2.13. We interpret the brighter hyperbola of the upper trace as generated

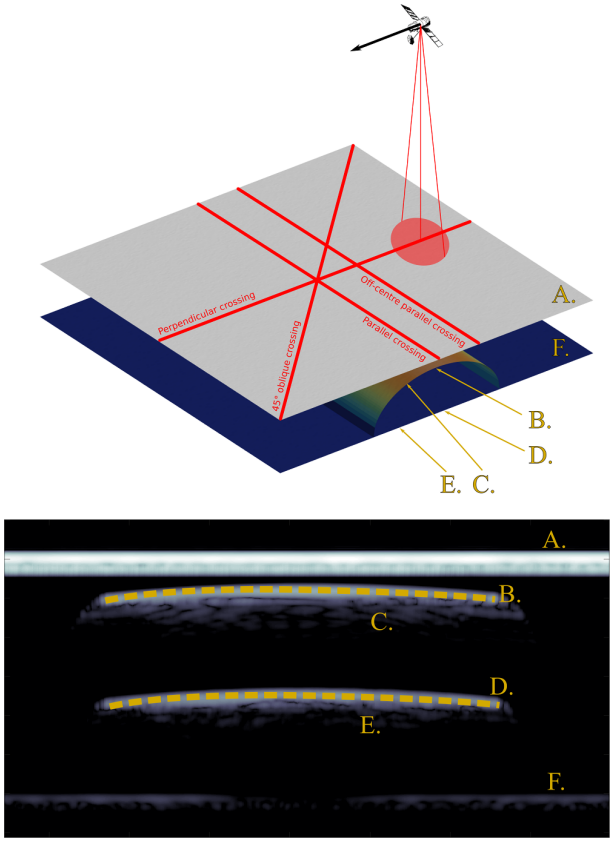

Figure 2.12: Illustration of the different acquisition geometries considered in the simulations (top), along with an example of simulated radargram for a perpendicular crossing direction (bottom), where key features of the terrain are cross-references with features on the radargram : A. surface, B. tube apex, C. tube walls, D. central portion of the floor, E. remainder of the floor, F. parasitic subsurface resulting from the terrain modelling (disregarded in the analysis).

by the apex of the tube (the centre of the floor for the lower part of the signature), and the more random pattern beneath it, from the tube walls (from off-nadir floor portions). These diffuse radar returns are less prevalent in the 100 MHz radar case due to the higher subsurface attenuation. The above-mentioned features are summarized in Fig. 2.12.

The only noticeable difference between the two crossing scenarios is that the features are spatially more stretched in the oblique crossing case when compared to the parallel one (see Fig. 2.13). The stretching factor is equal to $\cos\theta^{-1}$, where θ is the angle between the spacecraft ground trace direction and the line perpendicular to the lava tube axis.

In the parallel crossing case, the roof and floor appear as two parallel lines (see Fig. 2.16). Similarly to the previous case, there are some diffuse spurious reflections, which are more prominent in the 10 MHz case. The 100 MHz radargrams simply display two lines, as those off-nadir subsurface echoes are much more strongly attenuated than in the 10 MHz case. There are no significant differences between a centred crossing and an off-centre crossing except from a slight variation of the relative power levels of the tube and floor echoes.

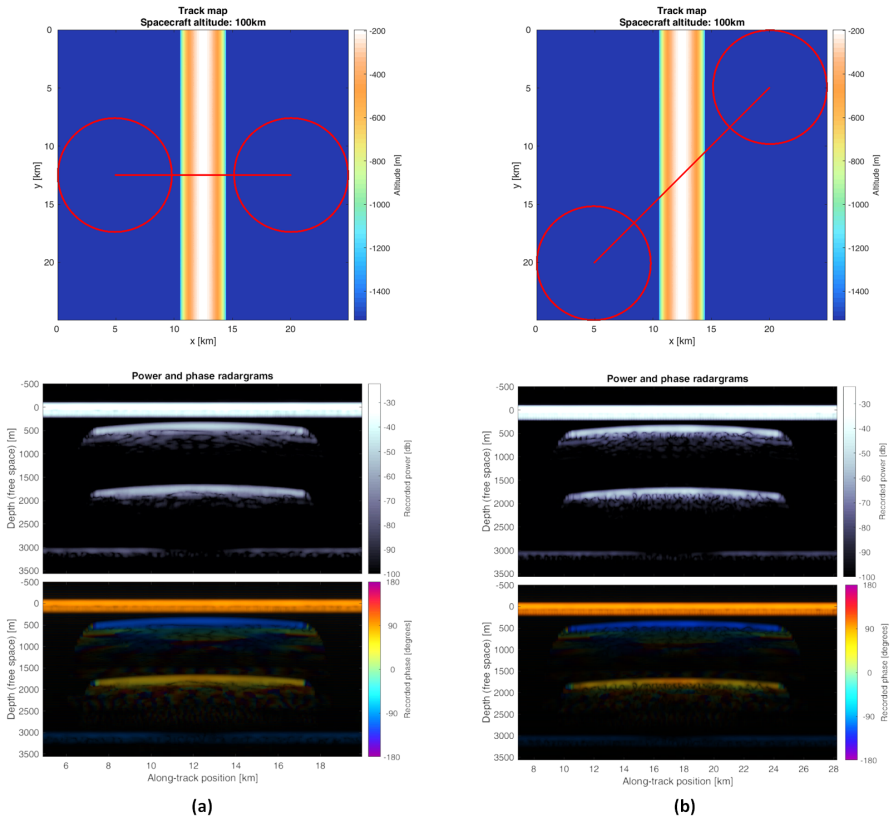

Figure 2.13: Electromagnetic signature of a lava tube of width $w = 4000$ m and roof height $h_r = 200$ as seen by the 10 MHz central frequency radar for (a) perpendicular and (b) oblique crossing. The phase radargrams highlights the phase inversion between the reflection of the roof and the bottom of the lava tube.

Our simulations highlight the very important feature of phase inversion, which can be observed in the radargrams of every detectable tube irrespective of the crossing direction (see Fig. 2.13 to Fig. 2.16). Indeed, the roof echo presents a 180° phase shift with respect to the surface echo. This is expected from a wave traveling from a medium 1 to a medium 2 characterized by $\epsilon_1 > \epsilon_2$ (i.e. roof medium to vacuum interface). To retrieve the subsurface phase component resulting from the interface reflection, the path-length phase contribution should be subtracted from the overall echo signal phase. In our simulations, we can perform this compensation in a deterministic way since we can exploit the a-priori information in the digital elevation model. In practice, phase inversion resulting from the interface reflection can be separated from the phase change due to path-length difference in a similar fashion as it is performed in ground penetrating radar (GPR) phase-based techniques for ground profiling [55, 56, 57, 58]. Radar sounder illuminates wider surface areas with respect to GPR, therefore the surface topography phase contribution shall be taken into account when compensating for the path length. Fortunately, high resolution DEM of the Moon are available, thus both clutter returns detection [59] and subsequent

topography phase contribution correction can be performed if needed.
Another important issue is the phase noise induced by the galatic noise. To address this issue, we performed Monte Carlo simulations (about 5000 trials for each step of SNR) by injecting random gaussian noise into the signal and computing the absolute phase error induced by the noise. The simulations of Fig. 2.14 show that with an SNR equal or greater than 10 dB the absolute phase error can be considered acceptable. As it will be presented in the next subsection, phase inversion is a key feature for the differentiation of legitimate lava tubes echoes from the ones generated by off-nadir surface clutter.

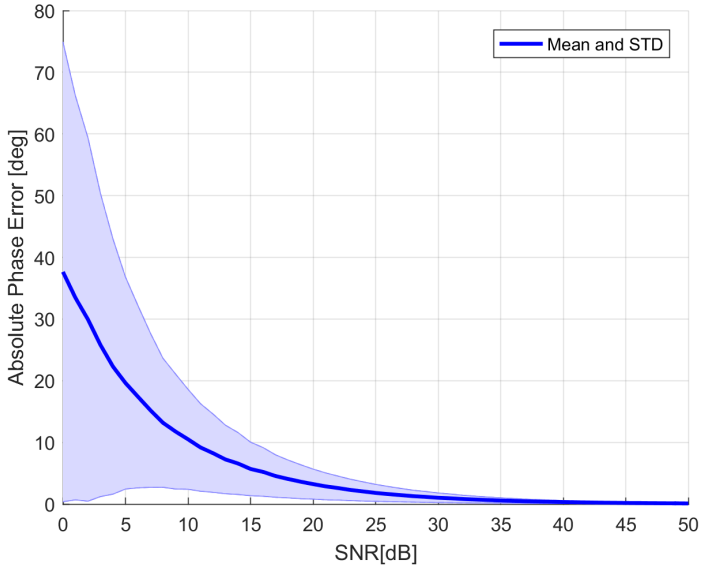

Figure 2.14: Mean and standard deviation of absolute phase error induced on the echo signal by galactic noise versus SNR.

The simulated electromagnetic signatures largely confirmed the conclusions of the performance analysis. Large lava tubes buried several hundreds of metres below the surface were only visible in the radargram with the 10 MHz carrier frequency instrument. On the other hand, the detection of shallow lava tubes was unambiguous only with the 100 MHz radar. On a few cases related to very shallow lava tubes, discrepancies appear between the simulation and the performance analysis. For instance, the upper hyperbola of the $w = 1250\,\text{m}$, $h_r = 50\,\text{m}$ lava tube cannot be distinguished from the surface response using the 10MHz radar. This is due to the fact that the range resolution computation does not take into account the elongation of the surface response over many range cells. Accordingly, the radar echoes originating from the roof of very shallow lava tubes may be buried in the surface echo. This depends on the lunar surface and radar antenna characteristics.

Tube Size	Width[m]	Height[m]	Roof Height [m]
Very Large	4000	1333	200
Large	3000	1000	20
Medium	1250	416	50
Small	500	167	5

Table 2.1: Dimensions of the four cases of lava tubes analysed in this study. Tube height is always equal to one-third of the tube diameter according to the stability analysis of [3]

2.4.2 Lava Tubes Electromagnetic Signatures : Impact of Lunar Topography

The simulations presented in the previous section were performed assuming a flat lunar surface. This allowed to characterize the radar electromagnetic signature of lava tubes in an ideal scenario. In this section, we analyse the effect of lunar topography on the lava tubes electromagnetic signatures. We consider three test scenarios namely (i) a reference case with no roughness, (ii) a case with a cratered surface and (iii) a case with a rough cratered surface and rough subsurface.

We performed the simulations of the above test scenarios considering a lava tube with width equal to $w = 2000\,\mathrm{m}$, and roof height equal to $h_r = 75\,\mathrm{m}$. The radar central frequency has been set equal to $f_0 = 80\,\mathrm{MHz}$ and the associated bandwidth equal to $B = 40\,\mathrm{MHz}$. Compared to the previous experiments, we selected a different central frequency in order to provide additional data.

In the lunar mare region, craters are the surface features which are mainly responsible for subsurface clutter. They are very likely to produce signatures composed of two vertically-aligned hyperbolas, which can be mistaken as lava tubes. The cratered surface simulation was run using a digital elevation model (DEM) including three craters of different sizes (see Fig. 2.17 (a)). On the one hand, the discrimination of crater signatures from the lava tube ones based on the power signature is very difficult due to the wide range of shapes craters and lava tubes can take. On the other hand, the signal phase information offers a very strong differentiating criterion. Experimental results show that, whereas hyperbolas of the crater signature display the same phase, those from a lava tube show a clear phase inversion on its upper hyperbola (see Fig. 2.17 (c)) allowing to discriminate between clutter and lava tubes echoes.

For the rough cratered surface and rough subsurface case, a fBm terrain with $H = 0.78$, $T = 20.6\,\mathrm{m}$, resulting in a RMS slope of $s(\Delta x) = 2.5°$ at $\Delta x = 17\,\mathrm{m}$, was superimposed to the DEM of the previous simulation. The fractal modelling of the surface is a reasonable representation of the lunar mare terrains [40], in which lava tubes have the highest probability of being found. A similar roughness has been applied to the lava tube roof and floor. Setting and results are shown in Fig. 2.18

In this simulation, we observe that the roof has an average peak power of -80 dB while the floor as an average power of -90 dB. These values are largely consistent with the findings of the performance analysis. The reference case yielded a peak power of about -75 dB for both the floor and the roof of the lava tube. The subsurface roughness as the effect of slightly distorting the lava tube signature with respect to the reference case. Nevertheless, the lava tube radar response can still be interpreted as two vertically-aligned

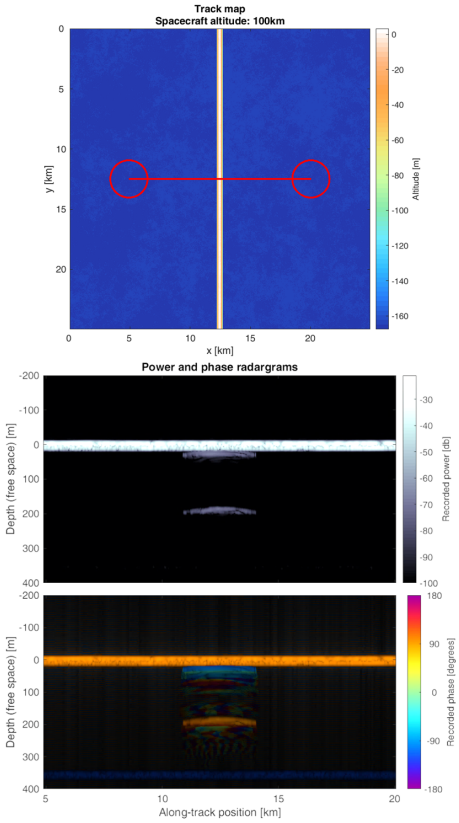

Figure 2.15: Electromagnetic signature of a lava tube of width $w = 500$ m and roof height $h_r = 5$ m as seen by the 100 MHz central frequency radar for perpendicular crossing. The phase radargrams highlights the phase inversion between the reflection of the roof and the bottom of the lava tube.

traces. More importantly, the surface roughness does not affect the phase information of the lava tube signals preserving the phase inversion mechanism. The response of the craters, although buried in the surface response, also indicates a negligible perturbation of the phase response.

The main conclusion from this analysis is that, even for surface presenting both roughness and clutter sources consistent with those typical of the lunar surface, the findings from the previous section still hold. The mechanism of phase inversion proved to be rather robust with respect to surface topography allowing to discriminate lava tubes from off-nadir surface clutter. In the case of clutter sources which are not located in the cross-track direction of the spacecraft, frequency analysis could also be used to discriminate between a nadir subsurface return (zero Doppler shift) and a an off-nadir clutter return (non-zero Doppler shift). Moreover clutter can be removed by performing clutter simulations as in [59] by taking advantage of the availability of the digital elevation model. Phase inversion, Doppler analysis and clutter simulations could thus be used in conjunction to further improve the reliability of lava tube detection.

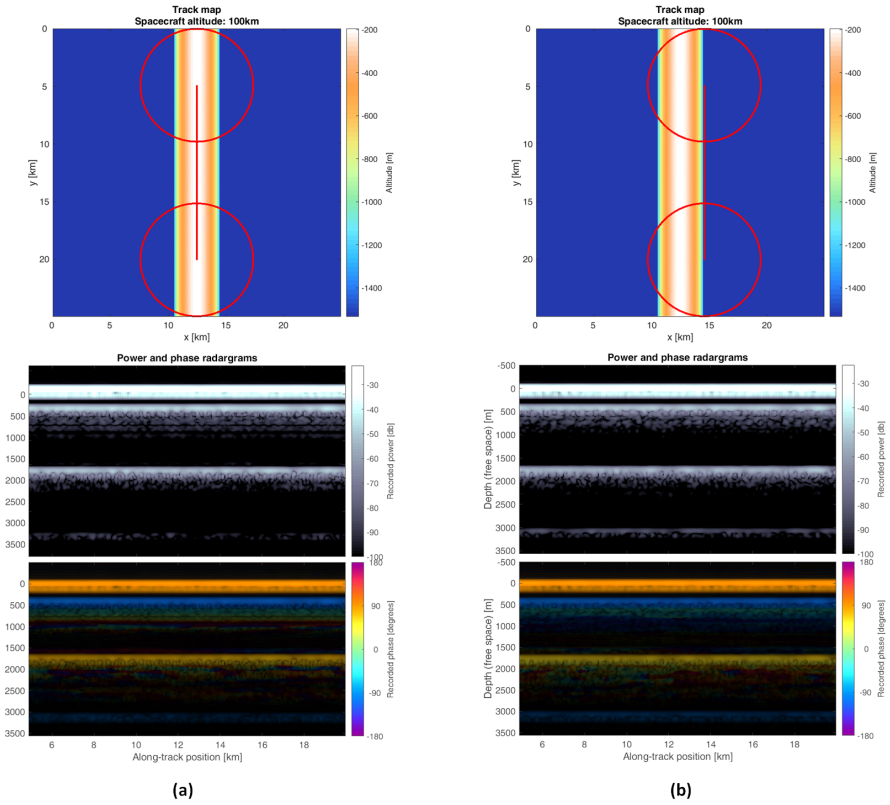

Figure 2.16: Electromagnetic signature of a lava tube of width $w = 4000$ m and roof height $h_r = 1333$ m as seen by the 10 MHz central frequency radar for (a) center parallel and (b) off-centre parallel crossing.

2.5 Discussion and Conclusions

Recent evidence based on gravity measurements and optical camera surveys suggest that there is a large number of lava tubes concealed under the Moon surface. In this thesis chapter, we investigated the feasibility of sounding lunar lava tubes of different dimensions from space with an instrument specifically dedicated for this task. By combining a theoretical performance analysis and comprehensive 3D electromagnetic simulations, we assessed the detectability of a wide range of lunar lava tubes.

The results show that a multi-frequency sounder in the MHz range is the best option to satisfactorily detect most of the lava tubes dimension which are expected from structural stability analysis recently presented in the literature. The main driving factors affecting the radar sounding performance are the attenuation of the basalt substrate (i.e. the value of the loss tangent) and its roughness (i.e. base of the regolith relief). The relief of the regolith/substrate interface is estimated to be in the order of meters. Our analysis shows that radar sounding at central frequencies between 80 MHz and 100 MHz can be considerably affected by it depending on the actual heights variation of the relief.

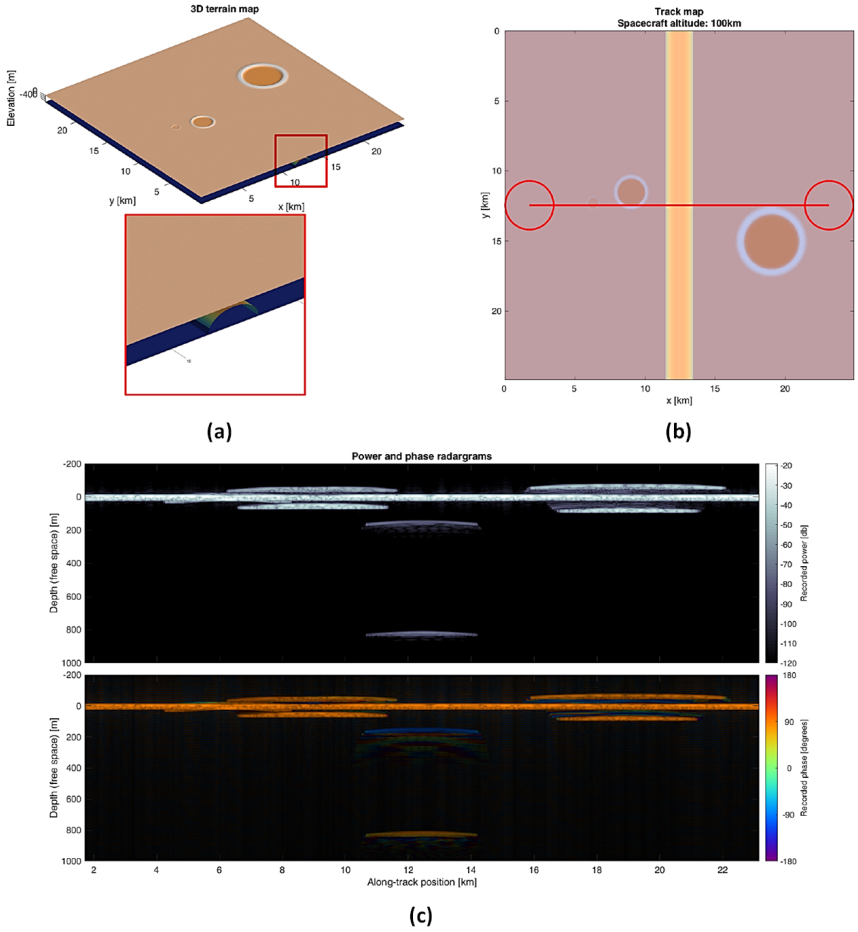

Figure 2.17: (a) Three-dimensional representation of the DEM used in this simulation (inset : zoom on the tube part). (b) Ground track of the probe (red line) along with two examples of footprint, the initial one and the final one (red circles), superimposed on the relevant features of the DEM. (c) Simulated radargram.

In this frequency range, sounding of lava tubes in the Moon highlands regions appears very unlikely whereas it is feasible in the the Maria region. Accordingly, a possible choice of the ranges of the two central frequencies which allow to sound the majority of lava tube dimensions is between 10 and 15 MHz for large lava tubes and between 60 and 65 MHz for small lava tubes sounding taking into account the 50% fractional bandwidth assumption. Regarding the technological readiness level of the proposed system, the fractional bandwidth of 50% can represent a surmountable challenge for the matching network design especially for frequencies in the lower range. The assumption on radiated power is based on the Lunar Radar Sounder transmitted power. The duty cycle in the LRS case is about 0.4%. The very low duty cycle was dictated by the 25% efficiency of the amplifiers. Please note that this configuration does not reflect the current state of the art in HF amplifiers. LRS has been developed more than 10 years ago. Modern amplifiers can reach 50% effi-

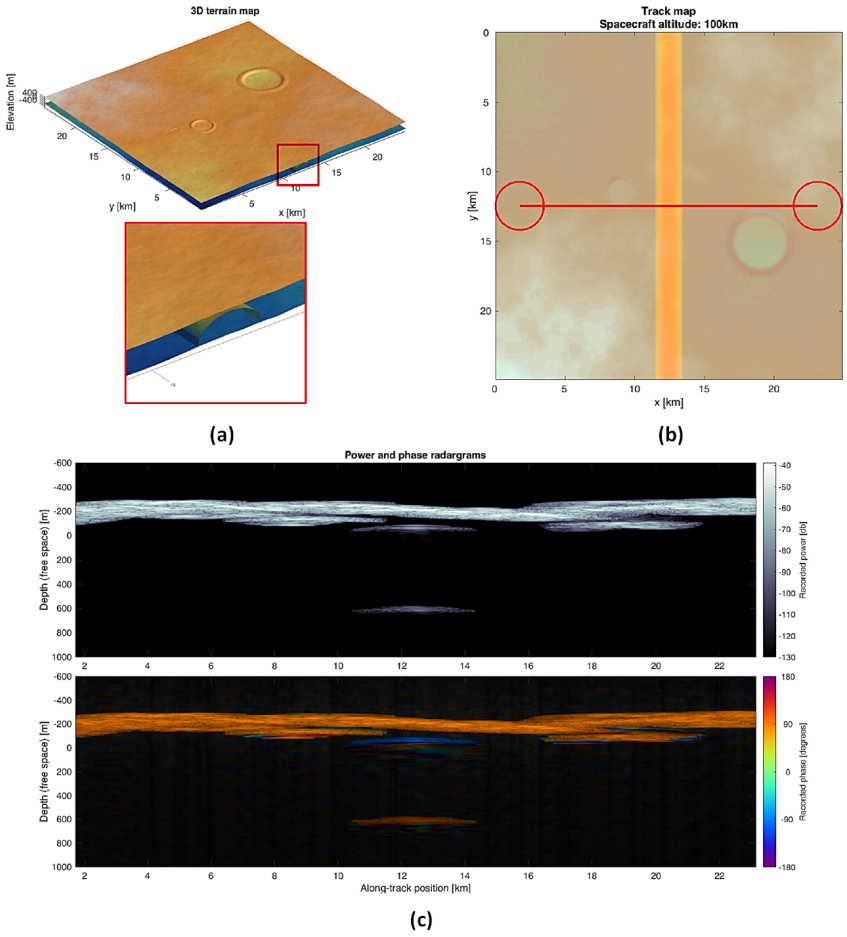

Figure 2.18: (a) Three-dimensional representation of the DEM used in this simulation (inset : zoom on the tube part). (b) ground track of the probe (red line) along with two examples of footprint, the initial one and the final one (red circles), superimposed on the relevant features of the DEM. (c) Simulated radargram.

ciency. In our case, the duty cycle is 5%, which is a reasonable and technological feasible value nowadays.

We simulated ideal radar signatures by analysing four lava tubes with representative dimensions. The simulations were performed at two different radar central frequency namely 10 MHz and 63 MHz.

Experimental results show that lava tube signatures (i.e., radar echoes) are composed of two vertically-aligned ensembles hyperbolas, one for the lava tube roof and one for its floor, each made of one bright hyperbola overhanging some more chaotic, dimmer returns. The radar echo from the lava tube roof shows a phase shift of 180° with respect to both the surface and the lava tube floor returns. This constitutes a very strong criterion to differentiate lava tube echoes from clutter (which do not show such phase inversion). The lava tube echoes structure and phase inversion mechanism hold even in the presence of

surface roughness such as that characterizing the lunar mare region of the moon. This is an important result as lunar mares are the main candidate regions for the subsurface presence of lava tubes.

As a final consideration, this study suffer from a certain number of limitations. The theoretical calculation of the range resolution estimation neglects the surface response that elongates over many different range bins depending on the surface characteristics an the actual radar antenna pattern. This could cause an overestimation of the detectability of the shallowest tubes. This effect has been detected in the simulations where lava tubes with sizes on the edge of detectability in the performance analysis could not be distinguished from the surface echo. The simulator itself has a limitation as well regarding whether or not the actual lunar surface topography is considered. As a coherent-only algorithm, it is forced to neglect any electromagnetic interaction at scales smaller to that of the DEM used, which in this case has a resolution of 118 m. This may have limited the amount of diffuse scattering in the simulated radargrams.

Chapter 3

A Bat Inspired Model for Clutter Detection in Radar Sounder Systems

As stated in the introductory part of this thesis, acquired data by radar sounders are often affected by unwanted artifacts which hinder the data interpretation conducted by geophysicists. Bats possess a remarkable ability in discriminating between a prey, such as a quick-moving insect, and unwanted clutter (e.g. foliage) by effectively employing their bio-sonar perfected in million years of evolution. Striking analogies occur between the characteristics of bats sonar and the one of a radar sounder. In this chapter[1]*, we propose an adaptation of the unique bat clutter discrimination capability to radar sounding by devising a novel clutter detection model. The proposed bio-inspired strategy proves its effectiveness on Mars experimental data and paves the way for a new generation of sounders which eases the data interpretation by planetary scientists.*

3.1 Introduction

Radar sounders are spacebourne sensors which exploit the interaction between electromagnetic waves and matter to probe the subsurface of celestial bodies. Bats are unique animals whose million years evolution has resulted in the refinement of a bio-sonar which is fundamental for hunting preys. Their bio-sonar performances are still unmatched by human-made radar and sonar systems.
These two apparently different fields of science sharing ties with electromagnetism for planetary exploration and biology offer inspiration to open up new ways of dealing with ambiguities in radar geophysical exploration of planetary bodies. As stated in Chapter 1.2.1, in a single given acquisition, planetary sounders antennas (which are assumed to be dipoles due to mechanical reasons) are always pointed toward nadir direction with respect to the surface and illuminate large surface and subsurface regions. The very large antenna footprint implies that off-nadir surface reflections (i.e. surface clutter) of the transmitted signal can be disguised for echoes coming from the interior of the target area. This causes

[1]Part of this chapter appears in:
L. Carrer and L. Bruzzone, "Solving for Ambiguities in Radar Geophysical Exploration of Planetary Bodies by Mimicking Bats Echolocation," in *Nature Communications*, 8.1 (2017): 2248

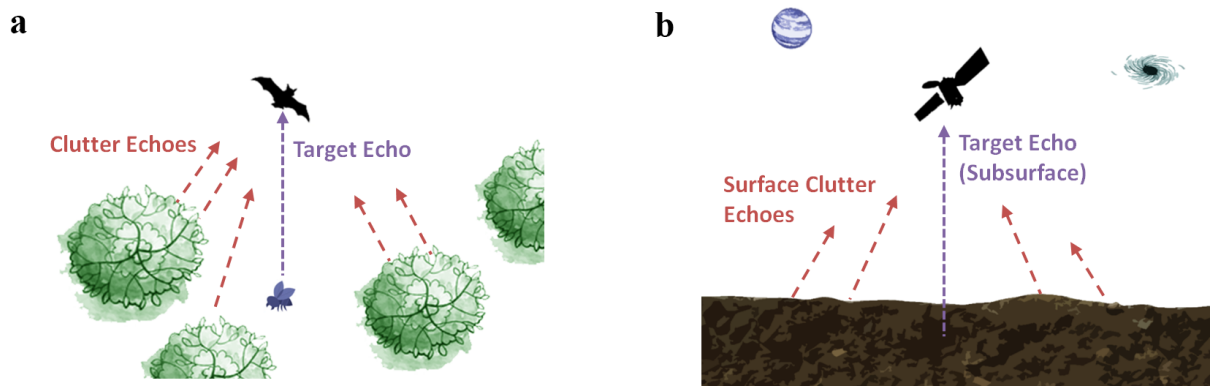

Figure 3.1: Similarity between (**a**) bats and (**b**) radar sounders acquisition geometry. In the bat case, side clutter echoes are coming from foliage while in the radar sounder case are coming from surface features. For both cases, the target of interested is always located in nadir direction.

a serious issue in terms of data interpretation. The clutter main driving factors are the surface characteristics such as roughness and electromagnetic backscattering properties. The most popular approach to clutter identification is to simulate the ambiguous echo signals produced by the surface and then compare them with the experimental data [60]. This approach requires the availability of a digital elevation model of the surface, which should be acquired by other instruments (e.g. a laser altimeter), with a sufficient resolution to give accurate results. Unfortunately, very often a surface digital elevation model is not available or it has an insufficient resolution with respect to the radar wavelength. Different attempts have been made to find a distinctive domain (i.e. an electromagnetic property of the signal) where disambiguation between clutter and subsurface signal can be performed. Recent papers proposed to detect clutter by focusing on the antenna pattern[61], the polarization[62] and interferometric diversity [63]. The approach based on antenna pattern diversity consists in deploying two different antennas. The primary antenna points towards nadir direction, whereas the secondary antenna illuminates surface regions to the sides of the main one. The signal received by the secondary antenna is assumed to contain only off-nadir surface clutter and therefore it is subtracted from the signal acquired by the primary antenna thus achieving clutter reduction. Polarization can be exploited for solving clutter ambiguities by transmitting circularly polarized waves. Nadir and subsurface reflections invert the sense of polarization once, whereas the off-nadir clutter reflections result in a double bounce. By projecting the received signal onto a suitable feature space, it is in principle feasible to distinguish the off-nadir reflections from the subsurface ones. The interferometric strategy consists in measuring the phase difference between the echoes received by two spatially separated antennas. The expected phase distribution for the nadir subsurface echoes differs from the one of the clutter thus making discrimination possible. However, none of the aforementioned strategies has proven to be the final solution to this specific problem. Moreover, the methods based on polarization and interferometry have never been tested on actual experimental data acquired from space.

Different animal species, such as dolphins and bats, rely on echolocation for foraging and navigation[64]. Their bio-sonars characteristics and processing scheme share many similarities with the strategies being adopted in radar sounders design and operations. As an example, some bat species transmit linear frequency modulated signals [65] and adapt the time between each signal transmission according to the target distance [66]. When hunting preys, bats usually fly in complex environments such as canopies of forests. This suggests that their sonar system should be capable of dealing with unwanted echoes coming from the surroundings [67, 68, 69]. Moreover, big brown bats need to face a given prey with their mouth. This implies that their targets will always be oriented toward nadir direction. It is therefore clear that a radar sounder and a big brown bat share a similar acquisition geometry (Fig. 3.1) even if in very different scenarios. Bates et al. [67] made a major step forward in unveiling the processing scheme of big brown bats (*Eptesicus Fuscus*) that is associated with their remarkable clutter mitigation performance. The main concept behind the *Eptesicus Fuscus* clutter reduction technique is to exploit frequency diversity. Big brown bats modulate two different harmonics over the same linear frequency modulated signal. The pattern beam-width (i.e. spatial distribution of the transmitted energy) is frequency dependent and narrower for the higher harmonic with respect to the fundamental one. Moreover, the signal attenuation due to atmospheric effects is frequency dependent too. By performing the ratio of the echo power between the two harmonics big brown bats can predict the echo direction of arrival and range. In the present study, we successfully adapt and implement the *Eptesicus Fuscus* clutter mitigation mechanism to radar geophysical exploration of planetary bodies. We develop a clutter detection model inspired by the bats processing strategy and tailored to the specific case of radar subsurface sounding. This results in a model that provides simple physical conditions for which clutter ambiguities can be resolved. We then apply the proposed bio-inspired model to experimental data acquired over different regions of Mars to assess the effectiveness of the presented approach.

3.2 Proposed Clutter Detection Method

3.2.1 Physical Analogies Between Bats Bio-Sonar and Radar Sounding

We analyze the *Eptesicus Fuscus* clutter mitigation strategy to find and study the difference and analogies with radar sounding. We argue that it is possible to adapt the bat clutter mitigation technique to the radar sounding case. The main obvious difference is that bats emit ultrasound waves while radars electromagnetic (EM) waves. Nevertheless, the two domains share many similarities such as interference, diffraction and refraction phenomena. A clear analogy, which is very relevant for this work, is the one between the bats sonar equation and the sounder radar equation. With reference to the big brown bat, the sonar equation that relates the echo power received (denoted as $P_{b,n}$) as function of the off-nadir angle θ and n-th harmonic $f_n,\ n = 1, 2$, is as follows [70]:

$$P_{b,n}(\theta) = \frac{P_{call}\ G_{tr}(\theta, f_n)\ A_{ear}\ \sigma_b^0(\theta, f_n) A_t\ e^{-2\alpha_b(f_n)d}}{(4\pi)^2 d^4} \tag{3.1}$$

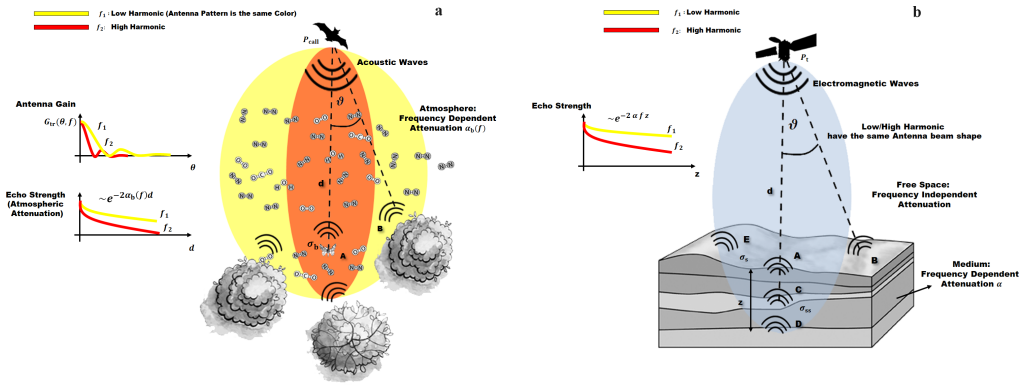

Figure 3.2: **(a)** Visualization of bats acquisition geometry assuming multi-harmonic signal transmission. The bats exploits a combination of atmospheric attenuation and antenna pattern diversity to distinguish clutter echoes coming from foliage. **(b)** Acquisition geometry for radar sounders assuming multi-harmonic transmission. The echo strength reduction in the subsurface depends on the transmitted frequency.

where P_{call} is the power of the sonar call transmitted by the bat, d is the target (e.g. insect) distance from the bat and $G_{tr}(\theta, f_n)$ is the gain of the transmitting antenna. It depends on the shape of the bats nose or mouth. A_{ear} is the area of the receiving antenna (i.e. bat's ear) and $\sigma_b^0(\theta, f_n)$ is the acoustic cross-section of the target. It indicates the target (e.g. a moth) capability of reflecting the transmitted energy back to the bat per unit area. This quantity depends on factors such as the shape and material of the target. A_t is the target area, a large target reflects more energy back to the bat. Finally, $\alpha_b(f_n)$ is the atmospheric attenuation constant which greatly affects the amount of echo power received by the bat and sensibly increases with frequency [71]. The relevant parameters of the above equation are sketched in Fig. 3.2 (a).
The bats multi-harmonic scheme is reflected by modeling in the radar equation the transmission being performed at two different harmonics namely f_1 and f_2. Both harmonics modulate the same chirp signal (i.e. linear frequency modulated) with equal bandwidth and pulse-width. This is consistent with the bats transmission scheme presented in Bates et al. [67]. From the radar system point of view, a higher central frequency would allow to exploit a larger bandwidth when compared to a lower one. Therefore, in order to have similar bandwidths at both harmonics, the higher harmonics bandwidth shall be selected to be less or equal the maximum allowable fractional bandwidth of the lower one. The echo power received from the surface at a given off-nadir angle θ and at the n-th harmonic ($n = 1, 2$) harmonic f_n is given by the radar equation [17] and it is equal to:

$$P_{s,n}(\theta) = \frac{P_t \; G(\theta, f_n) \; A_e \; \sigma_s^0(\theta, f_n) A_{ill}}{(4\pi)^2 d^4} \tag{3.2}$$

where P_t is the radar transmitted power, $G(\theta, f_n)$ is the antenna gain, $A_e = G(\theta, f_n)c^2/(4\pi f_n^2)$ is the antenna aperture where c is the speed of the light, $\sigma_s^0(\theta, f_n)$ is the surface backscattering coefficient, A_{ill} is the illuminated area and d is the distance between the radar

antenna and an arbitrary point of the surface. The surface backscattering coefficient measures the ability of a given surface to reflect electromagnetic energy. The forementioned quantities are visually described in Fig. 3.2 (b). By comparing equation (3.1) and equation (3.2) it is clear that the resulting echo power in the two cases depends on similar quantities. The main difference is that in the radar case there is no exponential attenuation of the echo power due to the atmospheric effect as in the bat case. This is expected because in planetary radar sounder the medium between the radar antenna and the surface is assumed to be vacuum. In practice, several celestial bodies such as the Earth do possess an atmosphere. To this extent, the ionosphere is a particularly important region with regards to radio signal propagation and radio communications in general [72]. Its properties govern the ways in which radar signals, particularly in the HF/VHF bands, propagate and distorts. The main degrading effects of ionosphere interaction with the radar signal are echoes resolution and peak power losses. An additional delay is also induced to the radar echo. These effects can be compensated by using radar processing techniques [73] for ionosphere distortion compensation. As stated in the introduction, the main goal of a radar sounder is to investigate the subsurface rather than the surface. In this case, the echo power at the n-th harmonic is described by:

$$P_{ss,n}(\theta) = \frac{P_t\ G(\theta, f_n)\ A_e\ \sigma^0_{ss}(\theta, f_n)\ A_{ill}}{(4\pi)^2(d+z)^4}(1-\Gamma^2_{01}(0))^2 e^{-2\ f_n\ \alpha\ z} \tag{3.3}$$

where α is the subsurface two-way attenuation factor (see (1.12)), z is the depth into the ground, Γ_{01} is the Fresnel reflection coefficient between the first medium and the second one (see (1.22)), $\sigma^0_{ss}(\theta, f_n)$ is the subsurface back-scattering coefficient and z is the ground penetration depth. The subsurface attenuation is function of the ground material electrical conductivity and relative permittivity. By analyzing the expression of the subsurface echo power presented in (3.3), we notice that there is a similarity between the atmospheric attenuation term in the bat case and the subsurface attenuation in the radar case. This represents a further relevant analogy which plays an important role in the definition of the bio-inspired ambiguities detection model described in the next section.

3.2.2 Bio-inspired Ambiguities Detection

Big brown bats adopt a combination of path attenuation difference and antenna pattern diversity [67] to distinguish foliage clutter. We can better understand the bat processing by analyzing the ratio of the echo power received at the two different harmonics [see equation (3.1)], which is equal to:

$$\Delta P_b(\theta, d) = \frac{P_{b,1}(\theta, d)}{P_{b,2}(\theta, d)} = \frac{G_{tr}(\theta, f_1)\ \sigma^0_b(\theta, f_1)}{G_{tr}(\theta, f_2)\ \sigma^0_b(\theta, f_2)}\ e^{-2(\alpha_b(f_1)-\alpha_b(f_2))d} \tag{3.4}$$

This power ratio is only function of the frequency dependent parameters such as attenuation and sonar cross-section of the target. This remarkable property implies that computing the echoes power ratio between different harmonics is a simple clutter discrimination strategy because it discards many physical parameters affecting the echoes

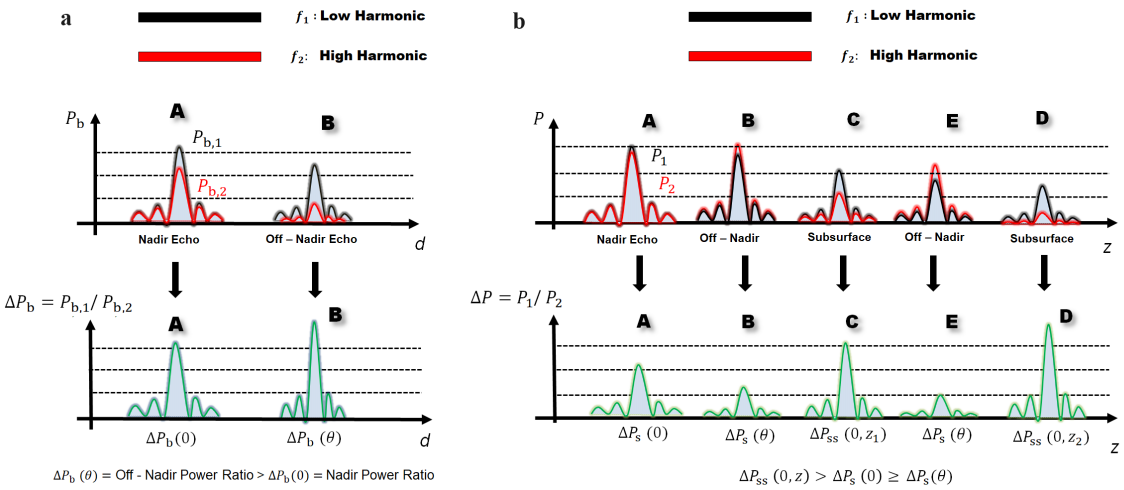

Figure 3.3: Visual Examples on how bats and radar sounders are able to disambiguate clutter on the power return at different harmonics. **(a)** For the bat case, $P_{b,1}$ and $P_{b,2}$ are the echo power received as a function of the distance at the two different harmonics. Points A and B are referred to Fig. 3.2 (a). **(b)** For the radar sounder case, P_1 and P_2 are the echo power received as a function of the distance at the two different harmonics. Points A to E are referred to Figure 3.2 (b).

intensity such as the power of the sonar call. It is interesting to note that the power ratio $\Delta P_b(\theta, d)$ defines a polar plot as function of the distance d and the angle θ. Except for the antenna gain, the other parameters such as attenuation are physical quantities not under the control of the bat. By analyzing the experimental results of Bates et al.[67] we can infer that echolocation evolution [74, 75] shaped the bat's antenna gain at different harmonics to result in a functional and wise representation of the power ratio $\Delta P_b(\theta, d)$. Accordingly, it has very different values for nadir direction (i.e. target position) with respect to off-nadir direction. A potential ambiguous return can be identified by simply comparing the power ratios [Fig. 3.3 (a)] of the different received echoes and verifying if the power ratio of a potential echo coming from nadir direction is greater than the one of an echo originated from a different angular direction such that:

$$\Delta P_b(0, d_1) < \Delta P_b(\theta, d_2) \tag{3.5}$$

where d_1 represents the distance between the bat and the target and d_2 the distance between the bat and the ambiguous return (e.g. foliage). Please note that in this paper by convention the power ratio definition is reversed if compared to the experimental results of Bates et al.[67].
In planetary radar sounders, the antenna type (i.e. dipole) excludes the possibility of having two antenna patterns with very different beam-widths. According to this, we assume that $G^2(\theta, f_1) \simeq G^2(\theta, f_2)$. On the other hand, the radar sounder signal experiences a greater attenuation in the nadir direction with respect to a bat signal due to the presence

of the subsurface. It is important to note that both antennas are pointed toward nadir direction. Following the bat clutter mitigation strategy, we define the surface echo power ratio $\Delta P_s(\theta)$ as follows:

$$\Delta P_s(\theta) = \frac{P_{s,1}(\theta)}{P_{s,2}(\theta)} = \frac{f_2^2\ \sigma_s^0(\theta, f_1)}{f_1^2\ \sigma_s^0(\theta, f_2)} \tag{3.6}$$

The subsurface echo power ratio $P_{ss}(\theta, z)$ is equal to:

$$\Delta P_{ss}(\theta, z) = \frac{P_{ss,1}(\theta, z)}{P_{ss,2}(\theta, z)} = \frac{f_2^2\ \sigma_{ss}^0(\theta, f_1)}{f_1^2\ \sigma_{ss}^0(\theta, f_2)}\ e^{-2(f_1 - f_2)\alpha z} \tag{3.7}$$

The result of equation (3.7) is similar to the surface echo power ratio of equation (3.6) but it has an additional dependence on the subsurface attenuation. The exponential scaling factor is always positive since we consider that $f_1 < f_2$.
Being the surface and subsurface natural terrains, we describe the backscattering coefficients assuming a fractal model [76, 77]. We derive the surface and subsurface echo power ratio for the nadir-looking case (i.e. $\theta = 0$) which are respectively equal to:

$$\Delta P_s(0) = (\frac{f_2}{f_1})^{2/H_s} \tag{3.8}$$

$$\Delta P_{ss}(0, z) = (\frac{f_2}{f_1})^{2/H_{ss}} e^{-2(f_1 - f_2)\alpha z} \tag{3.9}$$

where H_s and H_{ss} are the Hurst exponents of the surface and subsurface respectively. The value of the Hurst exponent is related to the terrain roughness. If the following condition is verified, then the subsurface echo signal can be always discriminated from clutter:

$$\Delta P_{ss}(0, z) > \Delta P_s(0) \geq \Delta P_s(\theta) \tag{3.10}$$

This inequality is inferred from the big brown bat clutter cancellation scheme previously described with the obvious addition of the subsurface return. An illustration describing how ambiguity can be resolved in the radar sounding case is shown in Fig. 3.3 (b). In order to apply the disambiguation condition, it is useful to locate the surface echo return. In general, this can be easily done for each echo trace as it is the return with the highest intensity[78]. The reader can notice that when compared to the bat case of equation (3.5), the condition is inverted. In the radar case, an higher attenuation difference among the two harmonics in the nadir direction is useful for improving clutter detection. In the bat case, the validity of the disambiguation condition of equation (3.5) has been experimentally verified. In the case of the radar sounder, to verify the limits of validity of the above disambiguation condition, first we need to analyze the inequality $\Delta P_{ss}(0, z) > \Delta P_s(0)$. This is equal to:

$$\frac{f_2 - f_1}{\ln(f_2/f_1)} > \frac{H_{ss} - H_s}{H_{ss} H_s} \frac{1}{\alpha z} \tag{3.11}$$

Equation (3.11) allows the selection of radar sounder harmonics in terms of (i) surface/subsurface geometrical parameters (i.e. H_s and H_{ss}), (ii) dielectric properties of the subsurface (i.e., α), and (iii) penetration depth z. If we consider fixed the aforementioned listed parameters, then the model performance in detecting ambiguities increases as the two harmonics separation increases. This is because the difference in power ratio of the subsurface with respect to the surface is equal to:

$$\Delta P_{ss}(0,z)/\Delta P_s(0) = (f_2/f_1)^{2c_h} e^{2\alpha(f_2-f_1)z} \tag{3.12}$$

where $c_h = (H_s - H_{ss})/H_{ss}H_s$. Equation (3.12) provides an indication of the model sensitivity.
The dielectric properties of the subsurface play an important role in ambiguity detection performance. High subsurface attenuation scenarios resulting in larger values of α provide better clutter disambiguation performance both in terms of sensitivity (i.e. $\Delta P_{ss}(0,z)/\Delta P_s(0)$) and minimum penetration depth (see equation (3.11)) when compared to low attenuation ones. The hypothesis that the surface echo power ratio from nadir direction is greater than the one from off-nadir direction (i.e. $\Delta P_s(0) \geq \Delta P_s(\theta)$) can be proven according to physical considerations. If we assume $f_2 > f_1$ in a confined range of frequencies typical of an orbital radar sounder, then it is always true that the power ratio $\Delta P_s(\theta)/\Delta P_s(0)$ will diminish for an increasing off-nadir angle θ. This is because the lower harmonic f_1 always perceives a smoother surface compared to f_2. This results in a stronger backscattering at f_1 for small off-nadir angles when compared to f_2. On the other hand, the backscattered power at f_1 decays faster than the return at f_2 as the off-nadir angle increases. Thus the result is a reduction of the ratio $\Delta P_s(\theta)/\Delta P_s(0)$ as θ increases. This hypothesis is supported by considering the frequency dependent root mean square slope $s(f_2, f_1)$ of a given surface defined as follows [54]

$$s(f_2, f_1) = s_0 \, (\frac{f_2}{f_1})^p \quad 0 \leq p \leq 1, \quad f_2 > f_1 \tag{3.13}$$

where the reference slope is denoted as s_0. It is clear from equation (3.13) that surface roughness increases as f_2 increases for a fixed f_1. Being the slope an indicator of a given surface roughness, this proves our hypothesis that $\Delta P_s(0) \geq \Delta P_s(\theta)$. Large facets of sloping terrains are among the main contributors to clutter echoes which could be typically mistaken as subsurface reflections. The value of θ of the surface and subsurface backscattering function is affected by the local slope of this type of features. This phenomenon could improve or degrade the disambiguation performance depending on the actual value of the feature surface slope and thus is strictly scenario dependent. In general, the value of θ in the nadir region should be smaller than the one in the off-nadir region. This is required to fully preserve the validity of the disambiguation condition on clutter and is mathematically expressed as:

$$\cos^{-1}(\hat{d}_n \cdot \hat{n}_n) \leqslant \cos^{-1}(\hat{d}_o \cdot \hat{n}_o) \tag{3.14}$$

where $\hat{d}_n$ and $\hat{d}_o$ are the distance versors pointing from any generic nadir and off-nadir surface locations to the radar respectively (Fig. 3.4). Similarly, we denote as $\hat{n}_n$ and $\hat{n}_o$

the local surface normal to any given nadir and off-nadir surface point respectively, and as $(\cdot)$ the dot product. Indeed, the local value of the surface normal is directly connected to the value of the local surface slope. The experimental results presented in the following section show that the local surface slope does not have a major impact on the model performance and the condition of equation (3.14) is in the majority of cases verified.

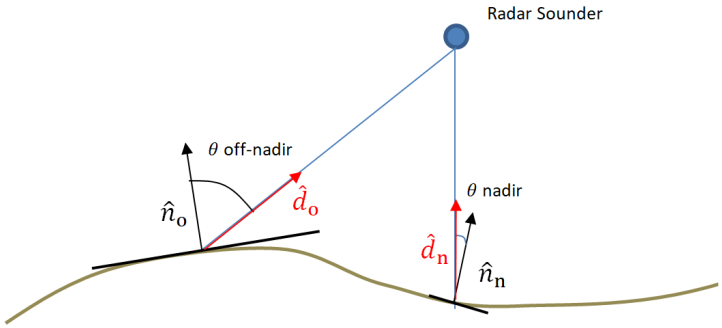

Figure 3.4: Geometry Scheme for the Local Surface Slope Analysis. The figure versor definitions is the following: $\hat{d}_n$ and $\hat{d}_n$ are the distance versors pointing from any generic nadir and off-nadir surface location to the radar respectively. Similarly, $\hat{n}_n$ and $\hat{n}_o$ are the local surface normal (i.e. the versor perpendicular to the local surface orientation) to any given nadir and off-nadir surface point respectively.

3.3 Experimental Results

We analyzed the effectiveness of the devised bio-inspired model to discriminate clutter features which can be disguised as subsurface structures by using real radar sounder data acquired over Mars. We verified the validity of the proposed model by analyzing radargrams under three different hypothesis: (a) clutter signal only (b) subsurface signal only and (c) mixed case where both clutter and subsurface signals are present. In order to test the proposed model for different surface and subsurface conditions, we selected three regions of Mars namely the South Polar (SP), the Deuteronilus Mensae (DM) and the Amazonis Quadrangle (AQ). The SP and DM regions are icy regions [10, 79]. The AQ is a volcanic region and its subsurface is mainly composed by dry sediments[80]. The subsurface only and clutter only hypotheses have been tested on all the datasets. The mixed case hypothesis has been validated on the AQ and DM datasets, as the SP dataset did not provide sufficient statistical data for the mixed case. This because in the SP region the subsurface structures are in locations where the surface topography is relatively smooth and does not generate clutter.

3.3.1 Data Overview and Pre Processing

The experiments for the different datasets were performed on the Shallow Radar (SHARAD)[81] Reduced Data Records (RDR). The SHARAD RDR records consist of radar received echoes that have undergone basic radar processing. They are correlated with the auxiliary information needed to locate the observation in space and time and compensated for the ionosphere effect [73, 82] resulting from the interaction between the radar signal and the martian ionosphere plasma[83]. Among the available datasets from planetary sounder instruments, the SHARAD ones are the only that allows to have both a reasonable harmonic separation and the same acquisition geometry which is required by the proposed model.
Being SHARAD a single frequency channel system, the two harmonics and the associated bandwidths were retrieved by dividing the radar bandwidth into two non-overlapping sub-bands [84] (Fig. 3.5). Accordingly, we obtained two linear frequency modulated signals of bandwidth 5 MHz centered at $f_1 = 17.5$ MHz and $f_2 = 22.5$ MHz, respectively. The

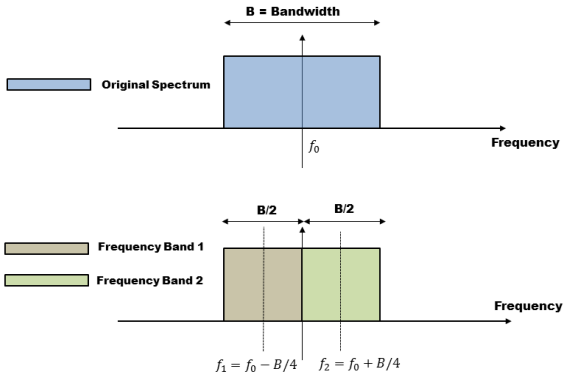

Figure 3.5: Working Principle of dividing the radar bandwidth into two sub-bandwidths

data has been processed according to the following procedure for denoising and validation purposes.
Let us define as $R(x, y)$ the SHARAD full-bandwidth radargram (see Fig. 3.6). Each value of this bidimensional function represents an echo intensity. The Cartesian coordinate x denotes depth while the y coordinate denotes the position of the sensor along the orbit trace. As a result of dividing the signal bandwidth into two sub-bandwidths, we obtain the "low-frequency" radargram denoted as $R_L(x, y)$ and the "high-frequency" radargram denoted as $R_H(x, y)$. For each sub-bandwidth we apply a 128 points moving average in the y direction and a 5 points moving average in the x direction. This is needed for increasing the signal to noise ratio. Then we compute the statistical noise power for each echo trace. In radar sounding noise samples are always available within each given range line leading or trailing the actual surface and subsurface signal. We exploit this

property to compute the statistical mean of noise power for the lower sub-bandwidth namely $NPM_1(y)$. Then the threshold T is computed as:

$$T(y) = K \cdot NPM_1(y) \tag{3.15}$$

K is an arbitrary constant defining the threshold level which is experimentally set to 1.7 for all the dataset. The threshold is computed over the lower harmonic signal since it is expected to have a greater SNR especially for higher penetration depths with respects to the signal acquired at the higher harmonic. All the samples of each sub-bandwidth below the threshold are discarded from the processing. Then the power ratio $R_L(x, y)/R_H(x, y)$is performed only on the peaks of each echo trace which is averaged with its two neighboring samples in order to deal with sensor resolution uncertainty. The bi-dimensional power ratio is subsequently averaged with a 3 x 3 averaging filter. The surface return is located for each given y. Then the disambiguation condition is applied to each echo trace for all the processed samples after the surface return. Each feature (e.g. clutter or subsurface) is represented by many echo samples allowing to compute mean and standard deviation of the power ratio. Each sample is declared as clutter or no clutter and the final decision is taken by majority rule. For each analyzed radargram ambiguous and real subsurface returns were labeled for validation purposes by detecting them with a specific clutter echo simulator [85]. We defined an ambiguous return as a geological-like structure having a contiguous extent in both horizontal (i.e. along-track) and vertical (i.e. depth) direction. For each echo ambiguous return, the equivalent depth is estimated by considering the difference between the vertical value of its coordinates centroid and the estimated position of the surface echo. We limited the analysis to the first 1000 m of subsurface depth according to the nominal penetration capability of the SHARAD instrument.

3.3.2 Results on Clutter Only Hypothesis

In the clutter only hypothesis, we verified whether the surface echo power ratio [i.e. $\Delta P_s(0)$] is greater or equal than the off-nadir surface power ratio [i.e. $\Delta P_s(\theta)$] according to the the proposed bio-inspired model. The results are analyzed in terms of the clutter detection ratio which has been defined as the number of clutter feature correctly classified as clutter [i.e. $\Delta P_s(0) \geqslant \Delta P_s(\theta)$] over the total number of clutter features detected at each given depth. The experimental results for the three datasets (Fig. 3.7) show that the clutter detection ratio is satisfactory and nearly constant as a function of the clutter equivalent depth (i.e. the free space depth scaled by the expected value of the dielectric constant for the region under investigation). Moreover, the clutter detection ratio it is similar for the different Mars regions under consideration. The SP and AQ regions exhibit deeper clutter features than the DM region (Fig. 3.7) due to the higher roughness of the surface as confirmed by the Mars laser altimetry data[86]. Interestingly, the values and the behavior of ΔP_s versus the depth are similar among the different investigated regions (Fig. 3.8).

Fig. 3.9 shows an example of results obtained in the SP region for the clutter only hypothesis. The example illustrates how the disambiguation condition effectively discriminates the clutter generated by different craters which can be mistaken as subsurface

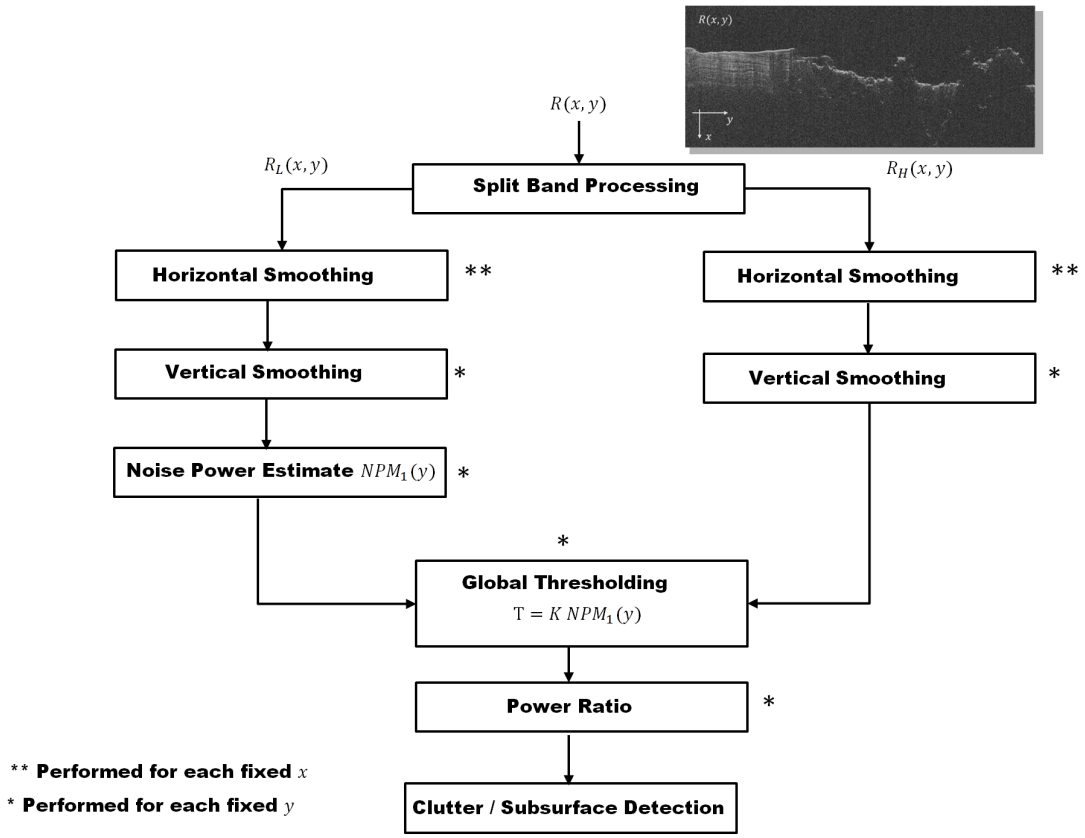

Figure 3.6: Processing Pipeline for denoising and evaluation purposes.

features. In this specific case, the value of $\Delta P_s(0)$ is equal to 3.1 dB. This value is in agreement with our model [equation (3.8))] for a surface having an Hurst exponent equal to $H_s = 0.7$, which corresponds to what is reported in the literature [87]. In the example, the values of $\Delta P_s(\theta)$ are provided as a function of depth. We analyzed the effects of the craters local slopes on the angle θ by computing the theoretical value of $\Delta P_s(\theta)$ and then comparing it with the experimental results shown in the example. The comparison (Fig. 3.10) shows that there is good agreement between the model and the surface power ratio values, and that the off-nadir reflections surface slope result in a larger θ when compared to the nadir surface reflection.

3.3.3 Results on Subsurface Signal Only Hypothesis

In the case of subsurface signal only, we verified the validity of left-hand side of the disambiguation condition [i.e. $\Delta P_{ss}(0, z) > \Delta P_s(0)$]. Similarly to the clutter only case, we defined the detection ratio as the number of subsurface features correctly classified as subsurface versus the total number of detected features at each given depth. In the

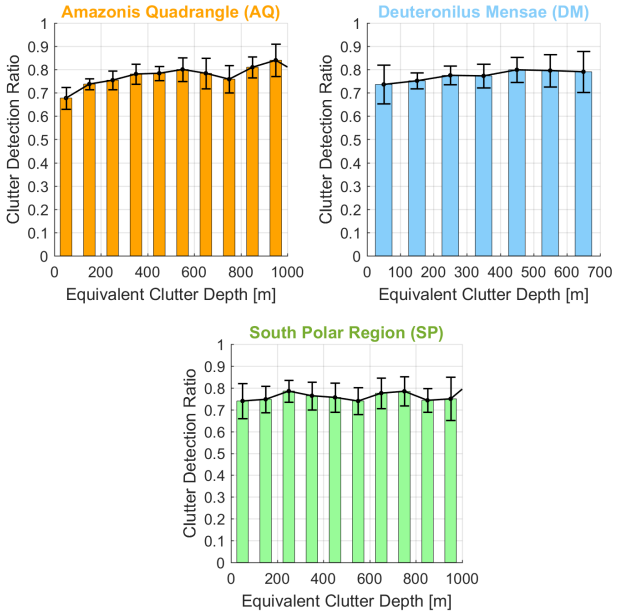

Figure 3.7: Clutter detection ratio, which is defined as the number of clutter feature correctly classified as clutter over the total number of clutter features detected at each given depth, and related mean absolute deviation vs the equivalent penetration depth for the different datasets. The maximum equivalent clutter depth depends on the surface roughness. The rougher the surface the higher the measured maximum equivalent clutter depth for a given dataset.

SP region, the subsurface stratigraphy allowed to compute the detection ratio from 50 to 750 m depth. Even though some subsurface structures are present from 750 m to 1000 m, the SNR for both harmonics was too low for performing meaningful analysis. The experimental results show that the subsurface detection ratio increases as a function of the equivalent subsurface depth and reaches values larger than 0.8 for depths greater than 400 m (Fig. 3.11). The explanation for this is that, for small depths, the attenuation difference between f_1 and f_2 is not sufficient to effectively discriminate the subsurface signal thus resulting in a small detection ratio. As the depth increases, the attenuation difference increases resulting in an improved detection ratio. This is line with what estimated by the proposed model [equation (3.12)], which predicts that for low depths the SP region represents a challenging case in terms of disambiguation performance since icy subsurface materials have low losses in the MHz range. For the DM data set, the measured average equivalent depth of the reflectors is equal to 450 m. The subsurface detection ratio is about 0.72. The average detection ratio for the AQ data set is of about 0.8 for subsurface features located at equivalent depths of 100 m. For the DM and AQ datasets, the clustering of subsurface features around a specific depth is in agreement with the geophysical analyses reported in the literature [80, 10]. The comparative analysis of the subsurface detection ratios (Fig. 3.11) confirms that in SHARAD data the subsurface

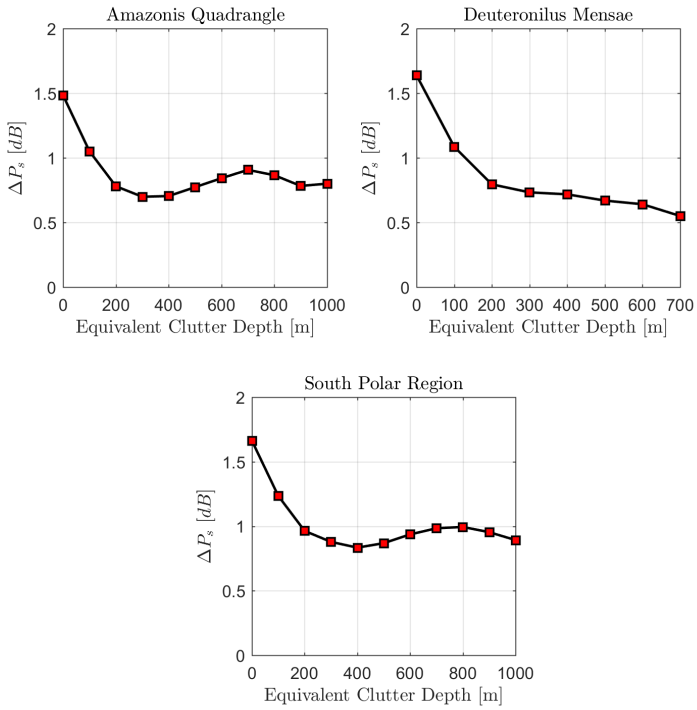

Figure 3.8: Mean values of the surface power ratio ΔP_s for the considered datasets. It is interesting to note that we obtain very similar curves for different datasets.

attenuation plays a major role in determining the performance of the method [equation (3.12)]. The AQ dataset provided solid disambiguation performance for low penetration depths when compared to the results of the SP region. This is expected being AQ a volcanic terrain with an higher two-way attenuation factor with respect to the other two subsets. The DM dataset results are in agreement with the ones of SP. This is also expected since the two regions shares very similar subsurface material properties. The comparison between the theoretical values of $\Delta P_{ss}(z)/\Delta P_s(0)$ of equation (3.12) and the experimental values of the subsurface power ratios for the various data sets shows that there is good agreement between the model and the expected geoelectrical properties of the subsurface (Fig. 3.12). For the AQ dataset, the model prediction is in agreement with the experimental data for values of tangent loss and dielectric constant consistent with those expected on a volcanic region [80]. Similar conclusions on model agreement can be done for the SP and the DM datasets using typical geolectrical values for these icy regions[10, 79].

3.3.4 Results on Mixed Case Hypothesis

In the mixed case hypothesis, we verified the validity of the combined disambiguation condition $\Delta P_{ss}(0, z) > \Delta P_s(0) \geq \Delta P_s(\theta)$. The experimental results show that the results

obtained for the other two hypothesis are generalized by the mixed case. For the DM dataset, the measured average power ratios are equal to $\Delta P_s(0) = 1.86 + /-0.53$ dB , $\Delta P_{ss}(0, z \sim 100m) = 3.72 + /-0.58$ dB and $\Delta P_s(\theta) = 0.59 + /-0.55$ dB thus confirming the validity of the disambiguation condition. For the AQ dataset, we measured average power ratios equal to $\Delta P_s(0) = 0.51 + /-0.42$ dB, $\Delta P_{ss}(0, z \sim 450m) = 2.24 + /-0.66$ dB and $\Delta P_s(\theta) = -0.34 + /-0.27$ dB, once again confirming the disambiguation condition validity. Fig. 3.13 shows an example of mixed case hypothesis result for the DM region. By applying the disambiguation condition, the subsurface feature located at about 550 m depth is correctly detected. The ambiguous reflections arising from different geological structures satisfy equation (3.10) and thus are correctly classified as clutter. The value of $\Delta P_s(0)$ is equal to 2.6 dB which, according to our model, corresponds to $H_s = 0.84$. Similarly to the previous discussed experiment, this value is in agreement with the literature. Another example of mixed case hypothesis result is provided in Fig. 3.14. This SHARAD radargram, acquired in the Phoenix [88] landing site region in the northern plains of Mars, has been already interpreted by Putzig et al.[89]. In their work, they highlighted the presence of a shallow subsurface layer [marked in Fig. 3.14 (a)] which can correspond to a relatively deep base of ground ice ($\epsilon = 3.15$) or to ice-free sediments (e.g. lava flows with $\epsilon = 8$). The presence of the mapped subsurface layer is accurately detected by the proposed method (Fig. 3.14 (c)) along with the discrimination of a clutter return located at about 300 m depth.

3.3.5 Considerations on Harmonics Separation

Despite the small harmonic ratio of the considered data (i.e. $f_2/f_1 = 1.29$) dictated by the lack of planetary radar sounder systems with larger harmonic ratios, the disambiguation condition provided satisfactory results for the different tested hypotheses, except for low depths in the SP dataset. Obviously, a small harmonic separation makes the model more prone to detection errors due to additive random noise and terrain back-scattered power variations. As stated, the proposed bio-inspired model predicts that the sensitivity and, in turns, the ambiguity solving accuracy increases by increasing the two harmonics separation. In practice, a trade-off exists between the maximum achievable harmonics separation and the frequency-dependent scattering properties of the target surface. If the harmonic separation is selected too large, then scattering properties of the surface may be not comparable at the two different frequencies (i.e. different scattering regimes). An example of the improvement in method sensitivity by varying the harmonic ratio f_2/f_1 is shown in Figures 3.15 and 3.16. The plots have been obtained considering typical Mars geoeletrical values [90, 91] and assuming $f_1 = 17.5$ MHz and f_2 variable.

3.4 Conclusions

Recent studies revealed how big brown bats can effectively discriminate between a given prey and unwanted clutter coming from their sonar scene background. In this study, we proved that this really powerful and relatively simple processing strategy can be mathematically modeled and adapted to radars for geophysical exploration of planetary bodies

thus improving the scientific interpretation of the acquired data. This has been achieved by observing and modeling many interesting parallelisms between the two apparently distant fields of biology and applied electromagnetism for planetary exploration. As a result, this work opens up for a new way of dealing with ambiguous returns in planetary subsurface probing radars without the need of having an additional sensor paired with it to produce a 3D surface model for correct data interpretation. The proposed bio-inspired model has been tested on real Mars experimental data and provided high detection rate (except for low penetration depths in the South Polar region case) despite the small harmonic separation dictated by limited existing data sets. The measured values of surface and subsurface power ratios are in good agreement with the proposed theoretical model. As expected, the model provides better clutter detection performance for high attenuation rates of the subsurface medium. The experimental results confirm that the fractal assumption on the back-scattering coefficient is effective in modeling complex scenarios such as reflections from crater rims and hills sides, which are the main features contributing to subsurface clutter. Moreover, the experimental results show that the change in the local surface slope induced by this type of features is well within the model theoretical assumption for the validity of the disambiguation condition. Beside the clutter and subsurface disambiguation capability, which is the core result of this paper, the proposed general approach can be useful to characterize the roughness of a given surface and subsurface terrain. This can be achieved by relating it to the change in surface and subsurface echo power ratio versus wavelength.

As a final remark, we point out that the proposed clutter detection model should be used to design radar sounder systems defined to have a sufficient large harmonic separation for optimizing performances. In the bat case, the harmonic ratio is equal to $f_2/f_1 = 2$ thus sensibly higher than in our performed experiments. This could possibly explain the greater clutter detection accuracy reported for bat tests when compared to our results. The average clutter detection ratio in the bat case is 0.95 which is 0.19 ± 0.01 higher than in our case.

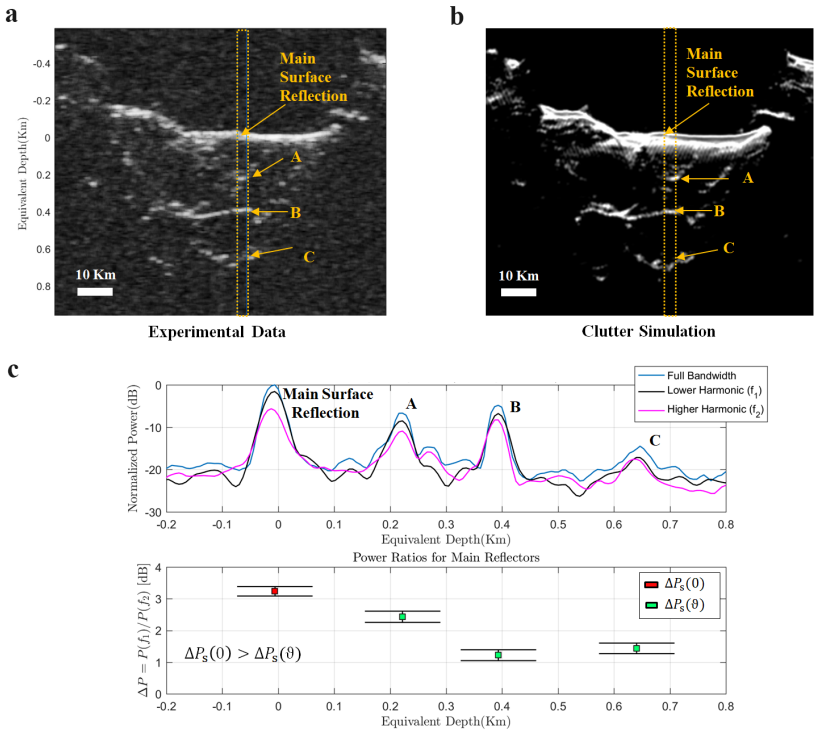

Figure 3.9: Example of the bio-inspired model results for a portion of the SHARAD radargram 0263001. The radargram is acquired over South Polar Region near Promethei Rupes and contains only clutter features that resemble subsurface echoes. The disambiguation condition on clutter $\Delta P_s(0) \geq \Delta P_s(\theta)$ is verified allowing the clutter discrimination to be effectively performed. **(a)** SHARAD radargram 0263001. The dashed orange box is the region under investigation. Main off-nadir clutter reflector regions are marked with letters from A to C **(b)** Clutter simulation confirming that the reflections are generated by surface features only. In this case, the clutter is generated by different craters walls. **(c)** Upper plot depicts echo traces (average over the investigated region) for the full signal and the harmonics decomposition. The lower plot shows the mean and standard deviation of power ratios for main reflectors. The number of echo traces considered for deriving the statistics is equal to 500. The equivalent depth in the subsurface medium has been computed from time delay assuming $\epsilon = 3.1$.

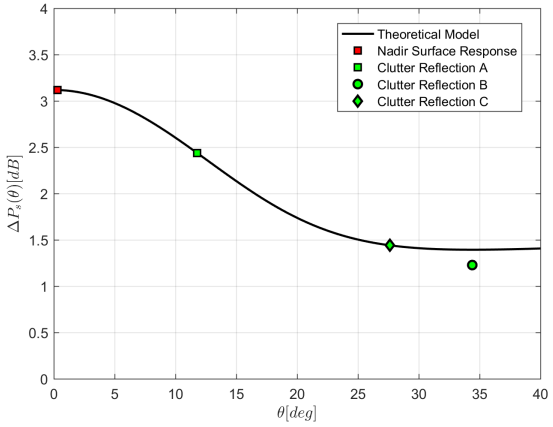

Figure 3.10: Model theoretical value versus the angle θ for $\Delta P_s(\theta)$ (black line) and comparison with the experimental data (average value). The model parameters for $\Delta P_s\theta)$ are $f_1 = 17.5$ MHz, $f_2 = 22.5$MHz and $H_s = 0.7$. The results show that the clutter returns of radargram 0263001 (Fig. 3.9), generated from different craters, correspond to large local slopes relative to the radar sounder. The clutter return of point C, compared to the one of point B, has a smaller local slope with respect to the radar even if it appears at a larger subsurface depth in the radargram. To disambiguate clutter it is sufficient that the nadir surface power ratio is greater than any other clutter reflection coming from off-nadir.

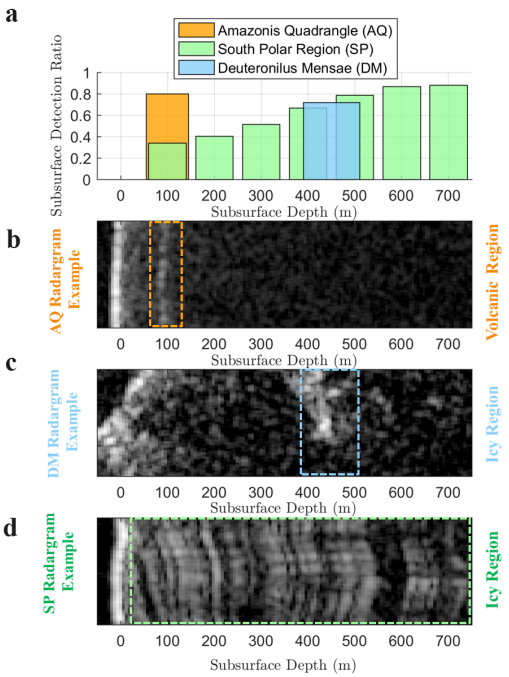

Figure 3.11: **(a)** Subsurface detection ratio, defined as the number of subsurface features correctly classified as subsurface versus the total number of detected features, at each given subsurface depth. The plot highlights the difference in subsurface detection ratio performance between a volcanic and an icy region due to the different subsurface attenuation values. **(b)** Typical radargram for the AQ region. The subsurface stratigraphy is such that the features are clustered around an average equivalent depths of 100 m. **(c)** Typical radargram for the DM region. The subsurface features are clustered around an average equivalent depth of 450 m. **(d)** Typical radargram for the SP region. The typical subsurface layering structure of this region allows the computation of statistics to be performed from 50 to 750 m depth.

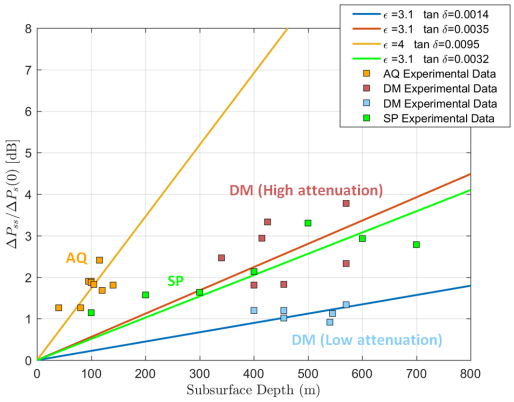

Figure 3.12: $\Delta P_{ss}/\Delta P_s(0)$ model predictions (see equation (3.12)) and comparison with the experimental results for the different datasets assuming $c_h \sim 0$. The disambiguation condition on subsurface signal predicts that $\Delta P_{ss}(z)/\Delta P_s(0) > 0$. For the AQ dataset we obtain subsurface power ratio values that are in agreement with the proposed model assuming a tangent loss of $9.5 \cdot 10^{-3}$ and $\epsilon = 4$ for the subsurface material. The DM dataset data is divided into two different classes, namely high attenuation and low attenuation. The experimental data are in agreement with the proposed model assuming an icy subsurface with $\tan\delta = 3.5{\cdot}10^{-3}$ for the high attenuation scenario and $\tan\delta = 1.4 \cdot 10^{-3}$ for the low attenuation scenario and $\epsilon = 3.1$ for both cases. For the SP region, the model predicts the experimental data assuming $\tan\delta = 3.2 \cdot 10^{-3}$ and $\epsilon = 3.1$. The DM and SP results are consistent with the fact that both regions have similar subsurface properties (i.e. icy regions).

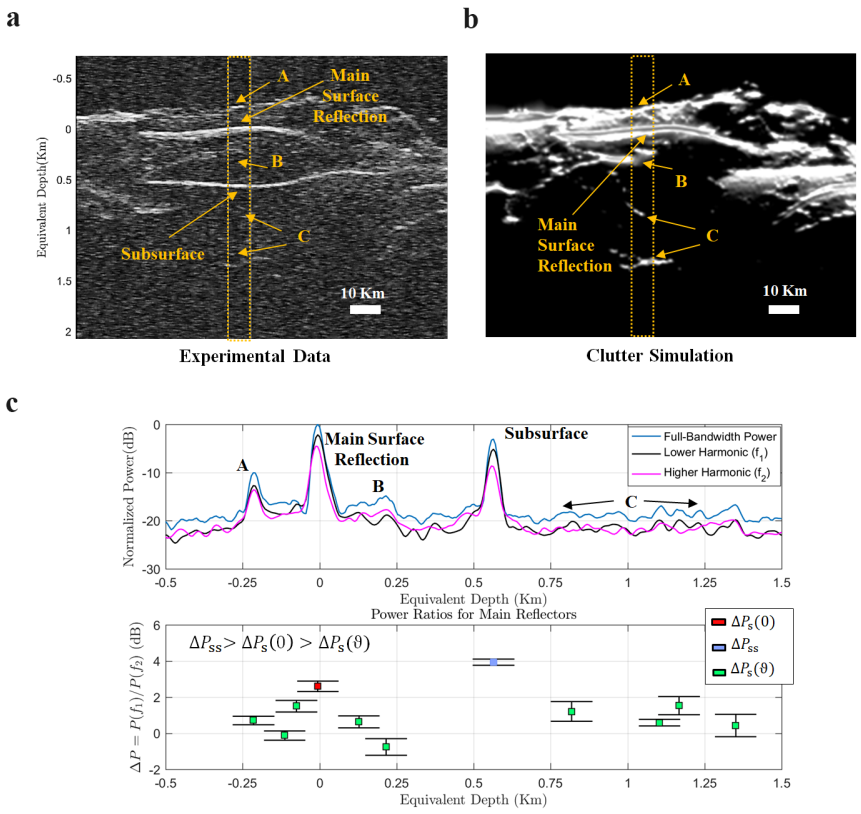

Figure 3.13: Example of the bio-inspired model results for a portion of the SHARAD radargram 0716902. The radargram is acquired over Deuteronilus Mensae and contains both clutter and subsurface features. The disambiguation condition $\Delta P_{ss}(0, z) > \Delta P_s(0) \geq \Delta P_s(\theta)$ is verified allowing the discrimination of clutter to be accurately performed **(a)** SHARAD radargram 0716902. The dashed orange box is the region under investigation. Off-nadir clutter reflections are marked with letters from A to C **(b)** Clutter simulation confirming that the reflections marked as A, B and C are generated by surface features only and that in the experimental data there is a legitimate subsurface reflection **(c)** Echo Traces (average over the investigated region) for the full and split bandwidth SHARAD signal (upper plot) and mean and standard deviation of power ratios for main reflectors (lower plot). The number of echo traces considered for deriving the statistics is equal to 700. The equivalent depth in the subsurface medium is computed from time delay assuming $\epsilon = 3.1$.

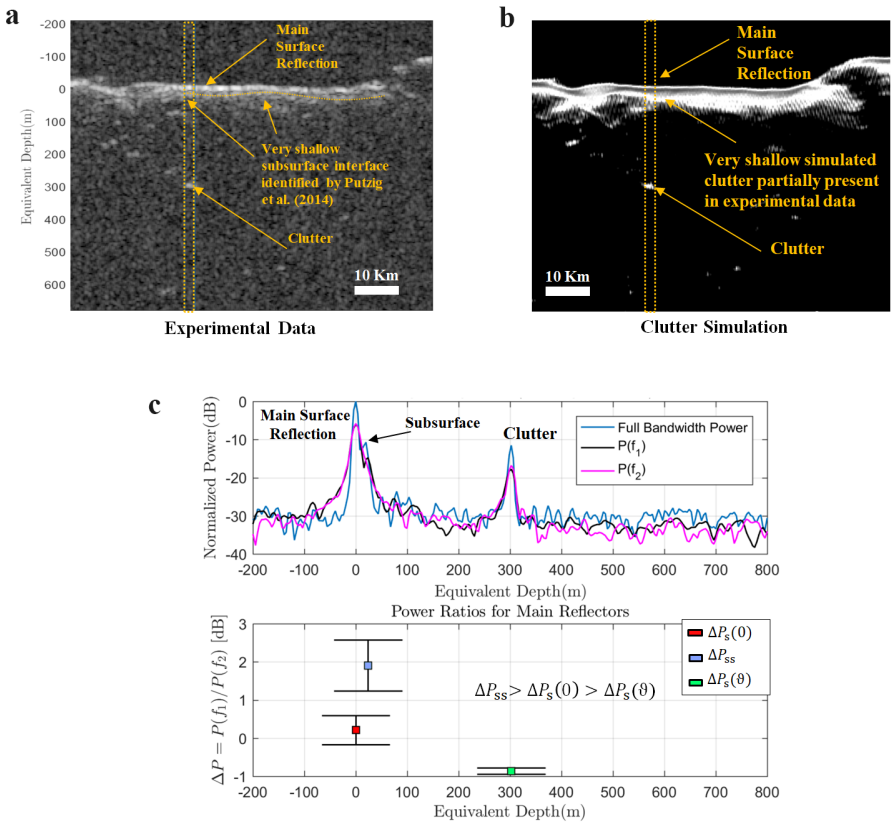

Figure 3.14: Example of the bio-inspired model results for a portion of the SHARAD radargram 1290301. This radargram has been previously analyzed by Putzig et al. [89] and it is acquired over the Green Valley of Vastitas Borealis and contains both clutter and subsurface features. The disambiguation condition $\Delta P_{ss}(0,z) > \Delta P_s(0) \geq \Delta P_s(\theta)$ is verified allowing the discrimination of clutter to be accurately performed and confirming the presence of a very shallow subsurface interface below the Phoenix landing site region. **(a)** SHARAD radargram 1290301. The dashed orange box is the region under investigation. The dashed orange line highlights a very shallow subsurface reflection mapped by Putzig et al. [89] using the same SHARAD observation **(b)** In this case, clutter simulation highlights a clear clutter reflection at about 300 m depths but overestimates clutter in the shallow subsurface **(c)** Echo Traces (average over the investigated region) for the full and split bandwidth SHARAD signal (upper plot) and mean and standard deviation of power ratios for main reflectors (lower plot). The number of echo traces considered for deriving the statistics is equal to 400. The equivalent depth in the subsurface medium is computed from time delay assuming $\epsilon = 8$.

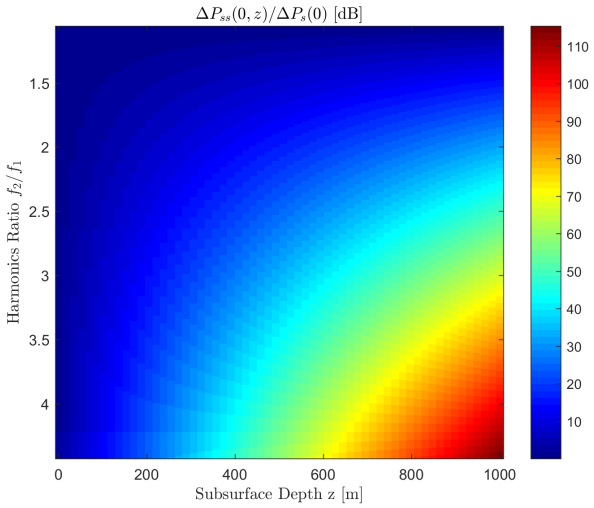

Figure 3.15: Values of $\Delta P_{ss}(0,z)/\Delta P_s(0)$ for a representative example of the Mars surface (e.g. Deuteronilus Mensae) assuming tangent loss equal to $tan\delta = 0.006$ and real part of the dielectric constant of the subsurface medium equal to $\epsilon_1 = 3.1$. From the figure, it is clear that the method sensitivity improves by increasing the harmonics ratios (i.e. f_2/f_1).

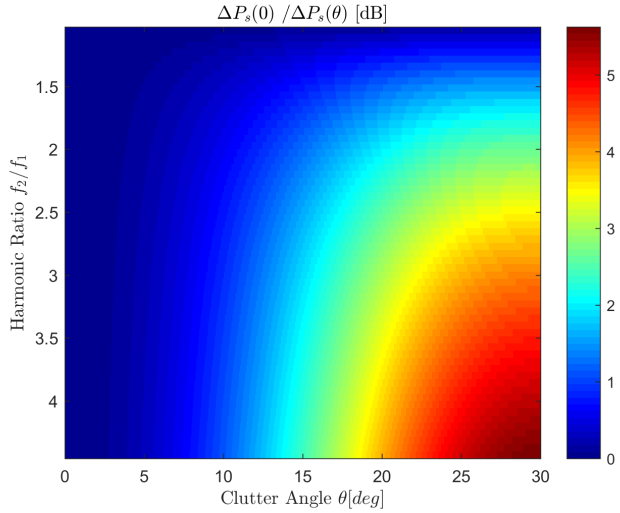

Figure 3.16: Value of $\Delta P_s(0)\ /\Delta P_s(\theta)$ for a representative example of the Mars surface(e.g. Deuteronilus Mensae). The plot has been computed assuming topothesy equal to $T = 10^{-4}$ m and Hurst exponent equal to $H_s = 0.85$. From the figure, it is clear that the method sensitivity improves for larger harmonics ratios (i.e. f_2/f_1).

Chapter 4

Automatic Enhancement and Detection of Layering in Radar Sounder Data Based on a Local Scale Hidden Markov Model and the Viterbi Algorithm

Radar sounders instruments produce a very large amount data. Very often these data are manually analyzed by planetary geophysicists. This is a very time-consuming operation and inherently subjective limits the scientific return of the data. In this context, automatic techniques can greatly support the planetary scientific community, ensuring reliable, consistent and fast extraction of information from the data. In this chapter [1], we propose a novel technique for the automatic detection of layer boundaries based on a local scale Hidden Markov Model (HMM), which model the radar response in the presence of a layer boundary, and the Viterbi Algorithm (which performs the inference step). The proposed technique is based on a divide and conquer strategy that executes the Viterbi algorithm using the observation data and the HMM to infer the most likely layer boundary location within a small radargram portion. Finally, a detection strategy is defined to chain together the inferred local layer locations. Furthermore, a novel radargram enhancement and denoising technique tailored to support the detection step is presented. The effectiveness of the proposed technique has been confirmed by testing it on different radargrams acquired by SHARAD (SHAllow RADar) over the North Pole of Mars. The results obtained point out the superiority of the proposed method in retrieving the position of each layer boundary (and thus of the related intensity and geometric properties) with respect to the state-of-the-art techniques.

[1] Part of this chapter appears in:
L. Carrer and L. Bruzzone, "Automatic Enhancement and Detection of Layering in Radar Sounder Data Based on a Local Scale Hidden Markov Model and the Viterbi Algorithm," in *IEEE Transactions on Geoscience and Remote Sensing*, 55.2, 2017, pp. 962-977.

4.1 Introduction

The large amount of data produced by planetary radar sounder instruments requires the development of automatic techniques for extracting relevant information from the acquired data in an efficient, objective and accurate way. However, the automatic extraction of information from radargrams produced by planetary sounders is a challenging task. This is due to (i) the very heterogeneous characteristics of the subsurface, (ii) the very long acquisitions distances both in the down-range and azimuth direction and (iii) the weak subsurface backscattered signal measured by the radar receiver resulting in a low signal to noise ratio. Planetary radargrams possess substantial differences when compared to other sounding instruments. In GPR (Ground Penetrating Radar), the number of subsurface layers is usually small and the azimuth and depth extension of the radargrams are small too. In ice sheets sounding of the Earth poles, the number of layers and the azimuth extension of the radargram is greater than in GPR and comparable to the planetary case. However, the SNR in ice sheets sounding is consistently higher than in the planetary case due to a higher radiated power and lower platform distance from the ground. It is clear from the above analysis that planetary radargrams have differences, when compared to other data products, which should be taken into account in the design of the data processing techniques. In this paper, we propose an automatic method for retrieving the spatial position and the radiometric properties of the subsurface layers in radargrams. The method do not rely on any specific geometric assumptions about the subsurface. Being the data acquired from planetary bodies inherently noisy, we adopt a statistical approach to the detection, which has the advantage of performing inference by explicitly modelling the spatial and radiometric uncertainty of the data induced by noise. In particular, we propose an approach based on a local scale Hidden Markov Model (HMM) and the Viterbi Algorithm (VA) for locating each of the target features. In this context, our approach addresses the critical issue of the literature algorithms which are characterized by a high computational complexity that scales with respect to both the state dimension and the number of targets. This issue is crucial in radargrams acquired by orbiting planetary sounders that are very large and usually contain a high number of layer boundaries in the subsurface. To avoid inconsistencies and false alarms in the detection procedure, we also propose a novel adaptive denoising and enhancement technique acting as a pre-processing step. This technique adaptively exploits the implicit information in the radargram signal samples to estimate the conditional density distributions of both noise and signal plus noise which are then used in the framework of the radar detection theory. The retrieved statistical information is combined with observations on the sensor deviations (e.g. accuracy) to produce a denoised radargram enhancing the subsurface layering with respect to noise and unwanted artefacts of the signal (e.g. side lobes). The denoising performances are determined statistically in terms of false alarm rate and detection probability.

This chapter is organized as follows. Section 4.1 introduces the background and the state-of-the-art along with the description of the sounder acquisition geometry and reference system. Section 4.2 presents the proposed pre-processing technique as well as the detection algorithm based on the local scale HMM and the VA. The experimental results obtained on SHARAD radargrams are presented in section 4.3, where they are also compared with those obtained by a recent state-of the-art-technique. Section 4.4 addresses

the conclusions of this chapter of the thesis.

State of The Art

In planetary radar sounders, the development of techniques for the identification and extraction of layers in radargrams is still at an early stage. The first attempt at detecting shallow linear features in SHARAD radargrams has been made by Freeman et al. [92]. The authors proposed a technique based on a combination of high-pass and low-pass filtering, matched filter and thresholding, under the assumption of having a flat (or quasi-flat) layering structure in order to apply the matched filter to highlight the horizontal features. The output of the method is a binary image showing the layering structure. However no information on the layer boundaries (e.g, geometric structure and radiometric characteristics) can be retrieved. In order to overcome these issues, Ferro et al. [93] proposed a method that exploits the BM3D [94] as a pre-processing denoising step and the Steger filter [95] for line detection. This method directly estimates the position of each layer with subpixel precision without relying on specific geometric assumptions. For each detected linear feature, it can retrieve the mean depth, the mean intensity and the relative mean contrast along with the layer distribution (i.e. number of features and density of layers) with a high overall accuracy. However, the method is designed for detecting mainly horizontal linear features in the radargrams, thus suffering the presence of local irregularities in the layering that would require more degrees of freedom in terms of feature detection. The method also leaves room for improvement in terms of false alarm and detection rate. In general, statistical models for multiple layer boundaries detection have been employed in related fields such as ground penetrating radar (GPR) and ice sheets sounding. In GPR, Smock et al. [96, 97] efficiently retrieved the layer boundaries using the VA by making an analogy between a radargram and a trellis. One of the main drawbacks of the VA is that it assumes that the most likely hidden sequence of states always starts from the first time step (i.e. first azimuth position). This assumption does not hold true for radargrams since a layer boundary could span only a small subset of the trellis. Smock proposed a solution to this problem by outlining a property of the VA named reciprocal pointer chains (RPC). This property consists in running the VA twice for each radargram. First, the algorithm runs from the foremost left to the foremost right azimuth position and then it starts from the foremost right to the foremost left position. If the left to right and right to left retrieved optimal states go exactly through the same path they form an RPC. Then an additional iterative step is performed for each layer boundary in order to refine the layer boundary position. It is important to note that in GPR the acquisition setup is very different from that of a planetary radar sounder. In Smock's setup, an antenna array is deployed in the across-track direction. This allows the acquisition of an entire radargram for each along-track position of the sensor. In turns, the performance of the VA can be improved from an acquisition to another by modifying the transition matrix of the algorithm at each along track position according to the results obtained from previous measurements. The RPC method runs the VA in a global fashion over the entire radargram. The pre-processing used by the authors is tailored specifically to the GPR case, where the spacing between layers is sensibly larger than in the sounder planetary case. Thus it is not straightforward to adapt the

method to be used with sounders data. In [98] the authors proposed a multi-target method that exploits the lateral continuity of the layer boundaries by first detecting and tracking for each radar scan the time of delay of backscattered pulses coming from the subsurface and then relating the neighbouring ones by assuming a first order Markov Model. To overcome the issue of limited performances of the above-mentioned technique when multiple targets have closely spaced delays, Nicoli et al. [99] proposed a method denoted as Multi-target VA that proved to have good performances for a very limited number of layer boundaries. Indeed, the algorithm complexity increases exponentially with the number of layers. In ice sheets sounding, Crandall et al. [100] proposed a method based on a statistical graphical model for finding layer boundaries under certain specific assumptions. The method models the radargram as a first-order Markov Random Field and then performs inference by applying the VA to each row of the radargram. Lee et al. [101] applied a probabilistic framework similar to the one in [100] but using a Markov-Chain Monte Carlo method rather than the VA to infer the position of the layer boundaries. These methods have been tested only on a limited number of layer boundaries (i.e. only surface and bedrock interfaces) and their computational complexity makes their application unfeasible to our problem. Regarding the number of detected layers, in ice sheets sounding most of the methods presented in the literature focus on the detection of the surface, the basal and the echo-free zone interfaces [102, 103, 104]. Recently, in ice sheets sounding several attempts have been made to extract the complete stratigraphy of the ice subsurface in an automatic or semi-automatic way [105, 106]. In this paper we focus only on automatic methods. Panton [107] proposed an automatic technique for tracing internal layers of a radargram, which is based on a combination of a high-pass filtering (denoising preprocessing step) adapted to process data having layers with different slope conditions. The actual tracing layer procedure is based on an active contour model (i.e. snakes). Before the tracing layer procedure takes place, the operator needs to manually specify the initial seeding points for initiating the integration procedure. The method is not effective in radargrams showing a missing or complex stratigraphy. Sime et al. [108] proposed a fast automated method for deriving dip angles of englacial radar reflectors. It exploits a preprocessing step based on incoherent averaging and thresholding. A local threshold is exploited for obtaining a binary image from the radargram on which short coherent layer segments are identified. Each coherent layer is selected and labeled on the basis of its logical values between adjacent image bins. Then the properties of the layer object such as position and angle are measured. As a final step the dip information is gathered together by location. Very recently, MacGregor et al. [109] proposed a method for automated radio stratigraphy of the Greenland Ice Sheet. The method is divided into three parts that trace and date reflections and normalize and grid age volume. The tracing reflection algorithm exploits the phase information contained in a coherent radar acquisition to derive the horizontal phase gradient of the englacial reflections and in turns the reflection morphology. The authors also propose an alternative method based on Doppler centroid for the same purpose. Then, by applying one of the two strategies, the radar data are integrated according to the information derived in the previous processing step. However, the above-described automatic methods are not suitable for planetary radar sounding applications due to the low SNR resulting in a highly disrupted structure

of the radargrams.

4.2 Proposed Automatic Enhancement and Detection Technique

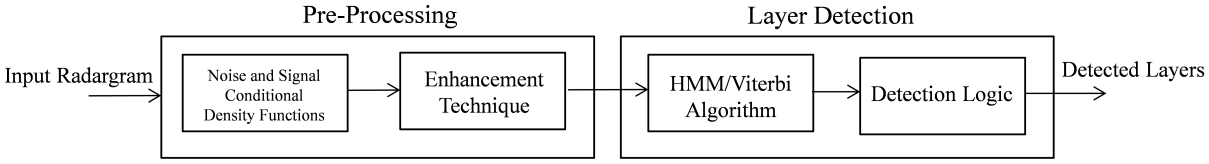

Figure 4.1: Block Diagram of the Proposed Technique. The layer detection block applies iteratively the VA and the detection logic stage to produce each layer.

The block diagram of the proposed automatic detection technique is depicted in Fig. 4.1. In the first processing step the noise and signal plus noise sample values conditional distributions are computed from the radargram. This allows one to perform an adaptive processing and filtering of the radargram by estimating the probabilities of false alarm and detection. The enhancement technique highlights the structure of the radargram by taking into account both the threshold derived from the previous step and the radar range accuracy. The enhanced radargram, which is the output of the pre-processing unit, is then given as an input to the layer detection module where the candidate features are identified by the combination of the HMM and the VA and validated according to a given strategy (i.e. detection logic). In this paper, the term detection has the meaning of finding the pixel coordinates of each layer boundary. An ensemble of pixel coordinates forms a vector which is representative of the position of the layer. The pixel coordinates can be converted to actual absolute distance values by knowing the parameters of the sensor and the orbit of the spacecraft. Moreover, the technique extracts the radiometric property of each layer (i.e. statistics of pixel intensity along the layer). This layer detection procedure can be exploited for further high level processing.

4.2.1 Proposed Radargram Pre-Processing Technique

This section presents a novel technique for enhancing the layering structure of the radargram that has several important properties. The technique is propaedeutic to the detection procedure which will be described in the next subsection. Le us define a given radargram as a 2D function $R(x, y)$ where each value of this function is a power sample of the radar returned signal. The Cartesian coordinate x represents the range direction while y is the along-track (i.e. azimuth) position of the sensor for a given acquisition. As a first step, an incoherent averaging of the radargram (i.e. moving average) is performed

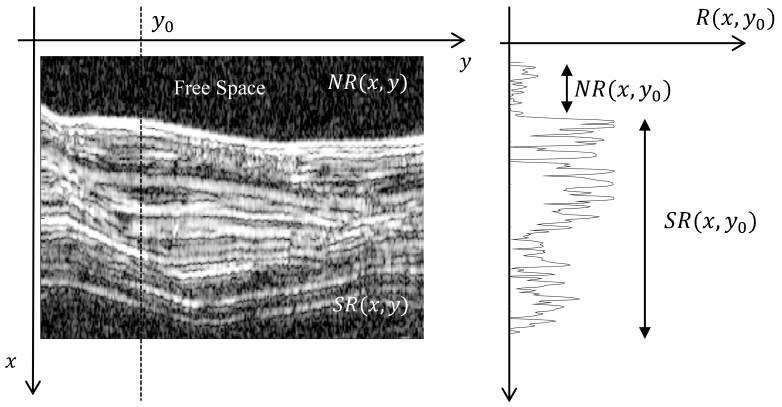

Figure 4.2: Radargram subdivision into noise region $NR(x, y)$ and signal plus noise region $SR(x, y)$.

in the azimuth direction according to the following equation:

$$R_{AV}(x,y) = \frac{1}{N_{AV}} \sum_{i=y}^{y-N_{AV}-1} R(x,y) \tag{4.1}$$

This allows preserving the signal and reducing the noise under the assumption that the layering structure is flat at a horizontal scale equal or greater than the averaging length N_{AV}. Note that this can be considered as a multi-look processing in the azimuth direction. After incoherent averaging the statistical properties of the radargram are analyzed. As the radar sounder receiver starts recording earlier than the actual surface and subsurface signals arrival times, for each pulse repetition interval (i.e. range line) the radar acquires a significant number of noise samples. It follows that for each radargram we can always define a region containing only noise and a region where the signal is superimposed to the noise. The existence of a signal free region is exploited to estimate adaptively the noise distribution. From such an estimate, it is possible to use the Neyman-Pearson decision strategy [110] to discriminate samples associated with signal from those only affected by noise. In such framework, a target is detected if:

$$p_s(\nu)/p_n(\nu) > T_h \tag{4.2}$$

where $p_s(\nu)$ and $p_n(\nu)$ are the signal plus noise and noise samples conditional density functions respectively, v is the generic echo sample intensity, and T_h a given threshold value. For each given radargram, the technique computes the above distributions in an empirical way according to the following procedure. Let $NR(x, y)$ be a sub-region of $R_{AV}(x, y)$ containing only noise pixels and $SR(x, y)$ be a sub-region containing the signal pixels that are superimposed over the noise ones (see Fig. 4.2). Under the reasonable assumption that thermal noise is independent from one range line to another, $p_n(\nu)$ is

estimated by extracting a significant amount of samples from $NR(x, y)$. The same procedure is used for computing $p_s(\nu)$ by using samples in $SR(x, y)$. For a fixed probability of false alarm (denoted as P_{FA}), the threshold T_h is computed by numerically inverting the following equation:

$$P_{FA} = \int_{T_h}^{+\infty} p_n(\nu) \tag{4.3}$$

$$P_D = \int_{T_h}^{+\infty} p_s(\nu) \tag{4.4}$$

The detection probability is useful for checking whether the technique is providing a sufficient detection rate for the selected probability of false alarm. For each range line (i.e. fixed azimuth position), the local maxima exceeding the threshold T_h are detected and retained as potentially associated with a layer whereas the other samples are set to zero. These local maxima are computed under the assumption that they must be separated by a number of samples greater than the range resolution. After this step, the radargram has the following representation:

$$R_p(x, y) = R_{AV}(x, y)\delta(x, y) \tag{4.5}$$

$$\delta(x, y) = \left\{ \begin{array}{cc} 1 & x = x_i,\ y = y_i \\ 0 & \text{elsewhere} \end{array} \right\} \tag{4.6}$$

where $\delta(x, y)$ is a binary mask and (x_i, y_i) is the position of the $i - th$ local maxima for which $R_{AV}(x, y) > T_h$, and $x_i - x_{i-i} > R_r$ where R_r is the range resolution. From the radar point of view, a layer boundary is a distributed target that, depending on its thickness, may persist for a certain number of contiguous range samples. The application of (4.5) has the effect of representing each layer boundary with a single pixel in the range direction thus removing its thickness information. This is needed in order to avoid multiple detection of the same layer in the actual layer detection procedure. Note that, the peak detected point range accuracy depends on the range accuracy ΔR_r. According to theory [111, 112], this quantity depends on the Signal to Noise Ratio after incoherent or coherent signal integration:

$$\Delta R_r = \frac{R_r}{\sqrt{SNR}} \tag{4.7}$$

For a given layer boundary, the peak detected sample sequence in the azimuth direction may have a discontinuous behaviour due to the measurement uncertainty described above. This is of course against the expected physical behaviour of the interface. The continuity of the boundary layer can be improved in the azimuth direction by performing the following convolution between $R_p(x, y)$ and the following window function denoted as $rect_{2\Upsilon}(x)$:

$$rect_{2\Upsilon}(x) = \left\{ \begin{array}{cc} 1 & x_i - \Upsilon \leq x \leq\ x_i + \Upsilon \\ 0 & \text{elsewhere} \end{array} \right\} \tag{4.8}$$

The length of the rectangular function $rect_{2\Upsilon}(x)$ in the range direction is computed taking into account the radar range accuracy ΔR_r and the range spatial sampling frequency f_r.

Its value Υ (i.e. half-width size of the function) is equal to:

$$\Upsilon = \lceil \frac{\Delta R_r}{2 f_r} \rceil \tag{4.9}$$

where $\lceil . \rceil$ is the ceil operator. According to this we model the uncertainty on the tracked point position by taking into account points in its neighbourhood in the range direction. The number of neighbouring points being considered depends of the range accuracy of the system. We can derive a lower bound for the validity of equation (4.9) by stating that, in order to avoid the overlapping of previously detected points induced by the rectangular function, the condition $\Delta R_r < R_r$ must be satisfied.It can be proven that this inequality holds true only if the SNR is greater than 0, which is in general easily satisfied by all the detected points. To further enhance the layer continuity a convolution with a gaussian low-pass filter of size $[2\Upsilon + 1, 2\Upsilon + 1]$ is performed. Replacing the actual radargram with its enhanced representation denoted as $\hat{R}(x, y)$ has two main advantages in terms of detection based on the VA. First, it avoids multiple tracking of the same layer. This may occur when a layer is particularly thick and can be interpreted by the VA as multiple adjacent paths. This problem has been observed in the application of K-best disjoint paths to GPR radargrams [97]. With our approach, once a layer has been tracked, it can be easily removed from the observation matrix since its thickness is predicted as equal to 2Υ. The second advantage of the proposed enhanced representation is to simplify the tracking of close layers by enhancing their separation. When two layers are very close, the VA could mistakenly interpret them as one layer. This issue is particularly evident when a weak layer is very close to a stronger one. In this case VA starts tracking the weaker layer but then it locks to the stronger one thus interpreting the two as a single entity. A false layer could also be caused by the summation of the side-lobes of the radar response of very close layers. On the other hand, with this approach the information on the layer boundary thickness is lost but can be retrieved after the layer boundaries tracking procedure. Note that the presented technique has a general validity and can be applied to any type of radargram for which a signal free region exists. In the case this region is not available, the method can be applied with the modification that the decision on the threshold value should be manually selected.

4.2.2 Combination of the HMM and the VA for Layer Boundaries Detection: Proposed Concept

This section presents the proposed layer boundaries detection method. In our approach, the layer boundaries within the radargram are detected by inference. For this particular task we take advantage of the VA [113]. The rationale behind the adoption the VA is that the enhanced radargram $\hat{R}(x, y)$, due to its sampled nature, can be modelled as a trellis of size $N_x \times N_y$where each pixel range position x is mapped into a specific state and each azimuth position y is mapped into a time step of the trellis graph. The function values of $\hat{R}(x, y)$ are pixel intensities corresponding to the echo signal power samples which are mapped according to a specific rule into an observation vector for each time step. By all means, in the context of HMMs, the VA allows to find the optimal state sequence

associated with a given observation sequence. However, as mentioned before, in planetary radargrams both the very dense as well as fragmented layer structure and the very long azimuth acquisition represent a challenge in terms of VA applicability. This results in a very high computational complexity and in possible incorrect results when the radargram is considered as a whole in the inference process. Thus to overcome these limitations, a divide and conquer approach is proposed to infer the position of layer boundaries. This strategy consists in applying an appropriate HMM to small blocks of the radargram, which locally models the radar response in the presence of a layer boundary, and the VA. This is done by selecting only a limited number of rows and columns for each computation. First, the seeding points needed for starting VA iterations are retrieved and stored for each azimuth position according to the local maxima detection procedure described in the previous section. Then, the algorithm sequentially scans each range line and initializes the VA by setting as initial state the seed under investigation. The seeding strategy addresses the issue of the VA regarding the layer boundaries spanning only a small portion of the radargram. The best path is computed by considering only a small subset of states (i.e. range extension of the block) surrounding the one of the seed. Starting from the position of the seed, the number of azimuth positions (i.e. time steps) spanned by the algorithm is assumed to be equal to an arbitrary minimum detectable line length. Then the method checks whether the best path computed for the given azimuth span can be identified as a layer boundary. This is done by verifying if the intensity of the pixels included in the best path are above or below a given threshold. If the computed block is considered to be a layer, the algorithm proceeds to analyse the following block by assuming as a starting point the last estimated state within the best path (thus the subset of states is centred on this point) from the previous computation and repeats the same procedure performed for the first block. The algorithm stops when the threshold condition on the current block is not verified or when it reaches the last possible azimuth position of the radargram. Thus the overall layer boundary is defined as the chaining of the best paths for each block. Once a layer has been tracked, it is removed from the enhanced radargram $\hat{R}$. Since it is expected that a layer generates a tracking seed for each azimuth position, once the layer position has been computed for its entire azimuth extension, the corresponding seeds are removed from the data. Then the entire process of finding the best path through the trellis for each layer starts again on a subsequent azimuth position only after all the seeds for the previous one have been explored according to the explained procedure.

4.2.3 Combination of the HMM and the VA for Layer Boundaries Detection: Proposed Algorithm

Let us formalize the description of the proposed technique. We first define the underlying HMM by adopting the notation presented in [114]. The main model parameters are:

- $L(\zeta)$: Total number of time steps.
- $2\Lambda + 1$: Number of hidden states in the model.
- $S = \{s_1, s_2, .., s_{2\Lambda+1}\}$: Set of states.
- $Q = \{q_1, q_2, .., q_{L(\zeta)}\}$: State sequence.

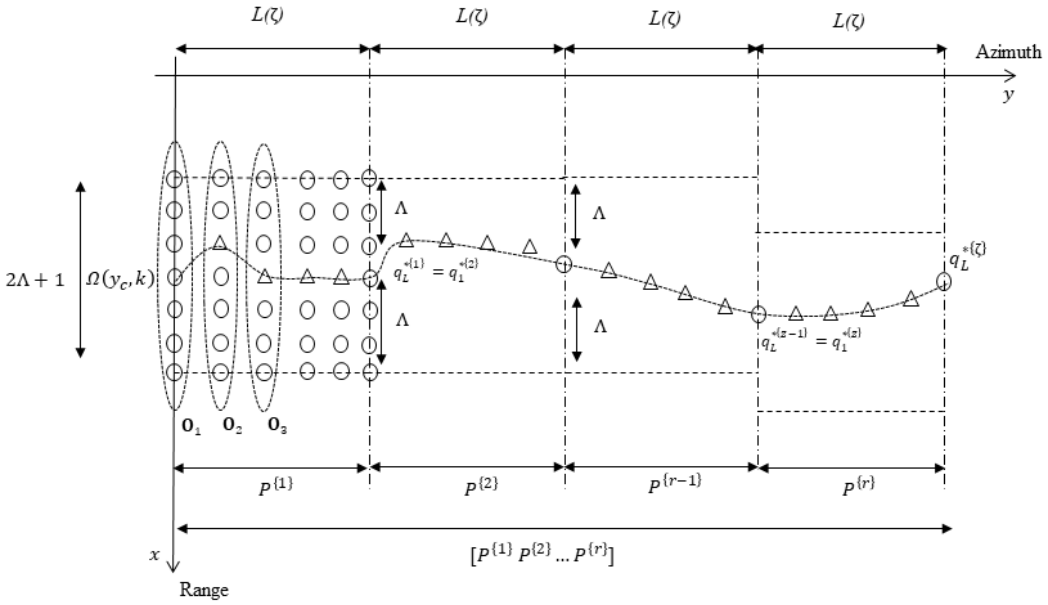

Figure 4.3: Illustration of the tracking procedure for a single layer boundary. Triangles represent an hypothetical retrieved best path states.

- q_t: State at time t. Where t locally corresponds (i.e. within the radargram sub-block) to the azimuth variable y.

- $\boldsymbol{O}_t$: Observation vector at time t.

The parameters Λ and $L(\zeta)$ are integer numbers that will be further discussed later throughout this section. In this context, the hidden states correspond to a layer being present at each of the range positions within the radargram sub-block under analysis. In other words, in the model there are $2\Lambda + 1$ hidden states and the $i - th$ hidden state corresponds to a layer which is positioned at a ground depth corresponding to the $i - t$h range pixel within the sub-block. The observation vector $\boldsymbol{O}_t$ contains pixel intensities extracted from the radargram according to a specific rule that will be explained later in this section. The initial state distribution is defined as:

$$\pi = \{\pi_j\} = P[q_1 = s_j], 1 \leq j \leq 2\Lambda + 1 \tag{4.10}$$

The state transition probability distribution is defined as:

$$A = \{a_{ij}\} = P[q_{t+1} = s_j | q_t = s_i], 1 \leq i, j \leq 2\Lambda + 1 \tag{4.11}$$

The state transition probability is defined as the probability that a layer boundary is at a range position at step t given that the same layer boundary was at a particular range

position at step $t-1$. The continuous emission probability densities are defined as:

$$B = \{b_j(\boldsymbol{O}_t)\} = P(\boldsymbol{O}_t|q_t = s_j), 1 \leq j \leq 2\Lambda + 1 \tag{4.12}$$

The model parameters A and B are properly initialized for the dataset under consideration and then recomputed by using the Baum-Welch algorithm [114]. For a more in depth discussion regarding the actual definition of the emission probability densities, the state transition probability distribution and the re-estimation procedure the reader shall refer to the experimental section (see Section 4.3.3). The method requires a minimum amount of human-aided training. For a given set of radargrams acquired by a sensor, the training is performed only once on a representative subset in terms of layer slopes variability and intensity. Then the method runs in a completely automatic way when a new radargram acquired by the same sensor has to be analysed. Moreover, the layers vertical shape in the radargram tends to be similar between different sensors, thus the training performed on a sensor could be suitable on datasets acquired by a different one. Note that, if the real sensor data is not available, the training can be easily performed on simulated data. Let us now focus on the proposed local VA implementation. The method is divided into the following seven parts. The illustrations of the whole modified Viterbi tracking procedure for a given single layer and multiple layers are shown in Fig. 4.3 and Fig. 4.4, respectively.

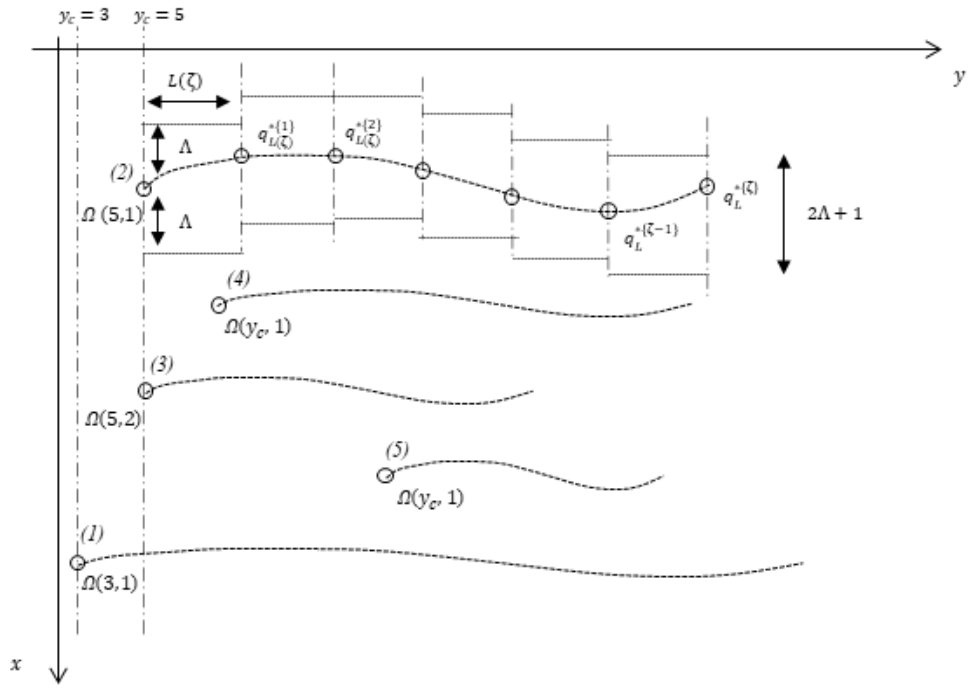

Figure 4.4: Illustration of the tracking procedure for a multiple layer boundary. The numbers denoted in brackets next to the initial seed represent the order in which the algorithm tracks the layer boundaries.

Index Settings

The seed function $\Omega(y_c, k)$ contains a variable number of k seeds seeds (i.e. initial tracking points) for each azimuth pixel index $y_c = 1, 2, ..., N_y - l + 1$. The variable y_c indicates the current azimuth position where the method is starting the computation for retrieving a given layer location. Moreover, l is the minimum azimuth extension of the layer boundary detected by the method. The seeds are retrieved by the operation of (4.5). The radargram is segmented along the azimuth direction y in sub-blocks of length $L(\zeta)$. For each block, the azimuth computation bounds are defined as:

$$y_1(\zeta) \leq y \leq y_2(\zeta) \tag{4.13}$$

where ζ is the index stating which block of the radargram is being processed:

$$\zeta = 1, 2, ... \lceil \frac{N_y - y_c}{l - 1} \rceil \tag{4.14}$$

For each ζ , the azimuth index bounds $y_1(z)$ and $y_2(z)$ are computed as:

$$y_1(\zeta) = \begin{cases} y_c & \zeta = 1 \\ y_2(\zeta - 1) & \zeta > 1 \end{cases} \tag{4.15}$$

$$y_2(\zeta) = min\{\zeta(l - 1) + y_c, N_y\} \tag{4.16}$$

The initial range pixel coordinate for the $\zeta - th$ computation is equal to:

$$\chi^{\{\zeta\}} = \begin{cases} \Omega(y_c, k) & \zeta = 1 \\ \chi_{L(\zeta-1)}(\zeta - 1) & \zeta > 1 \end{cases} \tag{4.17}$$

This means that, for the first block, the states under computation are centred on the $k - th$ tracked point at azimuth position y_c, while for $\zeta > 1$ they are centred on the last range pixel coordinate belonging to the sub-block optimal state path. The range interval considered for the $zeta - th$ computation is the following:

$$\chi^{\{\zeta\}} - \Lambda \leq x \leq \chi^{\{\zeta\}} + \Lambda \tag{4.18}$$

The state bound is selected according to the layer boundary variation rate along the azimuth direction. From (4.18) it is trivial to demonstrate that, for each given z, the number of states being processed is always equal to $2\Lambda + 1$. In the unlikely event that $\chi^{\{\zeta\}}$ is less than Λ pixels from the top or bottom edge of the radargram, one can pad with zero intensity pixels the bottom and/or the top edge of the related part of the radargram.

VA Initialization

Let the probability of the partial best path to a state j at time t be defined as $\delta_t(j)$ and let $\varphi_t(j)$ be the back-pointers matrix. The initial probability is set as:

$$\delta_1(j) = \{\pi_j\} = \begin{cases} 1 & j = \Lambda + 1 \\ 0 & elsewhere \end{cases} \tag{4.19}$$

This means that, due to (4.18),the most likely state at $t = 1$ is always the one geometrically centered in the sub-block (see also Fig. 4.3).The back pointers matrix for the first time step is set to $\varphi_1(j) = 0$.

VA Iteration

The induction part of the VA is computed according to the following equations:

$$\begin{aligned} \delta_t(j) = &\max_{1 \le i \le 2\Lambda+1} [\delta_{t-1}(j) a_{ij}] b_j(\boldsymbol{O}_t), \\ &2 \le t \le L(\zeta), 1 \le j \le 2\Lambda + 1 \end{aligned} \tag{4.20}$$

The observation vector is defined as:

$$\begin{aligned} \boldsymbol{O}_t = &[\hat{R}(\chi^{\{\zeta\}} - \Lambda, y_1(\zeta) + t - 1), ..., \hat{R}(\chi^{\{\zeta\}}, y_1(\zeta) + t - 1), ..., \\ &\hat{R}(\chi^{\{\zeta\}} + \Lambda, y_1(\zeta) + t - 1)] \end{aligned} \tag{4.21}$$

For each along-track position (i.e. time step), the observation vector $\boldsymbol{O}_t$ contains the intensity values extracted from the enhanced radargram $\hat{R}$ belonging to the range cut defined by the bound of (4.18). Thus its size is equal to $2\Lambda + 1$. The back pointer matrix is computed as:

$$\begin{aligned} \varphi_t(j) = &\max_{1 \le i \le 2\Lambda+1} [\delta_{t-1}(j) a_{ij}], \\ &2 \le t \le L(\zeta), 1 \le j \le 2\Lambda + 1 \end{aligned} \tag{4.22}$$

Termination

The algorithm is terminated when the last azimuth position of the block under investigation has been considered in the recursive computation such that:

$$q^{\star}_{L(\zeta)} = \arg \max_{1 \le i \le 2\Lambda+1} [\delta_{L(\zeta)}(i)] \tag{4.23}$$

Optimal State Sequence

The optimal state sequence is retrieved by back-tracing:

$$q^{\star}_t = \varphi_{t+1}(q^{\star}_{t+1}), t = L(\zeta) - 1, L(\zeta) - 2, .., 1 \tag{4.24}$$

The VA notation is expressed in a local (i.e. within the sub-block) coordinate frame. For retrieving the actual range pixel coordinates belonging to the optimal path, the following coordinate transformation can be performed:

$$\chi_t(z) = (\chi^{\{\zeta\}} - \Lambda - 1) + q_t^{\star} \tag{4.25}$$

The pixel intensities for the z-th block are stored in a matrix denoted as $I^{\{\zeta\}}$. The coordinates of each pixel of the detected layer are stored as following. Each column of the matrix represents a pair of coordinates (x, y):

$$P^{\{z\}} = \begin{bmatrix} \chi_1(\zeta) & \chi_2(\zeta) & \cdots & \chi_{L(\zeta)} \\ y_1(\zeta) & y_1(\zeta)+1 & \cdots & y_2(\zeta) \end{bmatrix} \tag{4.26}$$

Detected Layer Boundary (Detection Logic)

In this context, a drawback of the VA is that it cannot discriminate between noise pixels and signal pixels. This implies that if a layer has an azimuth extent smaller than the size of the radargram, and no stop condition is implemented, the VA algorithm will continue to chain blocks containing noise. Moreover, noise spikes in the $NR(x, y)$ radargram region may generate false layer boundaries. To overcome these issues, the discrimination between subsurface features and noise in the tracked layer boundary is done according to the following criterion. Let I_T be the set containing the elements of $I^{\{\zeta\}}$ exceeding the threshold value T_h, i.e.,

$$I_T = \{I^{\{\zeta\}} > T_h\} \tag{4.27}$$

A layer boundary block is considered detected if the following condition holds:

$$\frac{|I_T|}{L(\zeta)} > 0.5 \tag{4.28}$$

where $|I_T|$ is the set cardinality of I_T. According to (4.28), a simple majority rule is adopted. The detected layer is defined as the chaining of blocks defined in (4.26) for which the condition in (4.28) is verified (i.e. $[P^{\{1\}}P^{\{2\}}...P^{\{r\}}]$. The associated layer boundary amplitude vector (which describes the radiometric properties) can be derived as $[I^{\{1\}}I^{\{2\}}...I^{\{r\}}]$. The index $r \leq \max(\zeta)$ denoted the last block for which condition (4.28) is true. The overall azimuth extent of the layer boundary is equal to $y_1(\zeta = 1) \leq y \leq y_2(\zeta = r)$.

Layer removal from the observation matrix and update of the seed vector

As a final step the tracked layer is removed from the enhanced radargram all the pixel coordinates specified in $[P^{\{1\}}P^{\{2\}}...P^{\{r\}}]$ and the adjacent ones in the range direction having distance smaller than Λ. The seed vector is also updated removing all the seeds sharing the same coordinates with the retrieved layer position vector. This implies that the layers tracking order is dictated by the seeding strategy. The layers must be tracked sequentially left to right or right to left (with respect to the azimuth direction). The only tracking order that can be switched holding the same solution is the one when two

Table 4.1: Parameters of the considered SHARAD radargrams

Parameter	**Value**
Along Track Resolution	450 m
Across Track Resolution	3 Km
Sampling Frequency	26.667 MHz
Along Track Sampling	115 m
Range Resolution (ice)	10 m
Pixel Intensity Range of Values	[0-255]

layers start from different depths of the same azimuth position (i.e. top/bottom order). This seven step method is repeated for each azimuth position y until the azimuth position $y = N_y - l + 1$ has been reached. Finally, we derive the numerical value of the upper bound of the estimation error induced by segmentation. The decision whether a block contains a layer or not is taken according to (4.28). Thus if a layer spans an azimuth extent that is not a multiple of $L(\zeta)$ then the actual length may be under or over estimated. In both cases, the upper bound of this error is equal to $L(\zeta)/2$, thus smaller values of l should be preferred for reducing the error.

4.3 Experimental Results

This section presents the results obtained by the proposed technique applied to the real data set described in subsection 4.3.1. The other sub-sections are devoted to the qualitative and the quantitative analysis of the results obtained by applying the radargram pre-processing method described in section 4.2.1 and the layer detection technique described in sections 4.2.2 and 4.2.3.

4.3.1 Dataset Description

The considered dataset are radargrams obtained by the SHARAD instrument over the north polar layered deposits of Mars. In this paper, for comparison purposes, the same radargrams employed in [93] (see Fig. 4.5) are considered for evaluation. As already stated in [93], only the upper part of the radargrams is considered, which corresponds to a densely layered shallow subsurface. These areas can be automatically detected in a pre-processing phase by using the classification technique presented in [102]. The considered radargrams present a very limited amount of surface clutter thus the detection of layer boundaries is not ambiguous with respect to it. The main parameters of the radargrams are summarized in Table 4.1.

4.3.2 Proposed Method: Pre-Processing

This section presents the results obtained by the proposed denoising and enhancement technique over the data set under investigation. The value of N_{AV} [see (4.1)] has been set equal to 8 for the whole dataset. This value of N_{AV} has been chosen in order to guarantee an average $P_D \geq 0.95$ with a $P_{FA} = 10^{-3}$ for all the radargrams. The value

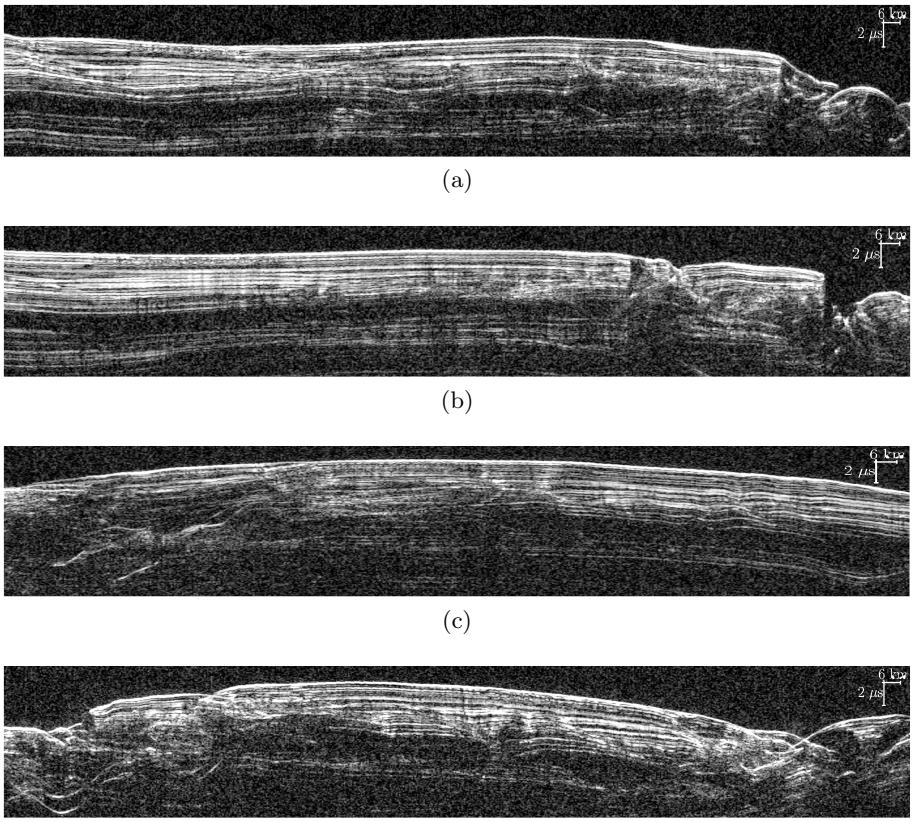

(a)

(b)

(c)

(d)

Figure 4.5: SHARAD radargrams considered in the experiments: (a) 52050100, (b) 528401000, (c) 1049190200 , and (d)1591701000. Figures from [93].

of the threshold T_h is computed according to (4.3) by fixing $P_{FA} = 10^{-3}$ after computing the conditional empirical noise distribution $p_n(\nu)$. The noise region within the radargram is automatically located by using the technique for the first return detection presented in [115]. For each range line, the technique finds the position of the first sample which is statistically different from the background noise thus allowing to isolate the radargram region above the surface layer. For the given data set the amount of samples extracted from the noise part of the radargram for computing the noise distribution is in the order of 10^4.According to the analysis carried out in [32], the layers of the NPLD region of Mars can be classified into four categories. Being only the densely layered upper part of the radargram considered, only strong layers (SL) and weak layers (WL) are taken into account. Accordingly, the parameter Υ has been fixed by considering an SNR value equal to:

$$SNR = 10\log_{10}(\sqrt{N_{AV}}\frac{SNR(SL) + SNR(WL)}{2}) \simeq 17dB \tag{4.29}$$

where $SNR(SL)$ and $SNR(WL)$ are the average SNR expressed in linear scale for strong layers and weak layers as in [115] and $\sqrt{N_{AV}}$ is the SNR gain due to incoherent averaging for both layer types. Considering the bandwidth and sampling frequency in Table I, the computation of (11) results in $\Upsilon = 1$ and thus the rectangular function of (10) has a width equal to 3 samples. It follows that the size of the Gaussian filter is 3 x 3. Fig. 4.6 shows a comparison between $\hat{R}(x, y)$ and the original radargram. Fig. 4.7 presents an example of an enhanced range line. The figures show that the method proved to be efficient in denoising the radargram and enhancing the underlying layering structure by showing features that are not easy to observe by visual inspection (see the example in Fig. 4.6). The effectiveness of denoising depends on the selected probability of false alarm. If the P_{FA} increases more details are in the image but at the cost of having more false alarms and vice-versa. In some regions, the radargram representation of the layers is still fragmented. This is expected due to the low signal to noise ratio. This issue is not of major concern since the proposed detection procedure based on the modified VA can reconstruct the layer azimuth continuity for small gaps induced by low SNR.

4.3.3 HMM Model Design and Parameters Tuning

The distribution of the observation vectors describing the typical signature of a layer for each state j is modeled as multivariate Gaussian distributions. This is justified by the fact that the last step of the pre-processing technique filters the radargram with a Gaussian filter. The continuous emission probability densities are given by:

$$b_j(\boldsymbol{O}_t) = \mathcal{N}(\boldsymbol{O}_t, \boldsymbol{\mu}_j, \boldsymbol{\Sigma}_j) \tag{4.30}$$

where $\boldsymbol{\mu}_j$ and $\boldsymbol{\Sigma}_j$ are the mean vector and covariance matrix, respectively. The state bound Λ has been experimentally set to 3. The estimation of the parameters of the multivariate normal distribution was performed by acquiring from different denoised and enhanced radargrams about 10^5 realizations of the vector $\boldsymbol{O}_t$ belonging to each state j. The parameters of the Gaussian distribution (i.e., $\boldsymbol{\mu}_j$,$\boldsymbol{\Sigma}_j$) were computed by maximum likelihood estimation. The mean observation vectors μ_j are shown in Fig. 4.8. By as-

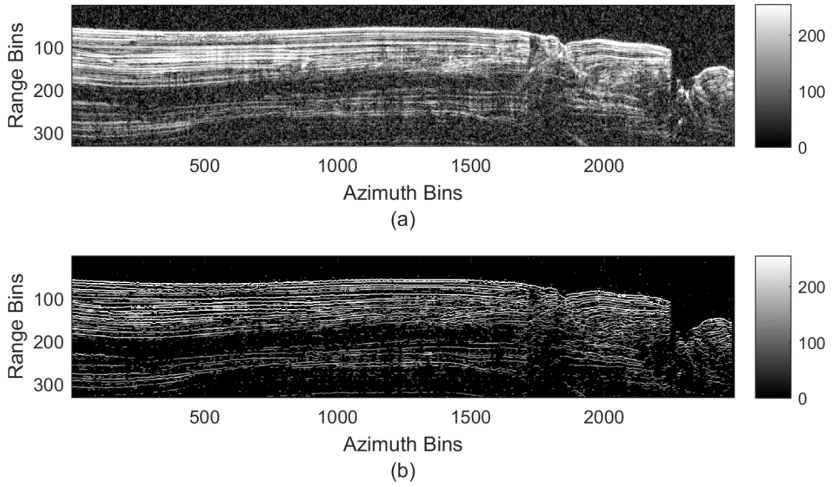

Figure 4.6: (a) Original Radargram 528401000 (b) Radargram obtained by the proposed denoising and enhancement technique $P_{FA} = 10^{-3}$. Gray levels represent pixel intensity.

suming $\Lambda = 3$ the size of the observation vector is 7. In Fig. 4.8 one can see that the mean vectors are shifted replicas of each other. To give an example, the mean observation vector of state 4 has a symmetric triangular shape which represents a layer perfectly centered in a given down-range cut within the current radargram sub-block being processed. The state transition probability distribution is initialized with the following triangular function (a similar definition is given in [98]) :

$$a_{ij} = \begin{cases} (1 - \dfrac{|i-j|}{\sigma_v})\dfrac{1}{\sigma_v} & |i-j| \leq \sigma_v \\ 0 & |i-j| > \sigma_v \end{cases} \tag{4.31}$$

where σ_v is an application dependent scalar value (expressed in number of pixels) that models the lateral continuity of the layer boundary. This parameter is set to $\sigma_v = 4$, which has experimentally proven to be the most appropriate value for the data set under consideration. Then the model parameters A and B are recomputed by the Baum-Welch procedure according to the equations given in [114]. Due to the fact that the state conditioned emission probabilities are modeled as multivariate Gaussian distributions, the related equations given in [114] were implemented for re-estimating the mean vector and covariance matrix for each state taking into account multiple observation sequences. The re-estimated values of a_{ij} are shown in Fig. 4.9. The dataset used for training is very large and made up of 10^3 layers handpicked by an expert operator along with their trajectories. The training procedure is performed only once and the method runs in a completely automatic way when a new inputs radargram is processed. The training set is selected such that is representative in terms of slope variability and pixel intensity of the entire dataset. If a real training set cannot be defined, the training procedure could

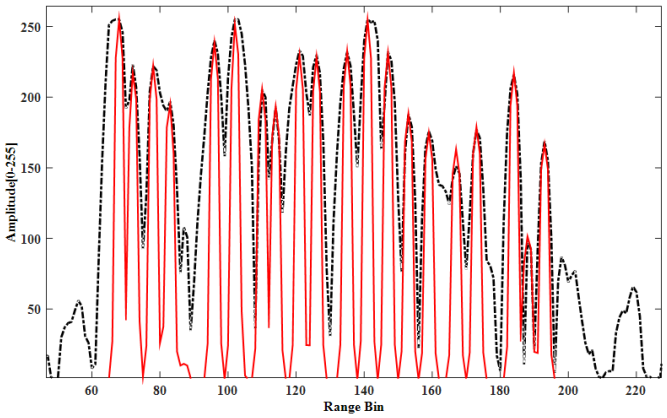

Figure 4.7: Example of an enhanced range line (red continuous) compared to the original range trace with no incoherent averaging (dashed black line). The in between layer boundary signal is greatly reduced in the enhanced case. In the plot T_h is set automatically by the algorithm to 100.

be easily performed on simulated radargrams that reproduce the physical properties of the layers. It is worth nothing that, due to the almost invariant physical properties of a layer in the range direction, a training performed over a dataset is likely to be suitable for application over a different dataset.

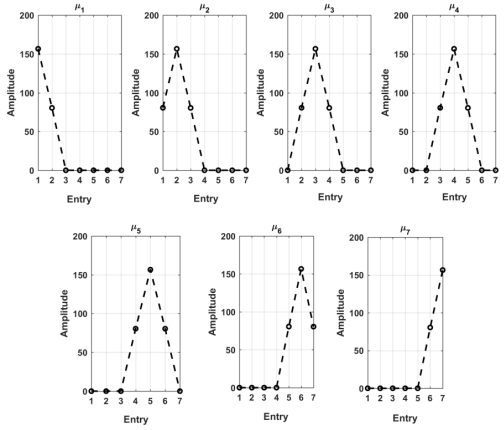

Figure 4.8: Mean Vectors $\boldsymbol{\mu}_j$ of the multivariate Gaussian distribution for each state j. The mean vectors were estimated by a Maximum Likelihood algorithm on the training data.

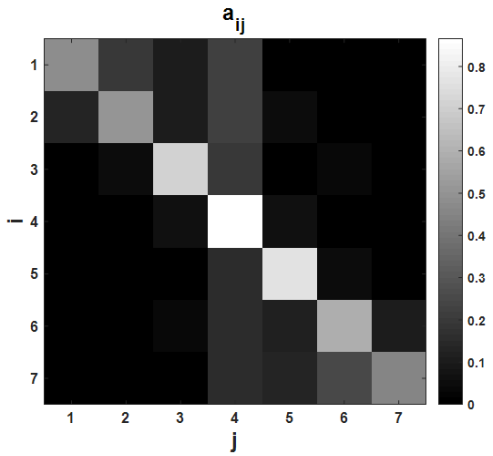

Figure 4.9: Re-estimated values a_{ij} of the state transition probability distribution according to the Baum-Welch algorithm.

4.3.4 Layer Boundaries Detection with the Combination of the HMM/VA

The $\hat{R}$ matrix obtained by the pre-processing step, the emission probability densities and the state transition probability distribution are the main inputs to the layer boundaries detection technique. The minimum layer extension l is set equal to 10 pixels in accordance with [93]. Layer boundaries showing an inclination greater than 45 degrees are discarded because features with high slopes have high probability of being false alarms due to limitations in the focusing processor applied to the data [93]. The detection and false alarm rates are evaluated by comparing the detected layer boundaries with the same subsurface reference maps used in [93]. A layer is counted as a correct detection if for each range line its position deviation from the given subsurface reference layer is within the range resolution of the sensor. For this particular data set, a layer is counted as detection if it lies within +1/-1 pixels from the actual position of the subsurface reference map. A layer is considered as a false alarm if it does not match this criterion. The margin value has been computed according to equation (4.9) which indeed takes into account the sensor resolution. Our approach exhibits a sharp increase in detection rate equal to $11\% + /-1.5\%$ when compared to the considered reference method (see Table 4.2 and Fig. 4.10). The number of false alarms is also significantly decreased. The improved performances can be largely explained by the fact that the proposed technique has a denoising step that better preserves the finer details of the data. The results on the number of detected, missed and false alarms versus the layer length are in accordance with the above consideration since, with respect to [93], there is an increase in the detection of shorter layers (see Fig. 4.11). Short layers are usually associated with finer details of the radargram. This behavior is observed on all the radargrams of the considered data-set. In fact, the BM3D filter used in [93] may generate unwanted artifacts that affect the quality of the radargram by masking finer details for low values of SNR. The property of the modified VA of getting through noise garbles allows a better reconstruction (i.e. less fragmentation) of the overall azimuth extension of the layer boundary thus acting as a

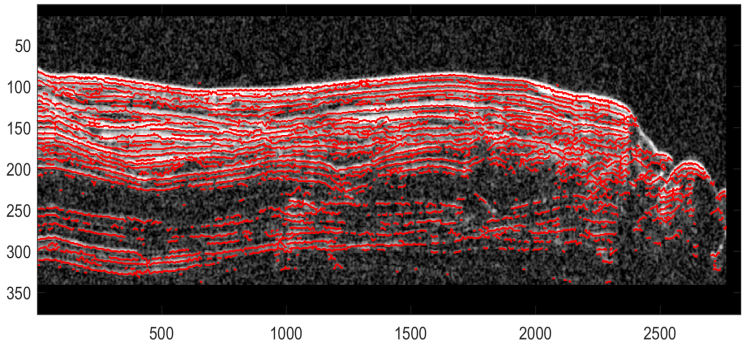

(a)

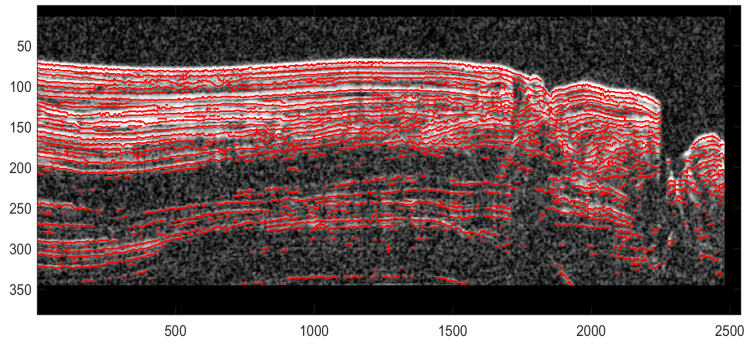

(b)

Figure 4.10: Detection results obtained by the proposed technique on SHARAD radargrams (a) 52050100, (b) 528401000. In the radargram 52050100 part of the surface layer is not detected due to the constraint on the maximum slope. This is of no concern since we are interested in the detection of the subsurface.

sort of regularization step. This is especially evident in noisy regions of the radargram (see Fig. 4.12). Another important feature of the proposed technique is that it tracks the layer boundaries pixel-by-pixel allowing a better representation of the layer variation when compared with the results of [93]. We performed simulations in order to assess whether the concatenated solution computed by the proposed method is the actual optimal state path solution. Studies have proven that the truncation of VA causes a negligible degradation (see [113]). If the truncation depth (line length in this context) is large enough then the effect on performance is negligible. To investigate this effect, we performed simulations consisting in computing the best path over a synthetic radargram with a number of time steps equal to 2500 (similar to a typical full radargram extent in the azimuth direction). The computed best path is compared with the best path computed as the concatenation of blocks for different truncation lengths L and for a varying SNR. The synthetic radargram has been modeled as a single layer over Rayleigh background noise according to [115] which results in the exponential distribution when the intensity is retrieved. We performed a Monte Carlo simulation with 200 runs for each combination of SNR and L values. The truncation error is computed as the number of times over the number of runs in which the truncated path differs at least by one retrieved state from the best path computed over the full layer. The results reported in Fig. 4.13 show that the truncation error is negligible. This is especially true considering that in the radargrams under consideration the SNR is about 17 dB. Regarding the computational complexity, the overall technique average running time required for processing a full radargram is less than 30 seconds on a workstation with 8 GB of RAM and an Intel Core i5-4590 processor with 3.3 GHz clock frequency. This is half the computational time required by the technique in [93]. Note that the computational complexity of the overall algorithm is bounded by the complexity of the VA, which is sharply reduced by the strategy outlined in Section 4.2.2 and 4.3.3. The number of states explored with our technique for each computation is equal to $2\Lambda+1$. The nominal VA computational complexity is polynomial and equal to $O(N_L N_y N_x^2)$, where N_L is the number of layer boundaries in the radargram. In our method, the subdivision of the radargram along the azimuth direction in blocks neither reduces nor increases the computation complexity. On the other hand, the proposed method reduces the number of states evaluated for each computation. Accordingly, the computational complexity of the proposed method is:

$$O(N_L N_y(2\Lambda + 1) + o_h) \tag{4.32}$$

The parameter $o_h \approx= 4N_{Pfa} l\Lambda^2$ is the computation overhead of the method, where N_{pfa} is the overall number of false alarms. This undesired computation overhead is due to the fact that the seed vector may contain noise spikes exceeding the threshold T_h. Thus before discarding the "noise layer", the modified VA computes an optimal local state path with azimuth extend equal to l. The computational complexity reduction of the proposed technique compared to a naïve VA implementation is equal to:

$$\frac{4N_L N_y \Lambda^2 + o_h}{N_L N_y N_x^2} \approx (\frac{2\Lambda}{N_x})^2 \tag{4.33}$$

Table 4.2: Comparison of correct detection and false alarms obtained by the proposed technique and the considered reference technique

		Proposed Technique		**Reference Technique Ferro et al. (2013)**	
Radargram Identifier	**Number of Lines**	**Detected Lines**	**False Alarms**	**Detected Lines**	**False Alarms**
52051000	777	722	27	636	63
528401000	768	705	37	601	52
1041902000	694	663	33	591	78
1591701000	754	690	31	610	48

Being Λ in the order of 10, the number of rows of the radargram N_x (i.e. possible states) in the order of $4 \cdot 10^3$, $N_L \approx 700$, and N_y in the order of 10^3 we can assume o_h contribution negligible. According to (4.33), the average decrease in computational complexity with respect to naïve VA implementation is very sharp and in the order of 10^5 operations.

4.4 Conclusions

In this chapter, a novel automatic technique for retrieving the position and the radiometric properties of layer boundaries in radargrams acquired by radar sounders data has been presented. The technique is based on a statistical approach that detects the spatial position of the layer boundaries by using an inference procedure. This approach is particularly suitable to the analysis of data having a low SNR (e.g. planetary data). The radargram is modelled as a trellis and its parameters (e.g, pixel intensity and depth) are mapped into the relevant parameters of a HMM. In order to infer the layer boundaries position, the VA is applied to the underlying HMM. However, when low SNR radargrams are considered, the application of the VA algorithm is not trivial due to the radargrams fragmented and dense layering structure. Thus, we proposed a modification of the algorithm based on a divide and conquer strategy where the radargram is split into blocks on which both the inference and the discrimination between noise and layer boundaries are performed. The proposed technique has substantial advantages in terms of computational complexity when compared to the standard VA, even if the retrieved state path may not represent the optimal state path provided by the optimal VA implementation. However, as discussed in the paper and empirically assessed, the discrepancy in the computed path between our technique and original VA is negligible for this type of application. In this work, we have also proposed a novel pre-processing technique for the denoising and enhancement of radargrams. The proposed technique takes into account the main variables affecting a radar acquisition and unwanted artifacts to produce an enhanced representation of the radargram which is propaedeutic to the subsequent detection steps. The combination of the proposed denoising and structure enhancement with the detection step performed by the modified VA resulted in a higher probability of detection and lower false alarm rate when compared to a recent literature technique. It is worth nothing that the detection of the proposed method is performed on a pixel-by-pixel basis. Accordingly, the azimuth

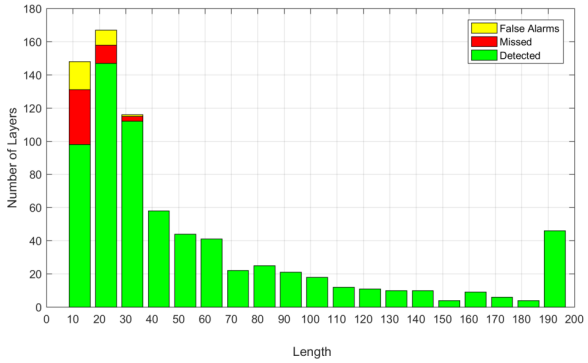

(a)

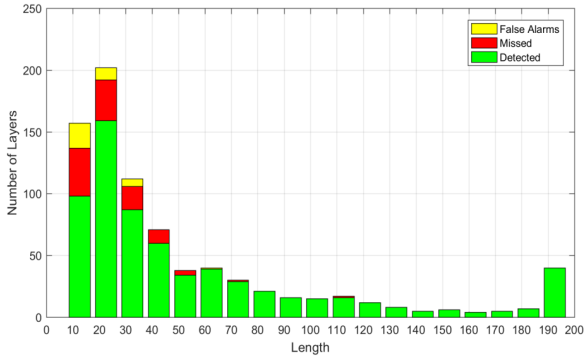

(b)

Figure 4.11: Histogram representing the number of detected, missed and false layers vs their length obtained by the proposed technique on SHARAD radargrams (a) 52050100, (b) 528401000. The Histogram bin quantization of the layer length is equal to 10 (i.e. equal to the line quantization step l) which is slightly different from the bin quantization of [93] that is equal to 5. Nevertheless, the results are still comparable. The last bin of the histogram contains all the lines with length equal or greater than 195 as in [93].

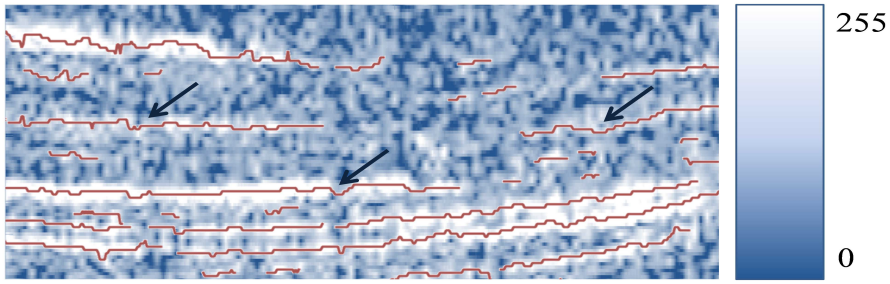

(a)

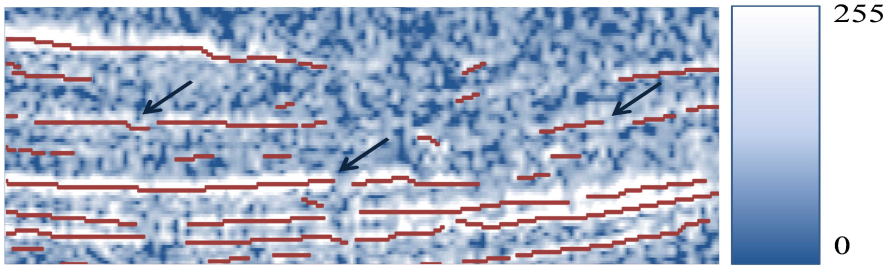

(b)

Figure 4.12: Layer Detection performances comparison between the proposed and the state-of-the-art method [93]. (a) Proposed Method (Weak Layers); (b) Method in [93] (Weak Layers). The detected layers are depicted in red overlapped on a false color amplitude representation of a portion of the Radargram 528401000. Black Arrows show example of areas where the proposed method improves the layer continuity.

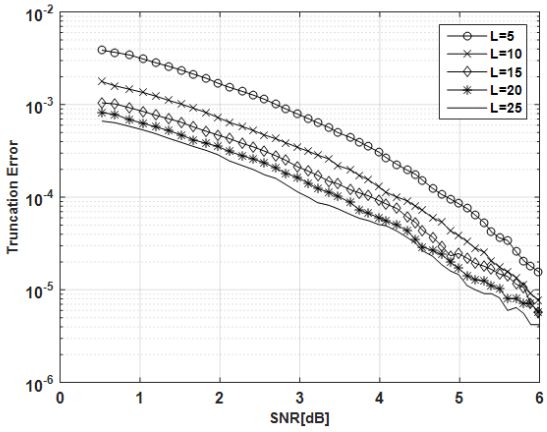

Figure 4.13: VA Truncation Error as function of SNR and line length

variations of the layer boundaries are better retrieved from the radargram, when compared to previously developed methods for planetary data. As a result of the inherent property of VA of getting through noise garbles, the method also partially acts as a regularization step of the noisy data.

Conclusions

This chapter concludes the thesis by presenting a general discussion of the work described and by providing a summary of the novel contributions illustrated in the document. Finally, possible future developments of the proposed research work are presented.

Summary and Discussion

Radar sounders are very valuable systems for subsurface investigation. In this thesis, we investigated three different aspects of radar sounding namely (i) system design, (ii) low-level processing and (iii) high level processing.
For each aspect, we presented a main novel contributions to the radar sounding state of the literature. The first part of thesis (Chapter 2), which represents the contribution related to system design, has been devoted to the investigation of the design requirements, performance assessment and 3D electromagnetic simulations of a radar sounder specifically designed for detecting Moon lava tubes from orbit. The results show that a multi-frequency radar sounder is the best option for effectively sounding lava tubes in the Maria region of the Moon. According to planetary studies, Lunar Marias are the most likely regions for the putative presence of lava tubes. The possible range for the selection of the probing two central frequencies, which allow to sound most of the lava tube dimension hypothesized in the literature, is between 10 and 15 MHz for the low carrier frequency and between 60 and 65 MHz for the high carrier frequency. The basalt substrate roughness which is in the order of meters along with its thickness are the two main driving factors for the radar performance thus severely limiting sounding at frequencies above 80 MHz. The objective of the 3D electromagnetic simulations was focused in understanding the typical electromagnetic response of a lava tube considering different geometric configuration for the acquisition scenario The results of the electromagnetic simulation highlighted the fact that lava tubes display a unique signature consisting in a phase inversion that can be exploited for their identification. This signature remains clearly detectable even in the presence of off-nadir surface clutter, which does not exhibits the same mechanism of inversion of the phase.
Off-nadir surface clutter is arguably one of the main issue affecting radar sounding. It hinders radar sounders recorded data interpretation by planetary geophysicists. To this extent, in the second novel contribution focused on low-level processing (Chapter 3), we proposed an adaptation of the unique bat clutter discrimination capability to radar sounding by devising novel clutter detection model based on a frequency diversity approach. We proved that the bats powerful and relatively simple processing strategy can be math-

ematically modeled and adapted to radar sounding as there are many striking analogies between a radar and a bat such as the nadir acquisition geometry. The method allows the prediction of the radar performance to be tailored as a function of the transmitted frequencies and of the surface and subsurface characteristics. The proposed bio-inspired model has been tested on SHARAD data acquired over Mars and has been validated on different regions characterized by diverse subsurface geoelectrical properties such as icy and arid areas. The experimental results showed that the proposed method can obtain in an immediate and reliable way a clear discrimination of the subsurface signal from the off-nadir clutter and that the model is in good agreement with the observations (e.g. expected values of the surface and subsurface power ratios). Compared to traditional studies manually performed by geophysicists, in our case the discrimination is performed in an automatic way and without relying on a digital elevation model of the surface which is not always available in the planetary case.
It is worthy nothing that, there is a clear synergy between the results of the system design study and the low-level processing one. The bio-inspired clutter detection method can be easily applied to the multi-frequency radar sounder for lava tube detection. This synergistic approach paves the way for a new generation of radar sounders which eases the data interpretation by planetary scientists.
The proposed approach for low-level processing eases the data interpretation but it does not provide high-level information regarding the detected geological structure. There is still a lack in the literature of high-level processing techniques for the automatic analysis and extraction of features from radar sounder data. As a consequence, most of the radar sounder data analysis is performed manually by experts and thus is inherently subjective and time-consuming. Accordingly, the third novel contribution presented in Chapter 4 focuses on high-level processing and in particular on the automatic and reliable extraction of high-level information from radargrams. Specifically, we proposed a technique for the automatic detection of layer boundaries in radar sounding data. The analysis of the ice stratification (i.e. layering) performed by geophysicists is particularly important since can be used for dating purposes and for the understanding of the past climate of a given geographical area. Our proposed approach to the automatic detection of layering is based on a local scale Hidden Markov Model (HMM), which model the radar response in the presence of a layer boundary, and the Viterbi Algorithm, which performs the inference step. This approach has the advantage of performing inference by explicitly modeling the spatial and radiometric uncertainty of the data induced by noise. Furthermore, a novel radargram enhancement and denoising technique tailored to support the detection step is presented. The effectiveness of the proposed technique has been confirmed by testing it on different radargrams acquired by SHARAD over the North Pole of Mars which show subsurface stratification. The results obtained point out the superiority of the proposed method in retrieving the position of each layer boundary and its characteristics with respect to the state-of-the-art techniques. The proposed technique can be included in a basic processing chain for radar sounding data. In this way, it is possible to generate high-level products that can be distributed along with radargrams.

Future Developments

The possible future developments of this thesis are briefly discussed in this section. A natural development for the multi-frequency radar sounder work is to analyse Moon radar sounding data recorded by the Lunar Radar Sounder(LRS) instrument and verify whether there are evidence of the lava tubes electromagnetic signatures presented in this paper. This can be done by taking into account the inherent limitation of LRS in terms of lava tubes detection capability being the system not specifically designed for this task.
For the bio-inspired clutter detection model, several engineering aspects can be further investigated such as the optimal probing frequency selection for clutter discrimination as function of a particular acquisition scenario. A potential test case for the model application is the lava tube sounding described in the first part of the thesis. To this extent, we can envision an holistic approach where the different contributions of this thesis (i.e. system design, low-level and high-level processing) are combined to form a processing chain for a potential future sounding mission based on a multi-frequency radar. In fact, the approach for the automatic layering detection based on a local scale Hidden Markov Model and the Viterbi algorithm can be easily adapted to other applications and thus offers the opportunity to expand this particular work in the direction of recognizing other type of features than layering such as lava tubes typical electromagnetic signatures.

List of Publications

Journal Papers

[1] **L. Carrer**, C. Gerekos and L. Bruzzone, "A Multi-Frequency Radar Sounder for Lava Tubes Detection on the Moon: Design, Performance Assessment and Simulations", Planetary and Space Science, in Press

[2] **L. Carrer** and L. Bruzzone, "Solving for Ambiguities in Radar Geophysical Exploration of Planetary Bodies by Mimicking Bats Echolocation", Nature Communications, 8.1 (2017): 2248.

[3] **L. Carrer** and L. Bruzzone "Automatic Enhancement and Detection of Layering in Radar Sounder Data Based on a Local Scale Hidden Markov Model and the Viterbi Algorithm", IEEE Transactions on Geoscience and Remote Sensing, 55.2 (2017): 962-977.

[4] Dustin M. Schroeder, Andrew Romero-Wolf, **Leonardo Carrer**, Cyril Grima, Bruce A. Campbell, Wlodek Kofman, Lorenzo Bruzzone, Donald D. Blankenship, "Assessing the potential for passive radio sounding of Europa and Ganymede with RIME and REASON", Planetary and Space Science, Volume 134, 1 December 2016, Pages 52-60.

International Conferences

[1] L. Bruzzone, F.Bovolo, **L. Carrer**, A.M. Ilisei , "STRATUS: Satellite Radar Sounder for Earth Subsurface Sensing", in 103 Congresso Nazionale Società Italiana di Fisica (SIF), 2017.

[2] **L. Carrer**, C. Gerekos, and L. Bruzzone. "Detection of Lunar Lava Tubes with Orbiting Radar Sounder Systems", European Planetary Science Congress (EPSC) 2017.

[3] **L. Carrer** and L. Bruzzone, "A bat inspired technique for clutter reduction in radar sounder systems", Proc. SPIE 10004, Image and Signal Processing for Remote Sensing XXII, 1000417, (October 18,2016). **(Best Student Paper Award)**.

[4] L. Bruzzone, **L. Carrer**, A. Tamponi, E. Pettinelli, S.E. Lauro, R. Orosei, F. Bovolo, " A Radar Sounder Instrument for the Analysis of Venus Sub-surface", in International Venus Conference 2016.

[5] **L. Carrer**, R. Croci, and L. Bruzzone. "A robust on-board tracking technique for spaceborne radar sounders." Geoscience and Remote Sensing Symposium (IGARSS), 2015 IEEE International. IEEE, 2015.

Bibliography

[1] L. M. Prockter, "Ice in the solar system," *Johns Hopkins APL technical digest*, vol. 26, no. 2, pp. 175–188, 2005.

[2] T. Prettyman, N. Yamashita, M. Toplis, H. McSween, N. Schörghofer, S. Marchi, W. Feldman, J. Castillo-Rogez, O. Forni, D. Lawrence *et al.*, "Extensive water ice within ceres' aqueously altered regolith: Evidence from nuclear spectroscopy," *Science*, vol. 355, no. 6320, pp. 55–59, 2017.

[3] D. M. Blair, L. Chappaz, R. Sood, C. Milbury, A. Bobet, H. J. Melosh, K. C. Howell, and A. M. Freed, "The structural stability of lunar lava tubes," *Icarus*, vol. 282, pp. 47 – 55, 2017. [Online]. Available: http://www.sciencedirect.com/science/article/pii/S0019103516303566

[4] I. H. Woodhouse, *Introduction to microwave remote sensing*. CRC press, 2005.

[5] A. H. Waite and S. Schmidt, "Gross errors in height indication from pulsed radar altimeters operating over thick ice or snow," *Proceedings of the IRE*, vol. 50, no. 6, pp. 1515–1520, 1962.

[6] L. J. Porcello, R. L. Jordan, J. S. Zelenka, G. F. Adams, R. J. Phillips, W. E. Brown, S. H. Ward, and P. L. Jackson, "The apollo lunar sounder radar system," *Proceedings of the IEEE*, vol. 62, no. 6, pp. 769–783, June 1974.

[7] R. Seu, R. J. Phillips, D. Biccari, R. Orosei, A. Masdea, G. Picardi, A. Safaeinili, B. A. Campbell, J. J. Plaut, L. Marinangeli, S. E. Smrekar, and D. C. Nunes, "Sharad sounding radar on the mars reconnaissance orbiter," *Journal of Geophysical Research: Planets*, vol. 112, no. E5, pp. n/a–n/a, 2007, e05S05.

[8] G. Picardi, J. J. Plaut, D. Biccari, O. Bombaci, D. Calabrese, M. Cartacci, A. Cicchetti, S. M. Clifford, P. Edenhofer, W. M. Farrell, C. Federico, A. Frigeri, D. A. Gurnett, T. Hagfors, E. Heggy, A. Herique, R. L. Huff, A. B. Ivanov, W. T. K. Johnson, R. L. Jordan, D. L. Kirchner, W. Kofman, C. J. Leuschen, E. Nielsen, R. Orosei, E. Pettinelli, R. J. Phillips, D. Plettemeier, A. Safaeinili, R. Seu, E. R. Stofan, G. Vannaroni, T. R. Watters, and E. Zampolini, "Radar soundings of the subsurface of mars," *Science*, vol. 310, no. 5756, pp. 1925–1928, 2005.

[9] T. Ono, A. Kumamoto, H. Nakagawa, Y. Yamaguchi, S. Oshigami, A. Yamaji, T. Kobayashi, Y. Kasahara, and H. Oya, "Lunar radar sounder observations of subsurface layers under the nearside maria of the moon," *Science*, vol. 323, no. 5916, pp. 909–912, 2009.

[10] J. J. Plaut, G. Picardi, A. Safaeinili, A. B. Ivanov, S. M. Milkovich, A. Cicchetti, W. Kofman, J. Mouginot, W. M. Farrell, R. J. Phillips, S. M. Clifford, A. Frigeri, R. Orosei, C. Federico, I. P. Williams, D. A. Gurnett, E. Nielsen, T. Hagfors, E. Heggy, E. R. Stofan, D. Plettemeier, T. R. Watters, C. J. Leuschen, and P. Edenhofer, "Subsurface radar sounding of the south polar layered deposits of mars," *Science*, vol. 316, no. 5821, pp. 92–95, 2007.

[11] R. Seu, R. J. Phillips, G. Alberti, D. Biccari, F. Bonaventura, M. Bortone, D. Calabrese, B. A. Campbell, M. Cartacci, L. M. Carter, C. Catallo, A. Croce, R. Croci, M. Cutigni, A. D. Placido, S. Dinardo, C. Federico, E. Flamini, F. Fois, A. Frigeri, O. Fuga, E. Giacomoni, Y. Gim, M. Guelfi, J. W. Holt, W. Kofman, C. J. Leuschen, L. Marinangeli, P. Marras, A. Masdea, S. Mattei, R. Mecozzi, S. M. Milkovich, A. Morlupi, J. Mouginot, R. Orosei, C. Papa, T. Paternò, P. P. del Marmo, E. Pettinelli, G. Pica, G. Picardi, J. J. Plaut, M. Provenziani, N. E. Putzig, F. Russo, A. Safaeinili, G. Salzillo, M. R. Santovito, S. E. Smrekar, B. Tattarletti, and D. Vicari, "Accumulation and erosion of mars' south polar layered deposits," *Science*, vol. 317, no. 5845, pp. 1715–1718, 2007.

[12] B. Schmidt, D. Blankenship, G. Patterson, and P. Schenk, "Active formation of'chaos terrain'over shallow subsurface water on europa," *Nature*, vol. 479, no. 7374, p. 502, 2011.

[13] G. Oswald and G. d. Q. Robin, "Lakes beneath the antarctic ice sheet," *Nature*, vol. 245, no. 5423, pp. 251–254, 1973.

[14] M. J. Siegert, R. Kwok, C. Mayer, and B. Hubbard, "Water exchange between the subglacial lake vostok and the overlying ice sheet," *Nature*, vol. 403, no. 6770, p. 643, 2000.

[15] F. T. Ulaby, E. Michielssen, and U. Ravaioli, "Fundamentals of applied electromagnetics 6e," *Boston, Massachussetts: Prentice Hall*, 2010.

[16] B. A. Campbell, *Radar remote sensing of planetary surfaces*. Cambridge University Press, 2002.

[17] L. Bruzzone, G. Alberti, C. Catallo, A. Ferro, W. Kofman, and R. Orosei, "Subsurface radar sounding of the jovian moon ganymede," *Proceedings of the IEEE*, vol. 99, no. 5, pp. 837–857, May 2011.

[18] F. Ulaby, D. Long, W. Blackwell, C. Elachi, and K. Sarabandi, *Microwave Radar and Radiometric Remote Sensing*. University of Michigan Press, 2014.

[19] D. M. Schroeder, A. Romero-Wolf, L. Carrer, C. Grima, B. A. Campbell, W. Kofman, L. Bruzzone, and D. D. Blankenship, "Assessing the potential for passive radio sounding of europa and ganymede with rime and reason," *Planetary and Space Science*, vol. 134, pp. 52 – 60, 2016. [Online]. Available: http://www.sciencedirect.com/science/article/pii/S0032063316301465

[20] I. A. Crawford, "Lunar resources: A review," *Progress in Physical Geography*, vol. 39, no. 2, pp. 137–167, 2015.

[21] F. Horz, "Lava tubes - Potential shelters for habitats," in *Lunar Bases and Space Activities of the 21st Century*, W. W. Mendell, Ed., 1985, pp. 405–412.

[22] R. Greeley, *Introduction to Planetary Geomorphology*. Cambridge University Press, 2013. [Online]. Available: https://books.google.it/books?id=fZwNNP-IzicC

[23] G. De Angelis, J. Wilson, M. Clowdsley, J. Nealy, D. Humes, and J. Clem, "Lunar lava tube radiation safety analysis," *Journal of radiation research*, vol. 43, no. S, pp. S41–S45, 2002.

[24] L. Chappaz, R. Sood, H. J. Melosh, K. C. Howell, D. M. Blair, C. Milbury, and M. T. Zuber, "Evidence of large empty lava tubes on the moon using grail gravity," *Geophysical Research Letters*, vol. 44, no. 1, pp. 105–112, 2017.

[25] A. Arya, R. Rajasekhar, G. Thangjam, A. Kumara, and A. Kiran Kumara, "Detection of potential site for future human habitability on the moon using chandrayaan-1 data." *Current Science (00113891)*, vol. 100, no. 4, 2011.

[26] J. Haruyama, K. Hioki, M. Shirao, T. Morota, H. Hiesinger, C. H. van der Bogert, H. Miyamoto, A. Iwasaki, Y. Yokota, M. Ohtake *et al.*, "Possible lunar lava tube skylight observed by selene cameras," *Geophysical Research Letters*, vol. 36, no. 21, 2009.

[27] B. A. Campbell, B. Ray Hawke, G. A. Morgan, L. M. Carter, D. B. Campbell, and M. Nolan, "Improved discrimination of volcanic complexes, tectonic features, and regolith properties in mare serenitatis from earth-based radar mapping," *Journal of Geophysical Research: Planets*, vol. 119, no. 2, pp. 313–330, 2014.

[28] L. J. Porcello, R. L. Jordan, J. S. Zelenka, G. F. Adams, R. J. Phillips, W. E. Brown, S. H. Ward, and P. L. Jackson, "The apollo lunar sounder radar system," *Proceedings of the IEEE*, vol. 62, no. 6, pp. 769–783, June 1974.

[29] T. Ono and H. Oya, "Lunar radar sounder (lrs) experiment on-board the selene spacecraft," *Earth, Planets and Space*, vol. 52, no. 9, pp. 629–637, 2000. [Online]. Available: http://dx.doi.org/10.1186/BF03351671

[30] J. Haruyama, T. Kaku, R. Shinoda, W. Miyake, A. Kumamoto, K. Ishiyama, T. Nishibori, K. Yamamoto, K. Kurosawa, A. Suzuki *et al.*, "Detection of lunar lava tubes by lunar radar sounder onboard selene (kaguya)," in *Lunar and Planetary Science Conference*, vol. 48, 2017.

[31] T. Kaku, J. Haruyama, W. Miyake, A. Kumamoto, K. Ishiyama, T. Nishibori, K. Yamamoto, S. T. Crites, T. Michikami, Y. Yokota *et al.*, "Detection of intact lava tubes at marius hills on the moon by selene (kaguya) lunar radar sounder," *Geophysical Research Letters*, 2017.

[32] R. Sood, H. J. Melosh, and K. Howell, "Lunar advanced radar orbiter for subsurface sounding (laross): lava tube exploration mission," in *AAS/AIAA 26th Space Flight Mechanics Meeting*, 2016.

[33] H. Miyamoto, J. Haruyama, T. Kobayashi, K. Suzuki, T. Okada, T. Nishibori, A. P. Showman, R. Lorenz, K. Mogi, D. A. Crown *et al.*, "Mapping the structure and depth of lava tubes using ground penetrating radar," *Geophysical research letters*, vol. 32, no. 21, 2005.

[34] C. R. Rowell, A. Pidlisecky, J. D. Irving, and R. J. Ferguson, "Characterization of lava tubes using ground penetrating radar at craters of the moon national monument, usa." CREWES Research Report, 22, 1-18, Tech. Rep., 2010.

[35] G. R. Olhoeft, D. Sinex, K. Sander, M. Lagmanson, D. Stillman, S. Lewis, B. Clark, E. Wallin, and J. Kauahikaua, "Hot and cold lava tube characterization with ground penetrating radar," in *8th International Conference on Ground Penetrating Radar*. International Society for Optics and Photonics, 2000, pp. 482–487.

[36] C. R. Coombs and B. Hawke, "A search for intact lava tubes on the moon: Possible lunar base habitats," in *Lunar Bases and Space Activities of the 21st Century*, 1992.

[37] K. A. Howard, J. W. Head, and G. A. Swann, "Geology of hadley rille," 1972.

[38] M. Robinson, J. Ashley, A. Boyd, R. Wagner, E. Speyerer, B. R. Hawke, H. Hiesinger, and C. Van Der Bogert, "Confirmation of sublunarean voids and thin layering in mare deposits," *Planetary and Space Science*, vol. 69, no. 1, pp. 18–27, 2012.

[39] W. Fa, M. A. Wieczorek, and E. Heggy, "Modeling polarimetric radar scattering from the lunar surface: Study on the effect of physical properties of the regolith layer," *Journal of Geophysical Research: Planets*, vol. 116, no. E3, 2011.

[40] M. Rosenburg, O. Aharonson, J. Head, M. Kreslavsky, E. Mazarico, G. A. Neumann, D. E. Smith, M. H. Torrence, and M. T. Zuber, "Global surface slopes and roughness of the moon from the lunar orbiter laser altimeter," *Journal of Geophysical Research: Planets*, vol. 116, no. E2, 2011.

[41] Y. G. Shkuratov and N. V. Bondarenko, "Regolith layer thickness mapping of the moon by radar and optical data," *Icarus*, vol. 149, no. 2, pp. 329–338, 2001.

[42] G. R. Olhoeft and D. Strangway, "Dielectric properties of the first 100 meters of the moon," *Earth and Planetary Science Letters*, vol. 24, no. 3, pp. 394–404, 1975.

[43] G. Picardi, D. Biccari, R. Seu, L. Marinangeli, W. Johnson, R. Jordan, J. Plaut, A. Safaenili, D. Gurnett, G. Ori *et al.*, "Performance and surface scattering models for the mars advanced radar for subsurface and ionosphere sounding (marsis)," *Planetary and Space Science*, vol. 52, no. 1, pp. 149–156, 2004.

[44] S. M. Clifford, "A model for the hydrologic and climatic behavior of water on mars," *Journal of Geophysical Research: Planets*, vol. 98, no. E6, pp. 10 973–11 016, 1993.

[45] D. Biccari, D. Calabrese, D. Gurnett, R. Huff, L. Marinangeli, R. Jordan, E. Nielsen, G. Ori, G. Picardi, J. PIaut *et al.*, "Venus subsurface ionosphere radar sounder: Vensis," in *3D Data Processing, Visualization and Transmission, 2004. 3DPVT 2004. Proceedings. 2nd International Symposium on.* IEEE, 2004, pp. 931–937.

[46] D. W. Strangway and G. R. Olhoeft, "Electrical properties of planetary surfaces," *Philosophical Transactions of the Royal Society of London A: Mathematical, Physical and Engineering Sciences*, vol. 285, no. 1327, pp. 441–450, 1977. [Online]. Available: http://rsta.royalsocietypublishing.org/content/285/1327/441

[47] W. D. Carrier, G. R. Olhoeft, and W. Mendell, "Physical properties of the lunar surface," *Lunar sourcebook*, pp. 475–594, 1991.

[48] D. M. Schroeder, C. Grima, and D. D. Blankenship, "Evidence for variable grounding-zone and shear-margin basal conditions across thwaites glacier, west antarctica," *Geophysics*, vol. 81, no. 1, pp. WA35–WA43, 2015.

[49] M. E. Peters, D. D. Blankenship, and D. L. Morse, "Analysis techniques for coherent airborne radar sounding: Application to west antarctic ice streams," *Journal of Geophysical Research: Solid Earth*, vol. 110, no. B6, 2005.

[50] L. Boithias and L.-J. Libols, *Radio wave propagation*. North Oxford acad. London, 1987.

[51] T. Hagfors, "Backscattering from an undulating surface with applications to radar returns from the moon," *Journal of Geophysical Research*, vol. 69, no. 18, pp. 3779–3784, 1964. [Online]. Available: http://dx.doi.org/10.1029/JZ069i018p03779

[52] L. Bruzzone, G. Alberti, C. Catallo, A. Ferro, W. Kofman, and R. Orosei, "Subsurface radar sounding of the jovian moon ganymede," *Proceedings of the IEEE*, vol. 99, no. 5, pp. 837–857, 2011.

[53] J. D. Kraus, "Radio astronomy, 2-nd ed," *Cygnus-Quasar Books, Powell, Ohio*, pp. 7–12, 1986.

[54] B. A. Campbell, "Scale-dependent surface roughness behavior and its impact on empirical models for radar backscatter," *IEEE Transactions on Geoscience and Remote Sensing*, vol. 47, no. 10, pp. 3480–3488, Oct 2009.

[55] V. Mikhnev and P. Vainikainen, "Characterization of underground objects in uwb gpr by range profiling of phase," in *Radar Conference (EuRAD), 2010 European.* IEEE, 2010, pp. 368–371.

[56] V. Mikhnev, M.-K. Olkkonen, and E. Huuskonen, "Subsurface target identification using phase profiling of impulse gpr data," in *Ground Penetrating Radar (GPR), 2012 14th International Conference on.* IEEE, 2012, pp. 376–380.

[57] B. Sai and L. P. Ligthart, "Gpr phase-based techniques for profiling rough surfaces and detecting small, low-contrast landmines under flat ground," *IEEE Transactions on Geoscience and Remote Sensing*, vol. 42, no. 2, pp. 318–326, 2004.

[58] E. Huuskonen-Snicker, V. A. Mikhnev, and M.-K. Olkkonen, "Discrimination of buried objects in impulse gpr using phase retrieval technique," *IEEE Transactions on Geoscience and Remote Sensing*, vol. 53, no. 2, pp. 1001–1007, 2015.

[59] A. Ferro, A. Pascal, and L. Bruzzone, "A novel technique for the automatic detection of surface clutter returns in radar sounder data," *IEEE Transactions on Geoscience and Remote Sensing*, vol. 51, no. 5, pp. 3037–3055, 2013.

[60] P. Choudhary, J. W. Holt, and S. D. Kempf, "Surface clutter and echo location analysis for the interpretation of sharad data from mars," *IEEE Geoscience and Remote Sensing Letters*, vol. 13, no. 9, pp. 1285–1289, Sept 2016.

[61] G. Picardi, S. Sorge, R. Seu, G. Fedele, and R. L. Jordan, "Coherent cancellation of surface clutter for radar sounding," in *Geoscience and Remote Sensing Symposium, 1999. IGARSS '99 Proceedings. IEEE 1999 International*, vol. 5, 1999, pp. 2678–2680.

[62] R. K. Raney, "Radar sounder: Cross-track polarimetric selectivity," in *Synthetic Aperture Radar (EUSAR), 2008 7th European Conference on*, June 2008, pp. 1–4.

[63] D. Castelletti, D. M. Schroeder, S. Hensley, C. Grima, G. Ng, D. Young, Y. Gim, L. Bruzzone, A. Mousessian, and D. D. Blankenship, "Clutter detection using two-channel radar sounder data," in *2015 IEEE International Geoscience and Remote Sensing Symposium (IGARSS)*, July 2015, pp. 1052–1055.

[64] J. Thomas, C. Moss, and M. Vater, *Echolocation in Bats and Dolphins.* University of Chicago Press, 2004.

[65] J. Simmons, M. Fenton, and M. O'Farrell, "Echolocation and pursuit of prey by bats," *Science*, vol. 203, no. 4375, pp. 16–21, 1979.

[66] G. Jones, "Scaling of echolocation call parameters in bats," *Journal of Experimental Biology*, vol. 202, no. 23, pp. 3359–3367, 1999.

[67] M. E. Bates, J. A. Simmons, and T. V. Zorikov, "Bats use echo harmonic structure to distinguish their targets from background clutter," *Science*, vol. 333, no. 6042, pp. 627–630, 2011.

[68] S. Hiryu, M. E. Bates, J. A. Simmons, and H. Riquimaroux, "Fm echolocating bats shift frequencies to avoid broadcast–echo ambiguity in clutter," *Proceedings of the National Academy of Sciences*, vol. 107, no. 15, pp. 7048–7053, 2010.

[69] M. Warnecke, M. E. Bates, V. Flores, and J. A. Simmons, "Spatial release from simultaneous echo masking in bat sonar," *The Journal of the Acoustical Society of America*, vol. 135, no. 5, pp. 3077–3085, 2014.

[70] M. Denny, "The physics of bat echolocation: Signal processing techniques," *American Journal of Physics*, vol. 72, no. 12, pp. 1465–1477, 2004.

[71] B. D. Lawrence and J. A. Simmons, "Measurements of atmospheric attenuation at ultrasonic frequencies and the significance for echolocation by bats," *The Journal of the Acoustical Society of America*, vol. 71, no. 3, pp. 585–590, 1982.

[72] K. Rawer, *Wave propagation in the ionosphere.* Springer Science & Business Media, 2013, vol. 5.

[73] D. E. Wahl, P. H. Eichel, D. C. Ghiglia, and C. V. Jakowatz, "Phase gradient autofocus-a robust tool for high resolution sar phase correction," *IEEE Transactions on Aerospace and Electronic Systems*, vol. 30, no. 3, pp. 827–835, Jul 1994.

[74] G. Jones and E. C. Teeling, "The evolution of echolocation in bats," *Trends in Ecology and Evolution*, vol. 21, no. 3, pp. 149 – 156, 2006.

[75] N. B. Simmons, K. L. Seymour, J. Habersetzer, and G. F. Gunnell, "Primitive early eocene bat from wyoming and the evolution of flight and echolocation," *Nature*, vol. 451, pp. 818 – 821, 2008.

[76] B. B. Mandelbrot, *The fractal geometry of nature*. San Francisco, CA: Freeman, 1982.

[77] G. Franceschetti, A. Iodice, M. Migliaccio, and D. Riccio, "Scattering from natural rough surfaces modeled by fractional brownian motion two-dimensional processes," *IEEE Transactions on Antennas and Propagation*, vol. 47, no. 9, pp. 1405–1415, Sep 1999.

[78] A. Ferro, A. Pascal, and L. Bruzzone, "A novel technique for the automatic detection of surface clutter returns in radar sounder data," *IEEE Transactions on Geoscience and Remote Sensing*, vol. 51, no. 5, pp. 3037–3055, May 2013.

[79] J. J. Plaut, A. Safaeinili, J. W. Holt, R. J. Phillips, J. W. Head, R. Seu, N. E. Putzig, and A. Frigeri, "Radar evidence for ice in lobate debris aprons in the mid-northern latitudes of mars," *Geophysical Research Letters*, vol. 36, no. 2, pp. n/a–n/a, 2009, l02203. [Online]. Available: http://dx.doi.org/10.1029/2008GL036379

[80] B. Campbell, L. Carter, R. Phillips, J. Plaut, N. Putzig, A. Safaeinili, R. Seu, D. Biccari, A. Egan, and R. Orosei, "Sharad radar sounding of the vastitas borealis formation in amazonis planitia," *Journal of Geophysical Research: Planets*, vol. 113, no. E12, 2008.

[81] R. Croci, R. Seu, E. Flamini, and E. Russo, "The shallow radar (sharad) onboard the nasa mro mission," *Proceedings of the IEEE*, vol. 99, no. 5, pp. 794–807, May 2011.

[82] M. Restano, R. Seu, and G. Picardi, "A phase-gradient-autofocus algorithm for the recovery of marsis subsurface data," *IEEE Geoscience and Remote Sensing Letters*, vol. 13, no. 6, pp. 806–810, June 2016.

[83] B. A. Campbell, N. E. Putzig, F. J. Foss, and R. J. Phillips, "Sharad signal attenuation and delay offsets due to the martian ionosphere," *IEEE Geoscience and Remote Sensing Letters*, vol. 11, no. 3, pp. 632–635, March 2014.

[84] T. Wang, J. M. Keller, P. D. Gader, and O. Sjahputera, "Frequency subband processing and feature analysis of forward-looking ground-penetrating radar signals for land-mine detection," *IEEE Transactions on Geoscience and Remote Sensing*, vol. 45, no. 3, pp. 718–729, March 2007.

[85] F. Russo, M. Cutigni, R. Orosei, C. Taddei, R. Seu, D. Biccari, E. Giacomoni, O. Fuga, and E. Flamini, "An incoherent simulator for the sharad experiment," in *2008 IEEE Radar Conference*, May 2008, pp. 1–4.

[86] D. E. Smith, M. T. Zuber, S. C. Solomon, R. J. Phillips, J. W. Head, J. B. Garvin, W. B. Banerdt, D. O. Muhleman, G. H. Pettengill, G. A. Neumann, F. G. Lemoine, J. B. Abshire, O. Aharonson, C. David, Brown, S. A. Hauck, A. B. Ivanov, P. J. McGovern, H. J. Zwally, and T. C. Duxbury, "The global topography of mars and implications for surface evolution," *Science*, vol. 284, no. 5419, pp. 1495–1503, 1999.

[87] R. Orosei, R. Bianchi, A. Coradini, S. Espinasse, C. Federico, A. Ferriccioni, and A. I. Gavrishin, "Self-affine behavior of martian topography at kilometer scale from mars orbiter laser altimeter data," *Journal of Geophysical Research: Planets*, vol. 108, no. E4, 2003, 8023.

[88] P. Smith, L. Tamppari, R. Arvidson, D. Bass, D. Blaney, W. Boynton, A. Carswell, D. Catling, B. Clark, T. Duck *et al.*, "Introduction to special section on the phoenix mission: landing site characterization experiments, mission overviews, and expected science," *Journal of Geophysical Research: Planets*, vol. 113, no. E3, 2008.

[89] N. E. Putzig, R. J. Phillips, B. A. Campbell, M. T. Mellon, J. W. Holt, and T. C. Brothers, "Sharad soundings and surface roughness at past, present, and proposed landing sites on mars: reflections at phoenix may be attributable to deep ground ice," *Journal of Geophysical Research: Planets*, vol. 119, no. 8, pp. 1936–1949, 2014.

[90] J. Boisson, E. Heggy, S. M. Clifford, K. Yoshikawa, A. Anglade, and P. Lognonné, "Radar sounding of temperate permafrost in alaska: Analogy to the martian midlatitude to high-latitude ice-rich terrains," *Journal of Geophysical Research: Planets*, vol. 116, no. E11, 2011.

[91] L. Castaldo, D. Mège, J. Gurgurewicz, R. Orosei, and G. Alberti, "Global permittivity mapping of the martian surface from sharad," *Earth and Planetary Science Letters*, vol. 462, pp. 55–65, 2017.

[92] G. J. Freeman, A. C. Bovik, and J. W. Holt, "Automated detection of near surface martian ice layers in orbital radar data," in *Image Analysis & Interpretation (SSIAI), 2010 IEEE Southwest Symposium on*. IEEE, 2010, pp. 117–120.

[93] A. Ferro and L. Bruzzone, "Automatic extraction and analysis of ice layering in radar sounder data," *IEEE Transactions on Geoscience and Remote Sensing*, vol. 51, no. 3, pp. 1622–1634, 2013.

[94] K. Dabov, A. Foi, V. Katkovnik, and K. Egiazarian, "Image denoising by sparse 3-d transform-domain collaborative filtering," *IEEE Transactions on image processing*, vol. 16, no. 8, pp. 2080–2095, 2007.

[95] C. Steger, "An unbiased detector of curvilinear structures," *IEEE Transactions on pattern analysis and machine intelligence*, vol. 20, no. 2, pp. 113–125, 1998.

[96] B. Smock and J. Wilson, "Efficient multiple layer boundary detection in ground-penetrating radar data using an extended viterbi algorithm," in *Proc. SPIE*, vol. 8357, 2012, p. 83571X.

[97] B. Smock and J. Wilson, "Reciprocal pointer chains for identifying layer boundaries in ground-penetrating radar data," in *Geoscience and Remote Sensing Symposium (IGARSS), 2012 IEEE International*. IEEE, 2012, pp. 602–605.

[98] U. Spagnolini and V. Rampa, "Multitarget detection/tracking for monostatic ground penetrating radar: Application to pavement profiling," *IEEE Transactions on Geoscience and Remote sensing*, vol. 37, no. 1, pp. 383–394, 1999.

[99] M. Nicoli, V. Rampa, and U. Spagnolini, "Multitarget detection/tracking based on hidden markov models," in *Acoustics, Speech, and Signal Processing, 2000. ICASSP'00. Proceedings. 2000 IEEE International Conference on*, vol. 5. IEEE, 2000, pp. 3196–3199.

[100] D. J. Crandall, G. C. Fox, and J. D. Paden, "Layer-finding in radar echograms using probabilistic graphical models," in *Pattern Recognition (ICPR), 2012 21st International Conference on*. IEEE, 2012, pp. 1530–1533.

[101] S. Lee, J. Mitchell, D. J. Crandall, and G. C. Fox, "Estimating bedrock and surface layer boundaries and confidence intervals in ice sheet radar imagery using mcmc," in *Image Processing (ICIP), 2014 IEEE International Conference on*. IEEE, 2014, pp. 111–115.

[102] A.-M. Ilisei and L. Bruzzone, "A system for the automatic classification of ice sheet subsurface targets in radar sounder data," *IEEE Transactions on Geoscience and Remote Sensing*, vol. 53, no. 6, pp. 3260–3277, 2015.

[103] A.-M. Ilisei and L. Bruzzone, "A model-based technique for the automatic detection of earth continental ice subsurface targets in radar sounder data," *IEEE Geoscience and Remote Sensing Letters*, vol. 11, no. 11, pp. 1911–1915, 2014.

[104] N. B. Karlsson, D. Dahl-Jensen, S. P. Gogineni, and J. D. Paden, "Tracing the depth of the holocene ice in north greenland from radio-echo sounding data," *Annals of Glaciology*, vol. 54, no. 64, pp. 44–50, 2013.

[105] V. de Paul Onana, L. S. Koenig, J. Ruth, M. Studinger, and J. P. Harbeck, "A semiautomated multilayer picking algorithm for ice-sheet radar echograms applied to ground-based near-surface data," *IEEE Transactions on Geoscience and Remote Sensing*, vol. 53, no. 1, pp. 51–69, 2015.

[106] J. E. Mitchell, D. J. Crandall, G. C. Fox, and J. D. Paden, "A semi-automatic approach for estimating near surface internal layers from snow radar imagery," in *Geoscience and Remote Sensing Symposium (IGARSS), 2013 IEEE International*. IEEE, 2013, pp. 4110–4113.

[107] C. Panton, "Automated mapping of local layer slope and tracing of internal layers in radio echograms," *Annals of Glaciology*, vol. 55, no. 67, pp. 71–77, 2014.

[108] L. C. Sime, R. C. Hindmarsh, and H. Corr, "Instruments and methods automated processing to derive dip angles of englacial radar reflectors in ice sheets," *Journal of Glaciology*, vol. 57, no. 202, pp. 260–266, 2011.

[109] J. A. MacGregor, M. A. Fahnestock, G. A. Catania, J. D. Paden, S. Prasad Gogineni, S. K. Young, S. C. Rybarski, A. N. Mabrey, B. M. Wagman, and M. Morlighem, "Radiostratigraphy and age structure of the greenland ice sheet," *Journal of Geophysical Research: Earth Surface*, vol. 120, no. 2, pp. 212–241, 2015.

[110] C. Oliver and S. Quegan, *Understanding synthetic aperture radar images*. SciTech Publishing, 2004.

[111] C. Cook, *Radar signals: An introduction to theory and application*. Elsevier, 2012.

[112] D. K. Barton and H. R. Ward, *Handbook of radar measurement*. Prentice Hall, 1969.

[113] G. D. Forney, "The viterbi algorithm," *Proceedings of the IEEE*, vol. 61, no. 3, pp. 268–278, 1973.

[114] L. R. Rabiner, "A tutorial on hidden markov models and selected applications in speech recognition," *Proceedings of the IEEE*, vol. 77, no. 2, pp. 257–286, 1989.

[115] A. Ferro and L. Bruzzone, "Analysis of radar sounder signals for the automatic detection and characterization of subsurface features," *IEEE Transactions on Geoscience and Remote Sensing*, vol. 50, no. 11, pp. 4333–4348, 2012.